論文 / 著書情報
Article / Book Information

題目(和文)	ナノ構造制御触媒を用いたメタンの二酸化炭素改質反応の低温化
Title(English)	Carbon dioxide reforming of methane under low temperature by nano-phase controlled catalyst
著者(和文)	庄司州作
Author(English)	Shusaku Shoji
出典(和文)	学位:博士(学術), 学位授与機関:東京工業大学, 報告番号:甲第11539号, 授与年月日:2020年3月26日, 学位の種別:課程博士, 審査員:宮内 雅浩,中島 章,生駒 俊之,松下 伸広,松下 祥子
Citation(English)	Degree:Doctor (Academic), Conferring organization: Tokyo Institute of Technology, Report number:甲第11539号, Conferred date:2020/3/26, Degree Type:Course doctor, Examiner:,,,,
学位種別(和文)	博士論文
Type(English)	Doctoral Thesis

令和２年度

博士論文

Carbon dioxide reforming of methane under low temperature by nano-phase controlled catalyst

ナノ構造制御触媒を用いたメタンの二酸化炭素改質反応の低温化

物質理工学院材料系　宮内研究室

庄司州作

Contents

1. **Introduction**

1.1 Methane conversion

1.1.1 Necessity of methane conversion

Recent years, the mining amount of natural gas and landfill gas are rapidly increasing because of the development of mining technology. British Petroleum Company predicted the future demand of fuel souses. According to this prediction, the demand of coal, oil, and nuclear will be decreased, however, the demand of gas will massively increase[1]. In case of United States, it is predicted that the mining amount of shale gas will drastically increase[2]. Because of the importance of conversion of natural gas, methane (CH_4) conversion into higher valuable chemical feed stock is highly expected.

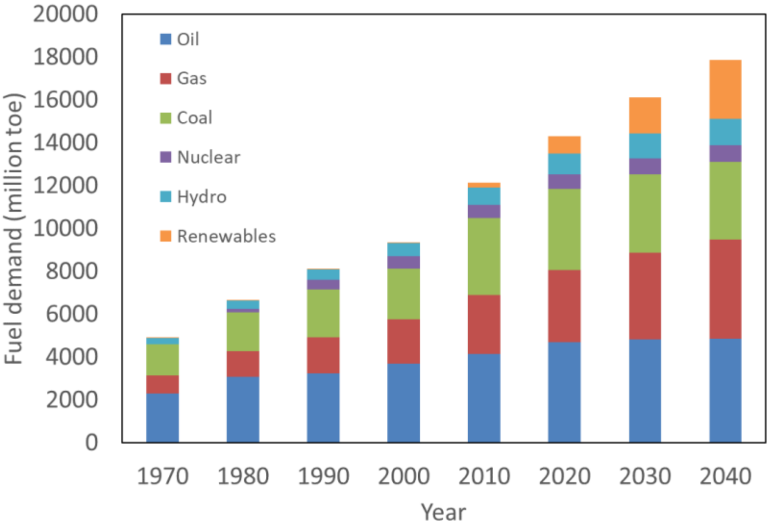

Figure 1.1 Outlook of the world energy demand[1].

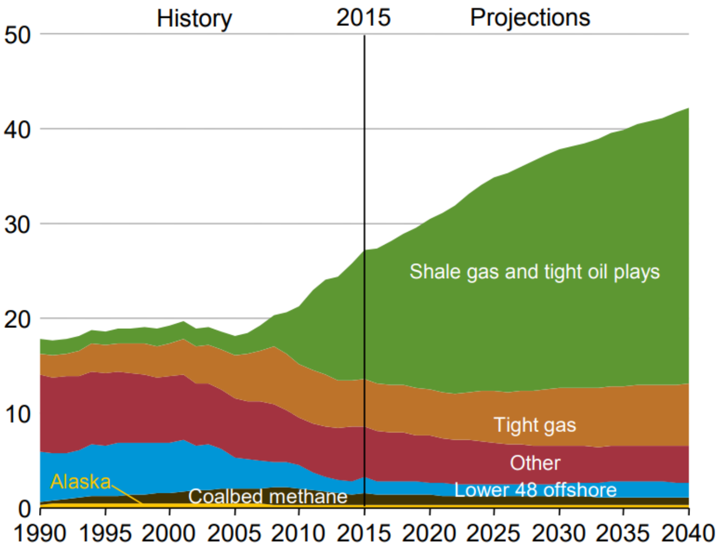

Figure 1.2 U.S. dry natural gas production by source in the Reference case, 1990–2040 (trillion cubic feet)[2].

1.1.2 Methane conversion

Among the various CH_4 conversion technology, partial oxidation (PO)[3], steam reforming (SRM) [4-6] and dry reforming of methane (DRM)[7] have mostly been studied. These reactions use CH_4 as a reductant as described in equation (1)-(3). In these cases, oxygen (O_2), water (H_2O) or carbon dioxide (CO_2) are used as an oxidant.

PO $CH4 + \frac{1}{2}O2 \leftrightarrow CO + 2H2 \quad \Delta H = -35.9\ kJ/mol \quad (1)$

SRM $CH4 + H2O \leftrightarrow CO + 3H2 \quad \Delta H = +205\ kJ/mol \quad (2)$

DRM $CH4 + CO2 \leftrightarrow 2CO + 2H2 \quad \Delta H = +247\ kJ/mol \quad (3)$

Among these methane reforming reactions, DRM is attractive since DRM can convert top2 greenhouse gases (1st. CO_2, 2nd CH_4) into chemically valuable syngas. Since the main products of land fill gas are CH_4 and CO_2, the practical demand of DRM reaction is high from gas or chemical industries. With respect to DRM, SRM and PO have disadvantage because of the production of CO_2 by the overoxidation of CH_4. In particular of SRM, the ratio of H_2/CO is too high to be directly used for methanol or other chemical synthesis[8]. Further, there are the safety issue problems in the case of PO because of its high exothermic reaction[9]. On the other hand, DRM can produce nearly 1 ratio of H_2/CO[10]. However, the high stability of CH_4 and CO_2 makes DRM as less favorable reaction, and it requires the high reaction temperature because of the strong endothermic reaction (ΔH_{298}=247 kJ/mol). Therefore, it is able to say that DRM is the most attractive reaction but most challenging reaction among the various methane reforming reactions.

1.1.3 History of methane conversion

In 1928, Fischer and Tropsch firstly reported the catalyst technology to produce liquid fuel using syngas[7]. They used metal Ni and Co as catalysts, however, they observed harsh carbon deposition called coking onto catalysts. After several decades since the Fischer and Tropsch report, Lewis et al reported metal oxide support materials for metal catalyst to provide oxygen species from supports to the active sites and converted carbon spices to CO[11]. Indeed, Al_2O_3 support based catalysts have been investigated to promote the DRM reaction, and Ni loaded

Al_2O_3 catalysts were developed[12-14] as highly active economical catalyst using abundant elements. In addition to Ni catalyst, the noble metals such as Pt, Pd, Rh, Ir and Ru metal exhibited high activity for DRM[15-18]. Basic, neutral and acidic metal oxides supports, such as La_2O_3, MgO, TiO_2. CeO_2, SiO_2, and ZrO_2 have been also investigated as a catalyst support for DRM [8, 19-22]. However, their stabilities were still insufficient because of the aggregation and coking. In other words, these two problems are making DRM far from application, *i. e.* aggregation and coking.

1.1.4 Thermodynamics of methane conversion

To suppress the aggregation, reaction temperature should be reduced. However, as shown in Figure 3 which calculated equilibrium of DRM at atmospheric pressure, coking is favorably proceeded at low temperature through CH_4 decomposition ($CH_4 = C(s) + 2H_2$)[7, 23, 24].

$$CH4 = C(s) + 2H2 \qquad (5)$$

Some researcher predicted the coking proceeds along with equation (6).

$$CH4 + * \rightarrow CH3 * \rightarrow CH2 * \rightarrow CH * \rightarrow C \qquad (6)$$

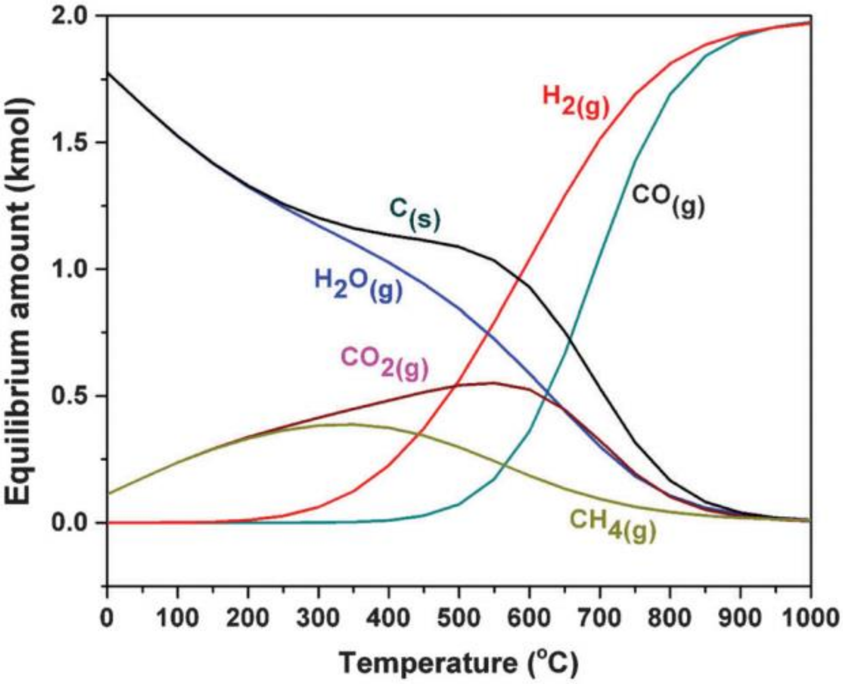

Figure 1.3 Thermodynamic plots for DRM[25].

In the methane reforming reaction, the dissociated methane species react with surface oxygen spices or lattice oxygen. Further, it is known that the reaction kinetics is sensitive to the structure of metal catalysts[26, 27]. Further, the active sites for methane reforming are not only the metal surface but also the metal/oxide interfaces. Since, increase of the interfaces of metal/oxide surface by controlling metal size to be nano-order size can be a good strategy for methane reforming catalyst[28, 29]. (Figure1. 4)

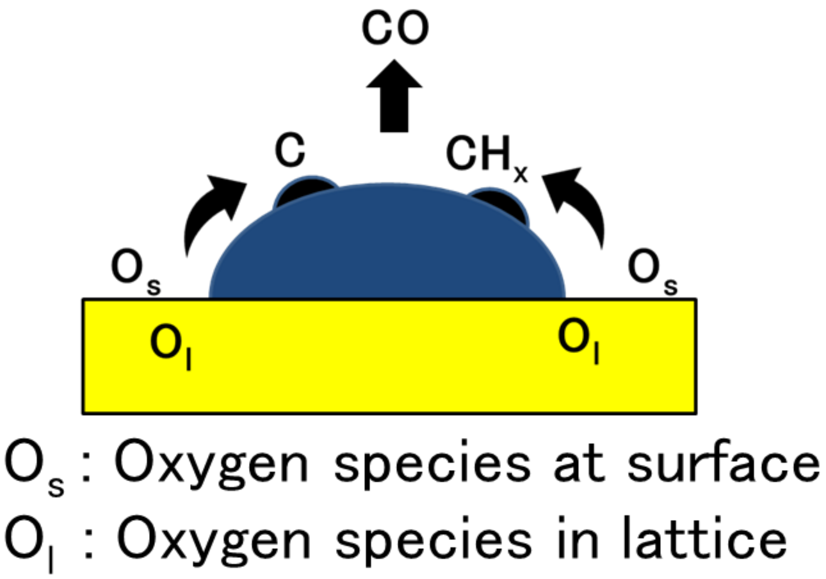

Figure 1.4 Model of the oxygen removal on the supported catalyst.

However, as described before, it is not so simple to achieve stable reaction by only decreasing catalysts size. The nano sized metal particles easily diffuse on the oxide supports even under not so high temperature around 450 ° C. Further, in the case of Ni metal, the deposited carbon species on the surface of support diffuse into Ni lattice causing nickel carbide. Subsequently, whisker like carbon grow up on Ni carbide and causes the peel off of Ni catalyst from the oxide supports. The separated Ni continue to react with methane to form fibrous carbon[30]. To summarize the phenomena seen in conventional thermal catalyst sytems, there are two problems under high temperature, *i. e.,* high fuel consumption and aggregation of catalysts. On the other hand, at low temperature, the reaction of coking becomes the highly favored reaction by the consideration of thermodynamics. Further, the nano sized catalysts have high anti-coking features but easily aggregate each other even at lower temperature.

Therefore, the efficient catalysts to drive DRM should have three requirements as follows,

1 Suppress the carbon deposition (coking) onto surface.

2 Quick oxidation of carbon species on the catalyst surfaces into CO and H_2.

3 Robust against heat to prevent aggregation.

1.2 Semiconductor photocatalysis

1.2.1 Brief history of photocatalysis since 1970s

The concept of photocatalysis was firstly established by Prof. Fujishima and Prof. Honda in 1972[31]. In this paper, they constructed electrochemical cell with TiO_2 anode which connected to Pt cathode. When the TiO_2 anode was irradiated by light source, H_2 was produced at Pt cathode and O_2 was produced at the TiO_2 anode through water splitting. This phenomenon is called as “Honda-Fujishima effect”. After this report, many researches on photocatalysis have been initiated. For example, deactivation of cyanide[32], photocatalytic conversion of carbohydrate into hydrogen have been reported[33]. Also, in 1978, Prof. Halmann developed p-type gallium phosphide as a photocathode and reduced CO_2 into formic acid by using water as electron donor[34]. In 1979, Ptof. Inoue and Prof. Fujishima demonstrated the CO_2 reduction by various semiconductors like TiO_2, CdS, GaP, ZnO and SiC[35]. In this paper, they showed the relationship between photocatalytic activities and conduction band positions (Figure 1.5).

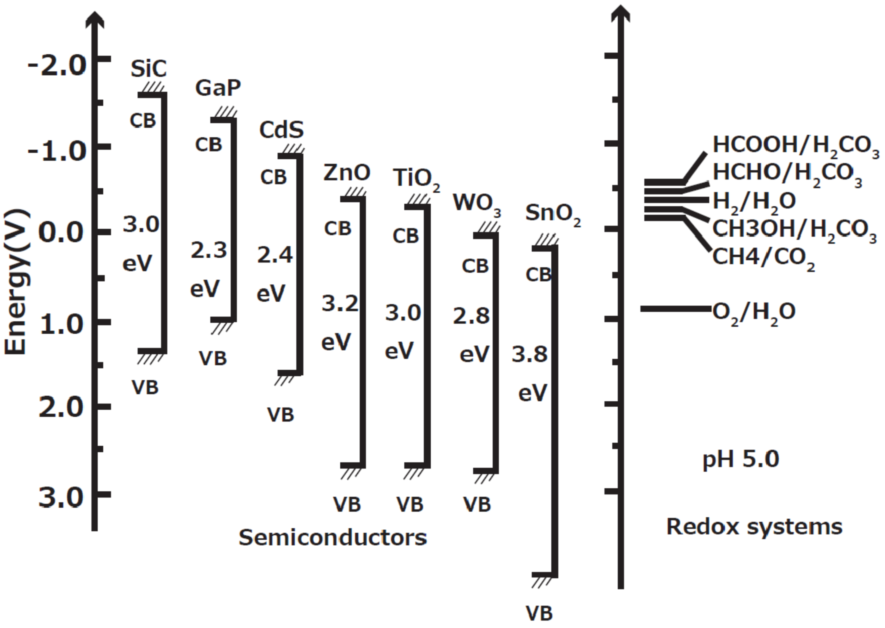

Figure 1.5 Relation between band structure of semiconductors and redox potentials of CO_2.

In 1990s, different from energy conversion, photocatalytic toxic organic decomposition into non-toxic material became the hot topic from the standpoint of environmental purification[36, 37]. Then, the TiO_2 films and/or particles have been developed for the application of water and/or air purification[38]. In 1997, in addition, the phenomenon of photon induced superhydrophilic has been founded to be applied for self-cleaning building materials[39]. Nowadays, the applications of photocatalysts have widely been used as gas sensor[40], synthesis of high value organic compounds[41],self-cleaning materials[42] and purification of indoor environment[43].

1.2.2 Mechanism of photocatalysis

The photocatalytic reaction scheme is shown in Figure 1.6. When the photocatalytic semiconductor irradiated by photons whose energy is higher than semiconductor's band gap (BG), electrons in the valence band (VB) is excited to the conduction band (CB). After excitation of electrons, same number of holes are generated at the VB. In the case of co-catalyst combined system, the excited electrons or holes are injected into these co-catalysts and promote the charge separation. When there is no reactant around photocatalytic system, the photogenerated charges are recombined and emit heat or fluorescence. On the other hand, when the reactants are exposed to photocatalyst surface, the photogenerated electrons reduce the reactants and photogenerated holes oxidize the reactants. These reactions should be driven by the chemical potential difference of the reactants and electrons or holes. In the case of CO_2 reduction, CO_2 molecules are reduced by the electrons to produce hydrocarbon or carbon monoxide, while H_2O molecules are oxidized by the holes to produce oxygen.

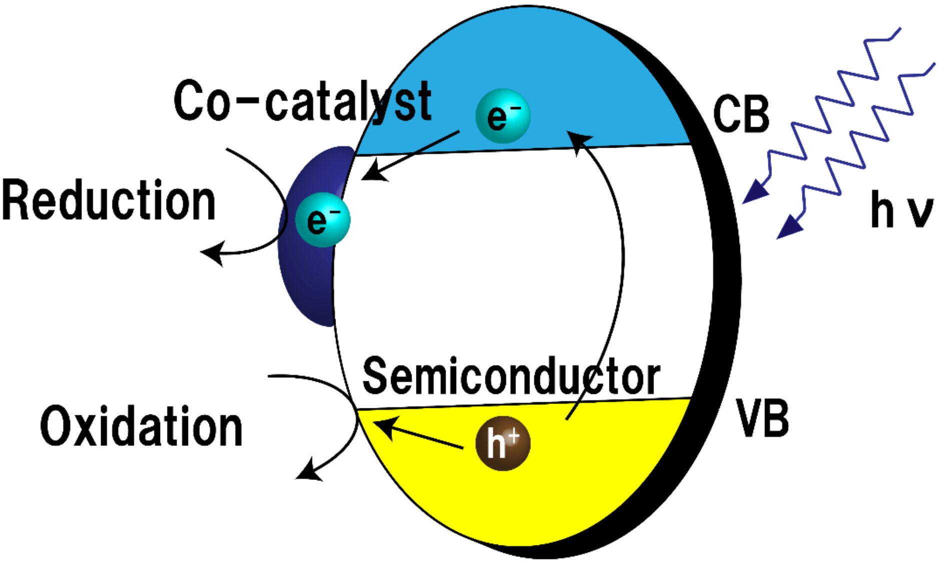

Figure 1.6 Model of the photocatalytic reaction.

1.2.3 Semiconductor photocatalysts

From the viewpoint of the efficient use of solar energy, narrowed BG of the semiconductor is preferred. From the viewpoint of kinetics, the CB should be high and VB should be deep to achieve worthful reaction rate, however, the absorption from light is decreased by widening of the BG. Figure 1.7 shows the relationship between BG and Flatband reported by Scaife[44]. In case of n-type semiconductors, the Flatband potential is almost consistent with the potential of CB edge. This relation could be represented as equation (5). Since the valence band position of the oxide is fixed by the 2p-orbital oxygen in almost of photocatalytic oxides, the position of CB relies on BG.

$$V_{fb}(SHE) = 2.94 - BG \qquad (5)$$

Therefore, the semiconductors used for various chemical reaction such as CO_2

reduction or environmental purification should be chosen by the consideration of this equation. In the case of CO_2 reduction, limited oxides, such as $SrTiO_3$ and Ta_2O_5, can be the candidate owing to their high CB.

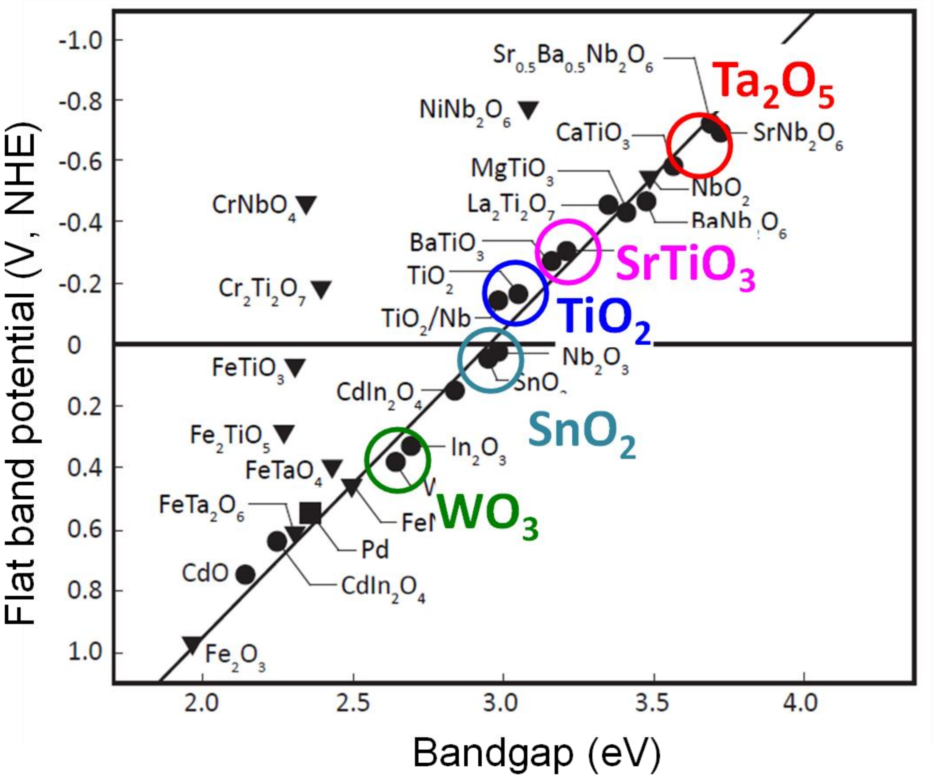

Figure 1.7 Relation between the flatband potential and BG for metal oxide semiconductors.

1.2.4 Photocatalytic CO_2 reduction

As described above, photocatalytic CO_2 reduction is one of the most attractive reaction since it can convert CO_2, which is most contribute to grovel worming, into higher valuable products. However, it is one of the most difficult reactions, because of the high stability of CO_2 molecule. CO_2 reduction requires the high reduction potential of CO_2 and it contains multi-electron reaction (equation 7-11 vs NHE ap pH = 7)[45-47].

$$CO2 + 2H + +2e - \rightarrow HCOOH\ E0 = -0.61\ V \qquad (7)$$

$$CO2 + 2H + +2e - \rightarrow CO + H2O\ E0 = -0.53\ V \qquad (8)$$

$$CO2 + 4H + +4e - \rightarrow HCHO + H2O\ E0 = -0.48\ V \qquad (9)$$

$$CO2 + 6H + +6e - \rightarrow CH3OH + H2O\ E0 = -0.38\ V \qquad (10)$$

$$CO2 + 8H + +8e - \rightarrow CH4 + 2H2O\ E0 = -0.24\ V \qquad (11)$$

Further, not only the band structure control, but also designing active sites for CO2 reduction should be considered for efficient reaction. Co-catalyst can improve the activity of the photocatalysts by suppressing charge recombination, facilitate multi-electron reaction. It is known that Cu[48-50], Ag[51, 52] and Au[53] exhibit high activity for CO_2 reduction. The author of this thesis synthesized Cu_xO loaded $SrTiO_3$ nanorod thin film and observed enhanced photocatalytic performance[54, 55]. There were few reports, which achieves photocatalytic CO_2 reduction using water as an electron donor.[51, 56, 57]. Since, the oxygen is abundantly contained in air and can be easily contaminate to the reactor or evaluation system. In my reports, isotope trace analysis was conducted by using $H_2{}^{18}O$ and $^{13}CO_2$ to detect $^{18}O_2$ and ^{13}CO and proved the products were truly produced through photocatalytic CO_2 reduction (Figure 1.8). Further, the ratio of the reduction products and the oxidation product became 2:1 which prove the stoichiometric reaction has proceeded (Figure 1.8). Therefore, for the design of photocatalytic system should contain co-catalyst in not only aqueous reaction but also gas phase reaction such as DRM.

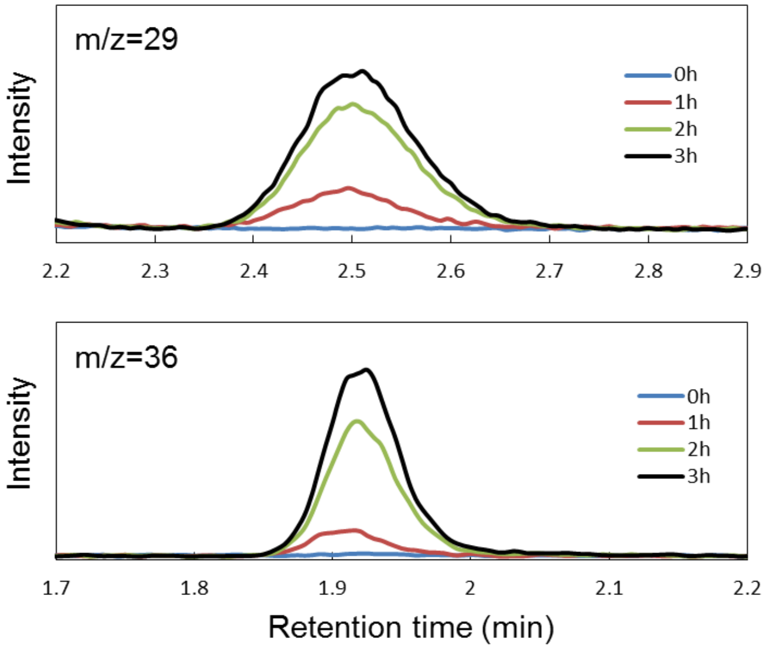

Figure 1.8 Mass spectra of ^{13}CO (top) and $^{18}O_2$ (bottom) produced on Cu_xO loaded $SrTiO_3$ photocatalyt.

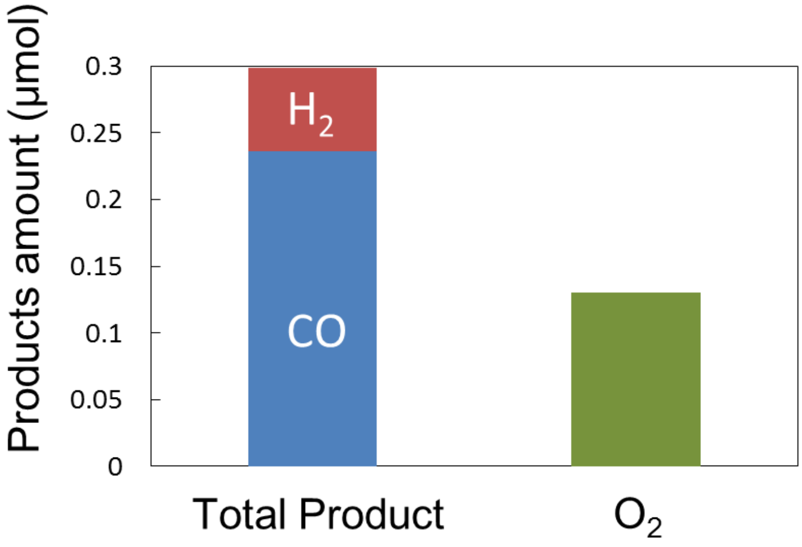

Figure 1.9 Produced amount of reduction products and oxidation product. The total product of reduction product became twice higher than oxidation product.

1.3 Photocatalytic dry reforming of methane (photo-DRM)

1.3.1 Potential of photocatalytic methane reforming

As described above, methane is the one of the most stable molecules and the conversion with CO_2 is endothermic reaction. Thus, to improve the efficiency and to reduce fuel consumption to drive the DRM system, using renewable energy like light is attractive. Direct excitation of methane molecule needs high energy photon the wavelength around 94-128nm. However, it becomes easier using photocatalysts with excited electrons or holes. Therefore, it has great potentials to proceed Up-hill reactions like methane conversion by photocatalysis.

1.3.2 Photocatalytic methane conversion

Though photon assisted methane reforming is quite attractive, previous reports on this challenge are quite limited. Yoshida et al. reported photon induced methane reforming by using MgO, ZrO_2, TiO_2 and β Ga_2O_3[58-60] under light irradiation to convert CH_4 and CO_2 into CO and H_2. Han et al. reported black TiO_2 with Pt catalyst converted CH_4 and CO_2 under visible light irradiation[61]. Ye et al. proceeded SRM on Rh/TiO_2 under visible light irradiation[62]. Singghi et al. proceeded DRM under UV irradiation at 973 K by using various photocatalysts such as $SrTiO_3$, TiO_2, WO_3 and SnO_2 and showed the conduction band position of semiconductor is main factor to drive DRM under UV irradiation[63]. However, these experiments were conducted under elevated temperature and methane conversion was lower than 1 % without heating. Further, there was no evidence that the reaction was driven by photocatalytic reaction. Therefore, these works should be categorized as a “photo-assisted DRM” rather than photocatalytic DRM. Previous studies of photo-assisted DRM are listed in the following table 1. Methane conversion and/or production yield of these previous studies were less than 5 %. Some of these studies indicate that the DRM reaction was driven by hot-carrier generation or bandgap excitation, however, they did not show any clear evidence on the reaction scheme.

Table 1. List of previously reported studies regarding photo-induced DRM.

	Catalyst	Reaction	yield or conversion	mechanism
Yoshida et al.[60]	β-Ga_2O_3	Non-oxidative methane coupling DRM	less than 1 % (@200 ℃)	no evidence
Ye et al.[62]	Rh/TiO_2	Steam-reforming of methane	2.6 % (@260 ℃)	Hot carrier from metal
Han et al.[61]	Pt/Black TiO_2	DRM	1.47 % (@550 ℃)	Not included
Singgih et al.[63]	$SrTiO_3$	DRM	3.88 % (@700 ℃)	Not included

1.4 Objective and research strategies

1.4.1 Research Objectives

As described above, the DRM reaction driven under low temperature is quite attractive and challenging, thus I decided the objectives as to drive stable DRM at low temperature.

1.4.2 Strategies

The structure of the thesis is shown as below. There are two approaches for the catalyst design. First approach is the topological control of thermal catalyst to stably drive DRM (Chapter 2). Indeed, some previous studies indicated that carbon removal using lattice oxygen was important. However, there are still problems of aggregation of catalyst and the mechanism of carbon growth is still unclear. Therefore, I try to develop the catalyst in this tehsis by controlling the catalyst composition and nanostructure. I carefully investigate the mechanism of carbon growth by the in-situ TEM observation. Based on these discussions, I try to develop the efficient thermal catalyst by a topological control.Second approach is developing photocatalyst for DRM (Chapter 3 and 4). Even though previous studies reported photo-assisted DRM, no research, which realized the photocatalytic DRM by using light without heat, has yet been established. Further, previous works could not elucidate the photocataltic DRM process. Therefore, I develop a photocatalytic system from the viewpoint of band structure of semiconductors and co-catalyst modification to drive DRM by using light as an energy source.

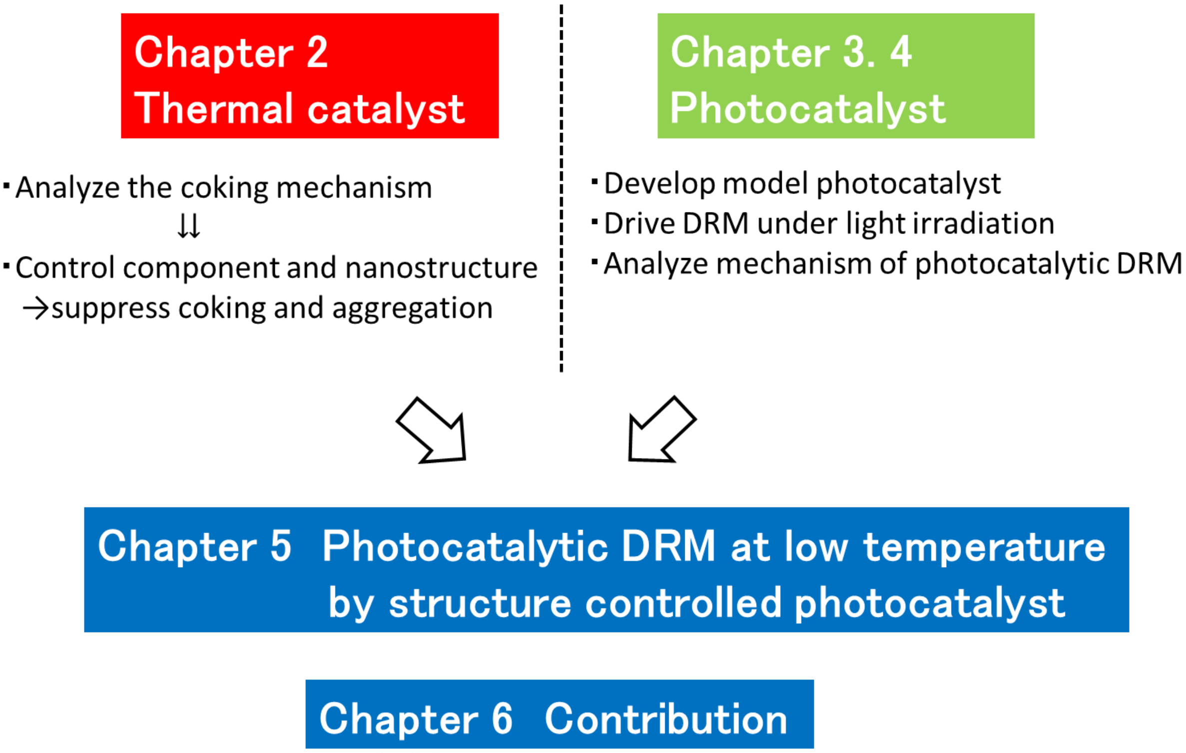

In Chapter 5, I combine the knowledge of Chapter 2-4 to establish efficient photocatalytic DRM system on the basis of nano-structural and band-structural control.

In Chapter 6, I will explain the philosophical contribution of my thesis to the field of materials and catalysis science. Finally, in Chapter 7, I summarize this thesis.

2. Topologically immobilized catalysis centre for long-term stable DRM at low temperature

This chapter introduces the value of topologically immobilized nanostructure of metal and oxide surfaces for driving DRM at low temperature. Methane reforming at low temperatures is of growing importance to mitigate the environmental impact of the production of synthesis gas, but it suffers from short catalyst lifetimes due to the severe deposition of carbon byproducts. Herein, I introduce a new class of topology-tailored catalyst in which tens-of nanometer-thick fibrous networks of Ni metal and oxygen-deficient Y_2O_3 are entangled with each other to form a rooted structure, i.e., Ni#Y_2O_3. We demonstrate that the rooted Ni#Y_2O_3 catalyst stably promotes the carbon-dioxide reforming of methane at 723 K for over 1000 h, where the performance of traditional supported catalysts such as Ni/Y_2O_3 diminishes within 100 h due to the precluded mass transport by accumulated carbon byproducts. The long-term stable methane reforming over the rooted catalyst is ultimately attributed to the topologically immobilized Ni catalysis centre and the synergistic function of the oxygen-deficient Y_2O_3 matrix, which successfully inhibits the accumulation of byproducts.

2.1 Introduction

The catalytic conversion of the major component in biogas and natural gas, methane (CH_4), into valuable synthesis gas consisting of CO and H_2, is of increasing importance to establish a hydrogen-based society as well as for petroleum-free carbon resource management. Meanwhile, it is acknowledged that deposition of solid-state carbon byproducts (carbon deposition) is a significant drawback for CH_4 reforming[7, 23, 24, 59, 64-66].In order to suppress carbon deposition, CH_4 reforming is currently conducted at high temperatures (>1073 K) and as a result, suffers from rapid catalyst degradation and huge energy consumption. In contrast, CH_4 reforming at 873 K or lower temperatures may be favored to mitigate the catalyst degradation and environmental impacts. However, the carbon deposition is strongly accelerated at low temperatures via CH_4 decomposition ($CH_4 = C(s) + 2H_2$) and/or CO disproportionation ($2CO = C(s) + CO_2$), which inhibits mass transport and shortens catalyst lifetime[7, 24] .Although CO_2 dry reforming of CH_4 (DRM: $CH_4 + CO_2 = 2CO + 2H_2$) is highly promising among the different types of CH_4 reforming in terms of the efficient use of carbon feedstocks and the reduction of CO_2 emissions[7, 67-73] , DRM is the most readily subjected to carbon deposition, especially at low temperatures. Recently, several strategies of designing core–shell structures and/or doping with other additive elements have been proposed to suppress undesirable carbon deposition[14, 74-76] ,yet it still remains a challenge. Herein, we propose a material design strategy to preclude carbon deposition via tailoring the three-dimensional topology of metal/oxide nanocomposites. We demonstrate that a nanocomposite, consisting of entangled networks of tens-of nanometre-thick fibrous phases of nickel metal and oxygen defficient yttrium oxide, i.e., Ni#Y_2O_3, can be prepared by utilizing nanophase-separation of a Ni–Y alloy in an oxidative atmosphere. The Ni#Y_2O_3 catalyst can activate CO_2 and CH_4 from a low temperature of 623 K (Figure 2.1) and stably promote the DRM reaction at 723 K (low-temperature DRM; abbreviated as LT-DRM hereafter) for over 1000 h, whereas traditional supported catalysts such as Ni/Al_2O_3 and Ni/Y_2O_3 diminish the catalytic performance within 100 h.

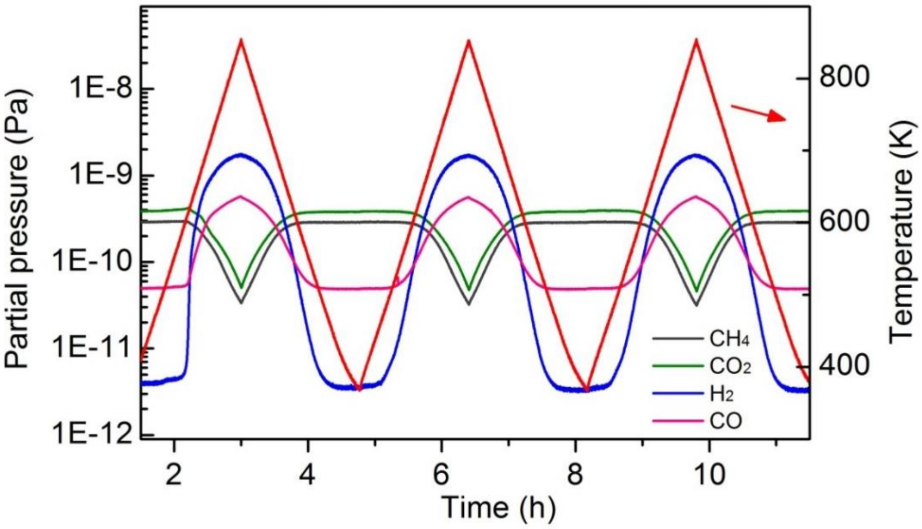

Figure 2.1 Low-temperature DRM over the Ni#Y_2O_3 catalyst at different temperatures. Temperature range: 373 K to 873 K.

Advanced characterizations, including in situ transmission electron microscopy, elucidate that particle migration occurs in the supported catalysts in the reaction atmosphere, and the migrating metal nanoparticles act as a major catalyst centre for the widespread growth of fibrous carbon byproducts. However, the Ni catalysis centre of the Ni#Y_2O_3 catalyst is, like a tree deeply rooted in the ground, topologically immobilized by entanglement with the oxygen-deffcient Y_2O_3 matrix, which can eliminate carbon byproducts to realize long-term stable DRM performance.

2.2 Experimental

2.2.1 Catalyst preparation

Elemental Ni metal (The Nilaco Corporation) and Y metal (Rare Metallic Co., Ltd.) were melted at different atomic ratios using an arc torch in an Ar atmosphere (Ar purity: 99.9999%) to synthesize Ni-Y alloy precursors with different atomic ratios (Ni_5Y, Ni_3Y, Ni_2Y, NiY and NiY_3). The prepared Ni-Y alloy ingot was ground in a mortar and was sieved to obtain powder precursors with an average particle size of 50-60 μm. After the Ni-Y alloy precursors were heated in a gas stream consisting of CO, O_2 and Ar (Japan Fine Products Corporation; 2 vol% of CO, 1 vol% of O_2 and 97 vol % of Ar; gas flow rate: 60 mL min-1) at 873 K for 12 hrs, we obtained the Ni-Y_2O_3 composites with different Ni/Y ratios. The Ni#Y_2O_3 catalyst was obtained from a NiY (Ni:Y=1:1) alloy precursor. Conventional supported catalysts of Ni/Al_2O_3 and Ni/Y_2O_3 were prepared as control by the impregnation method. An aliquot of 0.8 g of $Ni(NO_3)_2{\cdot}6H_2O$

(Sigma-Aldrich Co., Llc; 99.999%) was first dissolved in 20 mL of ethanol (Kishida Chemical Co., Ltd.; 99.5%). Then, 0.3 g of either Al_2O_3 or Y_2O_3 powder (Sigma-Aldrich Co., Llc.; nanopowder,

2.2.2 Characterization

The X-ray diffraction (XRD) patterns were recorded on an X-ray diffractometer (Panalytical X'Pert PRO) with Cu-Kα radiation. The surface morphologies of the samples were observed with a scanning electron microscope (SEM, Hitachi SU-8230, accelerating voltage: 10 kV). A focused ion beam (FIB, JEM-9320) was employed to section the sample. Transmission electron microscope (TEM) images were obtained with a JEOL 2100-F microscope with an operating voltage of 200 kV. Raman spectra were acquired with a Renishaw inVia 2000 Raman Microscope by using an Ar ion laser at a wavelength of 514.5 nm. Hard X-ray photoemission spectroscopy (HAXPES) was conducted by using an X-ray with a photon energy of 5.95 keV at the undulator beamline BL15XU of SPring-8, Japan. The 4 HAXPES spectra were acquired at room temperature under UHV using a hemispherical electron energy analyser (VG SCIENTA R4000). The binding energy was referenced to the Fermi edge of a Au thin film. H_2 pulse adsorption measurements were performed with a Micromeritics AutoChem II 2920 instrument. Aliquots of 0.1 g of the catalysts were first reduced in a H_2-Ar gas mixture (5 vol% H2) at 673 K for 4 hrs prior to the H_2 adsorption. Pulses of H_2-Ar gas were introduced into the quartz reactor at 308 K. The total H_2

uptake was recorded until no further consumption of H_2 was recognized. H_2-O_2 titration was also performed with the Micromeritics AutoChem II 2920 instrument. An aliquot of 0.1 g of the sample was pretreated in a H_2-Ar gas mixture at 673 K for 4 hrs. Pulses of O_2-He (10 vol% O_2) gas were then introduced into the reactor. The consumption amount of O_2 was utilized to calculate the reduction degree by assuming the stoichiometric reoxidation of Ni0 to NiO. The Ni dispersion degree was calculated based on the number of exposed surface Ni atoms with respect to the total number of Ni atoms in the catalyst. In-situ TEM was performed with a JEM-1000K RS TEM (JEOL) at Nagoya University, which was equipped with a specially designed atmosphere-controllable cell. The sample was exposed to a reactant gas consisting of equimolar amounts of CH_4 and CO_2 at 200 Pa.

2.2.3 Catalytic tests

Low-temperature dry reforming of methane (LT-DRM) was performed on a fixed-bed flow reactor at atmospheric pressure. An aliquot of 0.1 g of the catalyst was loaded in a quartz reactor with an inner diameter of 10 mm. Then, a gas mixture of CH_4, CO_2 and Ar (CH_4: CO_2:Ar = 1:1:98 in vol%) at a flow rate of 100 mL min-1 was introduced into the reactor. The temperature was raised to the desired reaction temperature, typically 723 K. The reaction effluents were analysed using a gas chromatograph equipped with an activated charcoal column. The catalytic performance over 6 hrs was typically used for the quantitative comparisons in the performance of different catalysts. The calculation methods for the consumption, formation and conversion rates are presented in the Equations 2.1-2.7. The turn over frequency (TOF) was evaluated by using the same fixed-bed flow reactor. Both of the CH_4 and CO_2 conversion rates were always adjusted below 10 % by changing the catalyst weights. The TOF was finally calculated based on the conversion after the LT- 5 DRM reaction of 6 hrs.

$$CH4\ Conv.[\%] = \frac{mol\ of\ CH4\ imput - mol\ of\ CH4\ output}{mol\ of\ CH4\ input} \times 100 \qquad (2.1)$$

$$CO2\ Conv.[\%] = \frac{mol\ of\ CO2\ imput - mol\ of\ CO2\ output}{mol\ of\ CO2\ input} \times 100 \qquad (2.2)$$

$$CH4\ Consumption\ Rate = flow\ rate\ of\ CH4\ input\ \times CH4\ conv. \quad (2.3)$$

$$CO2\ Consumption\ Rate = flow\ rate\ of\ CO2\ input\ \times CO2\ conv. \quad (2.4)$$

$$H2\ Formation\ Rate = flow\ rate\ of\ CH4\ input\ \times \frac{mol\ of\ H2\ output}{mol\ of\ CH4\ input} \quad (2.5)$$

$$\begin{aligned} &CO\ Formation\ Rate \\ &\qquad = (CH4\ input \\ &\qquad + CO2\ input) \times \frac{mol\ of\ H2\ output}{(mol\ of\ CH4\ input + mol\ of\ CO2\ input)} \quad (2.6) \end{aligned}$$

$$H2/CO\ ratio\ = \frac{H2\ formation\ rate}{CO\ formation\ rate} \quad (2.7)$$

2.3 Results and discussion

2.3.1 Characterization

The preparation processes for different metal/oxide catalysts are shown in Fig. 1. Traditional supported catalysts including Ni/Y_2O_3 and Ni/Al_2O_3 were prepared by a routine impregnation method (Fig. 2.2 a). The $Ni\#Y_2O_3$ catalyst was obtained from a Ni–Y (Ni: Y = 1 : 1) alloy precursor consisting of Ni metal and oxyphilic Y metal (Fig. 2. 3). The Ni–Y alloy was heated at 873 K in a gas mixture of CO and O_2 (CO : O_2 =2 : 1 in volume%) to promote nanophase separation from a uniform alloy into a nanocomposite consisting of metal Ni and Y_2O_3, namely, Ni#Y_2O_3. The Ni#Y_2O_3 nanocomposite comprised an entangled network of fibrous metal Ni and Y_2O_3, which further sprouted out of the bulk to develop a rooted structure (Fig. 2.2. b)[77]. As the control catalyst, different Ni–Y_2O_3 nanocomposites with different Ni/Y ratios of 5/1, 3/1, 2/1 and 1/3 were prepared from the corresponding Ni–Y alloy precursors (Ni_5Y, Ni_3Y, Ni_2Y and NiY_3, respectively; Fig. 2.4 and 2.5) via the same atmospheric treatment as for the Ni#Y_2O_3.

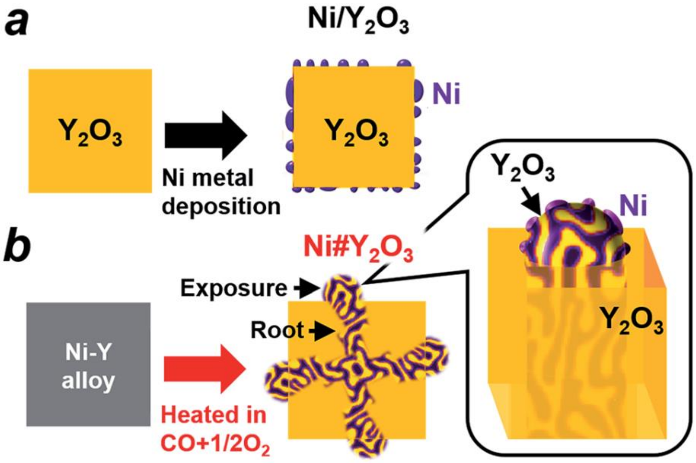

Figure 2.2 Designing metal/oxide catalysts with different topologies. (a) Traditional supported catalysts such as Ni/Y_2O_3 are prepared by depositing Ni nanoparticles onto the support surface(b).

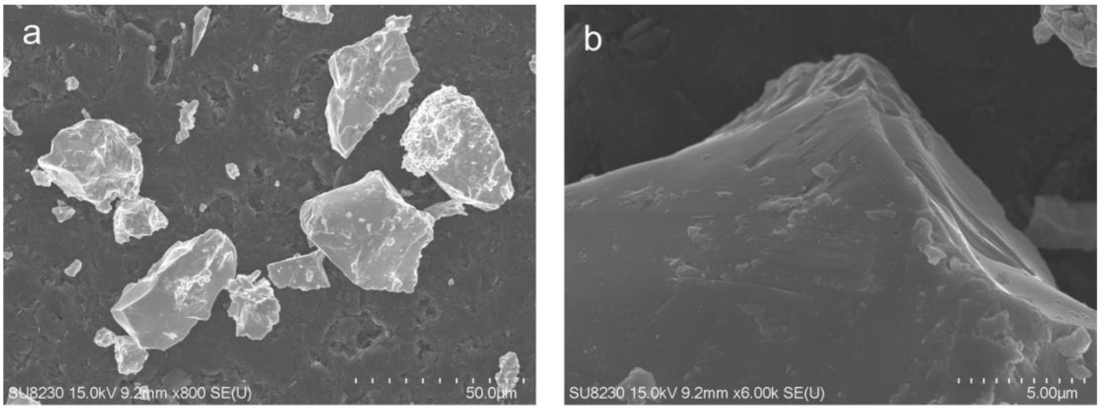

Figure 2.3 SEM images of the NiY (NiY = 1:1) alloy particles. (a) The particle morphology and (b) the outer surface.

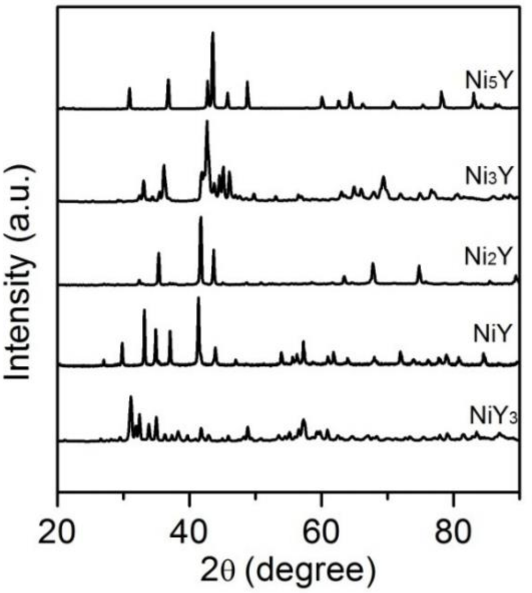

Figure 2.4 XRD patterns for the alloy precursors of Ni_5Y, Ni_3Y, Ni_2Y, NiY and NiY_3.

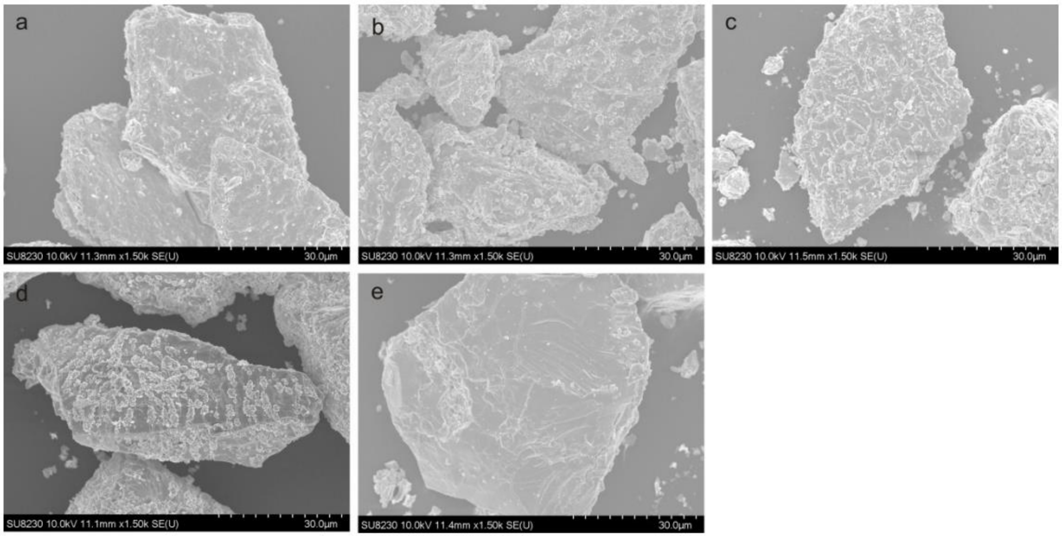

Figure 2.5 SEM images of the Ni-Y_2O_3 nanocomposites obtained from different Ni-Y alloy precursors with different Ni/Y ratios: (a) Ni/Y = 5/1,(b) Ni/Y = 3/1, (c) Ni/Y = 2/1, (d) Ni/Y = 1/1 and (e) Ni/Y = 1/3.

The microstructure of the Ni#Y_2O_3 catalyst was characterized with a scanning electron microscope (SEM). A number of precipitates were observed on the surface of the Ni#Y_2O_3 particles (Fig. 2.6 a). The cross-section SEM images demonstrated that the precipitates arose from the exposure of a rooted structure that propagated from the bulk to the surface (Fig. 2.6 b). High-magnification SEM and STEM observations further showed that the rooted structure was composed of fibrous Niand Y_2O_3 phases (Fig. 2.6 c and d).

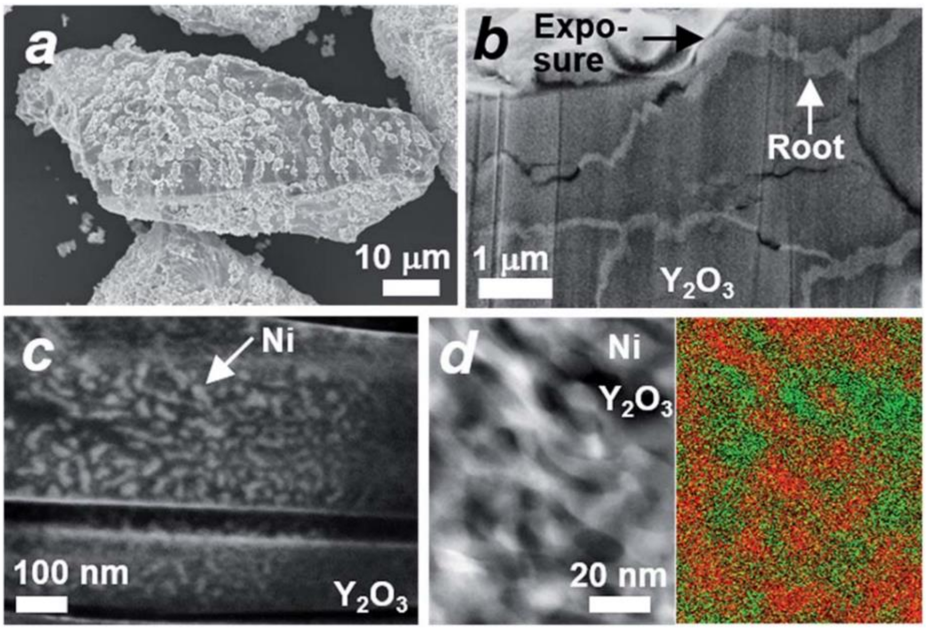

Figure 2.6 Micro- and nanostructures of the rooted catalysts. (a) SEM image of one of the Ni#Y_2O_3 particles. (b) Cross-section SEM image of one of the Ni#Y_2O_3 particles, showing the distribution of the rooted structure in the bulk. The black arrow shows one of the exposures of the rooted structure. (c) High-magnification SEM image of the rooted structure shown in (b). (d) High-magnification HAADF STEM- (left) and elemental mapping images (right) of the rooted structure. The redand green areas in the mapping image correspond to the Ni- and Y_2O_3 phases, respectively.

2.3.2 Activity of low temperature DRM

We tested the Ni#Y_2O_3 catalyst for LT-DRM in comparison to the other Ni-based catalysts prepared from different alloy precursors (Fig. 2.7 a).

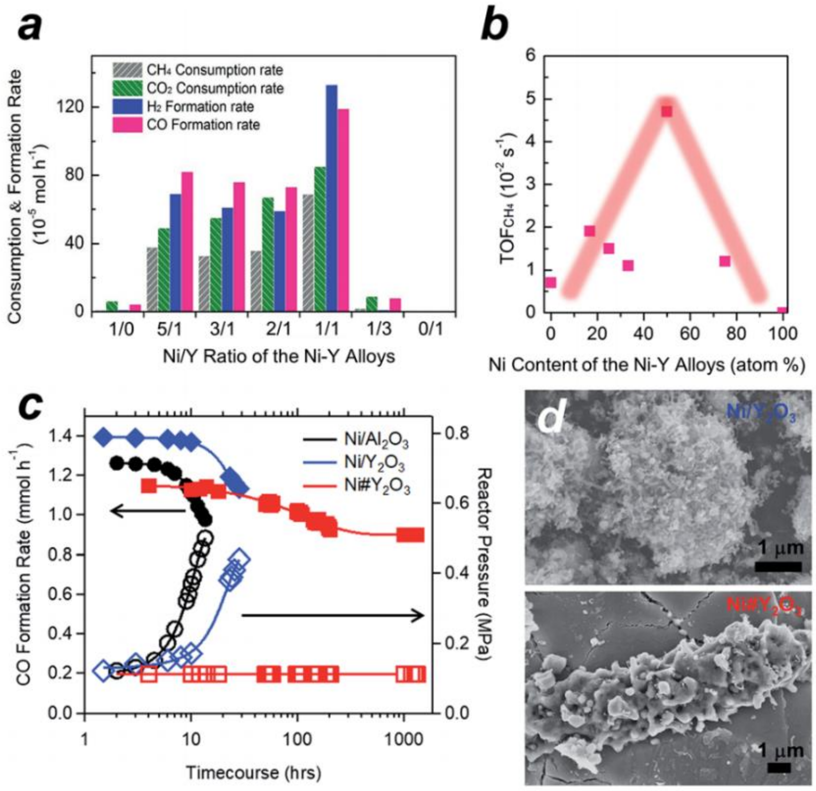

Figure 2.7 LT-DRM performance of the Ni#Y_2O_3- and other Ni-based catalysts. Catalyst amount = 0.1 g; reaction temperature = 723 K; CH_4/ CO_2/Ar = 1/1/98 in vol%; flow rate = 100 mL min1 . (a) CO/H_2 formation rates and CH_4/CO_2 consumption rates for the Ni–Y_2O_3 composites with different Y contents. The Ni#Y_2O_3 corresponds to the Ni/Y ratio of the Ni–Y alloy = 1/1. (b) The turn-over frequencies (TOFs) towards CH_4 conversion over the Ni–Y_2O_3 composites with different Y contents. The Ni#Y_2O_3 corresponds to the Ni content of the Ni–Y alloy = 50%. (c) CO formation (left axis) and reactor pressure (right axis) for the Ni#Y2O3- and supported Ni catalysts. (d) SEM images of the Ni/ Y_2O_3- and Ni#Y_2O_3 catalysts, 6 h after subjected to the LT-DRM atmosphere.

Pure Ni-powder exhibited very low activity, due to the low dispersion degree of the active Ni sites (Table 2.1 and Fig. 2.8). The different Ni–Y_2O_3 composites also exhibited lower consumption- and formation rates than the Ni#Y_2O_3 catalyst. This should be attributed to the overgrowth of Ni or Y_2O_3 during the atmospheric processing of CO/O_2 (Fig. 2.8).

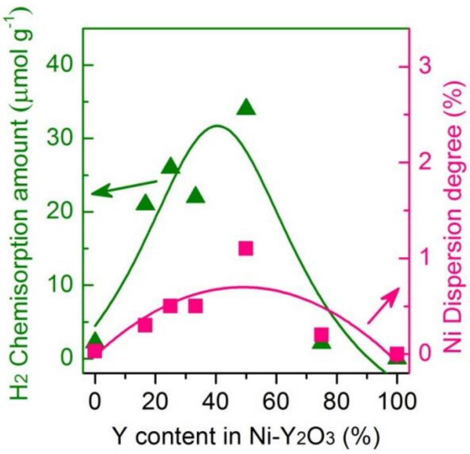

Figure 2.8 Influence of the Y content on H_2 chemisorption and Ni dispersion for Ni-Y_2O_3 composites.

Table 2.1 Physicochemical properties of the Ni-based catalysts.

Sample	Reduction degree[a] (%)	H_2 chemisorption amount[b] (μmol g^{-1})	Ni dispersion degree[c] (%)	Ni particle diameter[e] (nm)	Mean Ni size[f] (nm)	Mean Ni size[g] (nm)
Ni-powder	/	2.2	0.03[d]	/	/	/
Ni#Y_2O_3	25	34	4.5	21	19	20
Ni/Al_2O_3	63	74	3.9	24	22	25
Ni/Y_2O_3	69	101	4.9	20	19	22

The CH_4 and CO_2 consumption rates over the Ni#Y_2O_3 catalyst were close to half the value of the CO and H_2 formation rates, showing that the LT-DRM was promoted in a nearly stoichiometric pathway. We then evaluated the turnover frequency (TOF) of Ni#Y_2O_3 and the different Ni-based catalysts towards CH4 conversion (i.e. TOF_{CH4} , Table 2.2). The Ni#Y_2O_3 catalyst exhibited a much higher TOF_{CH4} than the other catalysts prepared from different alloy precursors (Fig. 2.7 b). The Ni#Y_2O_3 catalyst was optimized in terms of composition to achieve the highest LT-DRM performance.

Table 2.2 Catalyst amounts and the conversions for the TOF calculation.

Sample	Amount of catalyst used (mg)	CH_4 Conv. (%)	TOF_{CH4} [10^{-2} s^{-1}]
Ni-powder	100	0.4	0.7
Ni-Y_2O_3 (Ni/Y=5/1)	25	2.7	1.9
Ni-Y_2O_3 (Ni/Y=3/1)	27	2.9	1.5
Ni-Y_2O_3 (Ni/Y=2/1)	25	1.6	1.1
Ni#Y_2O_3 (Ni/Y=1/1)	7.0	3.0	4.7
Ni-Y_2O_3 (Ni/Y=1/3)	100	0.7	1.2
Y_2O_3	/	/	/
Ni/Al_2O_3	1.1	5.9	27
Ni/Y_2O_3	1.2	4.9	15

We finally compared the Ni#Y_2O_3 catalyst with traditional supported catalysts in terms of long-term stability for LT-DRM (Fig. 2.7 c). Note that the size of the Ni sites of Ni#Y_2O_3 (19 nm) was close to those of the supported catalysts including Ni/Y_2O_3 (19 nm) and Ni/Al_2O_3 (22 nm) (Table 2.1 and Fig. 2.9). However, the Ni#Y_2O_3 catalyst stably promoted LT-DRM at 723 K for over 1000 hours, keeping the reactor pressure constant. A slight drop during the first 100 hours was observed, likely because the catalyst needed an initiation to reach a balance of carbon deposition and re-oxidation. In contrast, the traditional supported catalysts such as Ni/Al_2O_3 and Ni/Y_2O_3 showed rapid lowering in CO formation although they exhibited superior catalytic activity in the early stages.

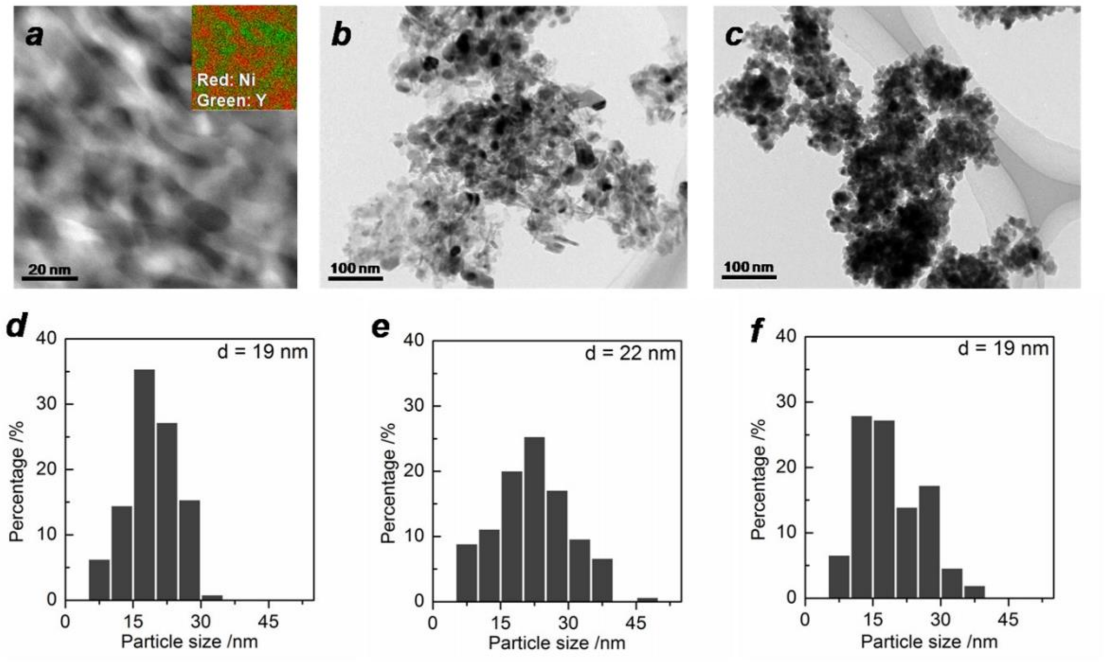

Figure 2.9 TEM observation and Ni particle size distribution for Ni#Y_2O_3, Ni/Al_2O_3, Ni/Y_2O_3. TEM observation: (a) Ni#Y_2O_3, (b) Ni/Al_2O_3, (c) Ni/Y_2O_3; Ni particle size distribution: (d) Ni#Y_2O_3, (e) Ni/Al_2O_3, (f) Ni/Y_2O_3. The mean Ni particle size was obtained by counting ca. 150 particles for each sample.

A similar trend was also observed in dense gas conditions (Fig. 2.10; catalyst amount = 0.1 g; reaction temperature = 823 K; $CH_4/CO_2/N_2$ = 10/10/5 in vol%; flow rate = 25 mL/min). The initial CH_4 and CO_2 conversions in LT-DRM were 49% and 38% over the supported Ni/Al_2O_3 catalyst, respectively, but rapidly decreased down to 12% and 9.1% after 10 h. However, our $Ni\#Y_2O_3$ catalyst initially exhibited 12% and 20% for the CH_4 and CO_2 conversions, respectively, and kept them higher than 7.5% and 14% even at a time course of 100 h. The reactor pressure containing the supported catalysts increased as the conversion rates decreased, which was a typical trend observed when the reactor is clogged by carbon deposits (Fig. 2.7 c and the inset in Fig. 2.10). In addition, a higher TOF_{CH4} was exhibited by the supported catalysts (Table 2.2), but the carbon balance was much larger than unity (i.e. [CH_4 consumption rate + CO_2 consumption rate]/CO formation rate > 1.0; Table 2.3). The provided carbon species of CH_4 and/or CO_2 were more readily converted into carbon deposits than CO over the supported catalysts. Unlike the supported catalysts, $Ni\#Y_2O_3$ exhibited a unity of carbon balance to achieve full conversion of CH_4 and CO_2 into CO without carbon deposits.

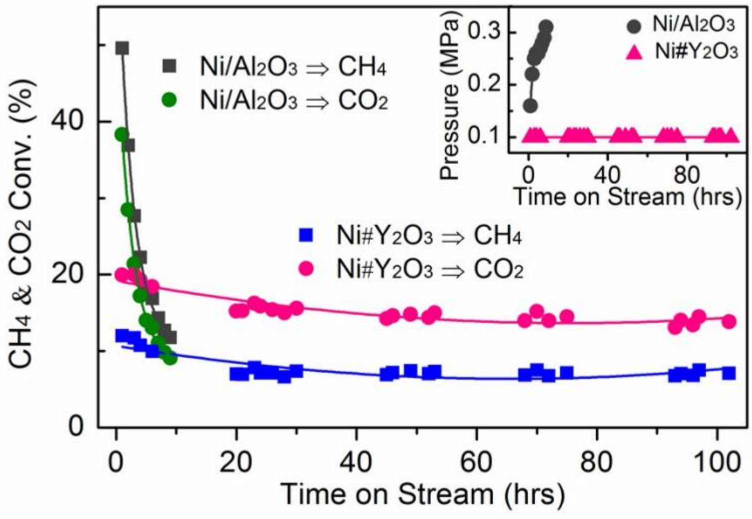

Figure 2.10 Stability of the Ni#Y_2O_3 in LT-DRM in a dense gas condition.

Table 2.3 LT-DRM performance of different catalysts in a dense gas condition.

Sample	CH_4 Consumption Rate [mmol h^{-1}]	CO_2 Consumption Rate [mmol h^{-1}]	H_2 Formation Rate [mmol h^{-1}]	CO Formation Rate [mmol h^{-1}]	Carbon balance
Ni/Al_2O_3	15	10	18	7.7	3.2
Ni/MgO	9.1	8.7	14	12	1.3
Ni#Y_2O_3	3.1	4.8	4.5	7.8	1.0

2.4.1 Elucidation of mechanisms

In order to elucidate the origin of the carbon-deposition tolerance of Ni#Y_2O_3, we performed different characterizations of the catalysts that were exposed to the LT-DRM atmosphere for 6 h (see Fig. 2.11 for XRD). SEM observation showed that the supported Ni/Al_2O_3 as well as Ni/Y_2O_3 were heavily covered with fibrous deposits (Fig. 2.7 d and 2.12). The Ni#Y_2O_3 catalyst was free from fibrous deposits, instead it was thinly coated with a deposit layer (Fig. 2.7d). Hard X-ray photoemission spectroscopy (HAXPES: Fig. 2.13) and thermogravimetry (TG: Fig. 2.14) showed that the total amount of carbon deposits on the Ni#Y_2O_3 catalyst was less than that on the Ni/Al_2O_3- or Ni/Y_2O_3 catalysts.

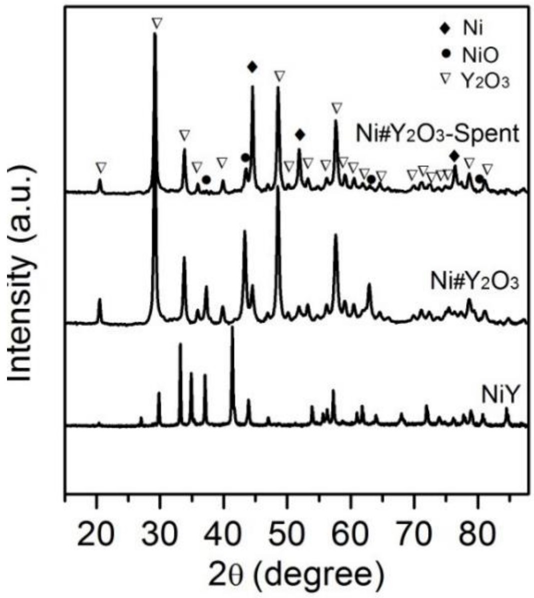

Figure 2.11 XRD patterns for the NiY alloy precursor, fresh Ni#Y_2O_3 and a Ni#Y_2O_3 catalyst used for the LT-DRM for 6 hrs.

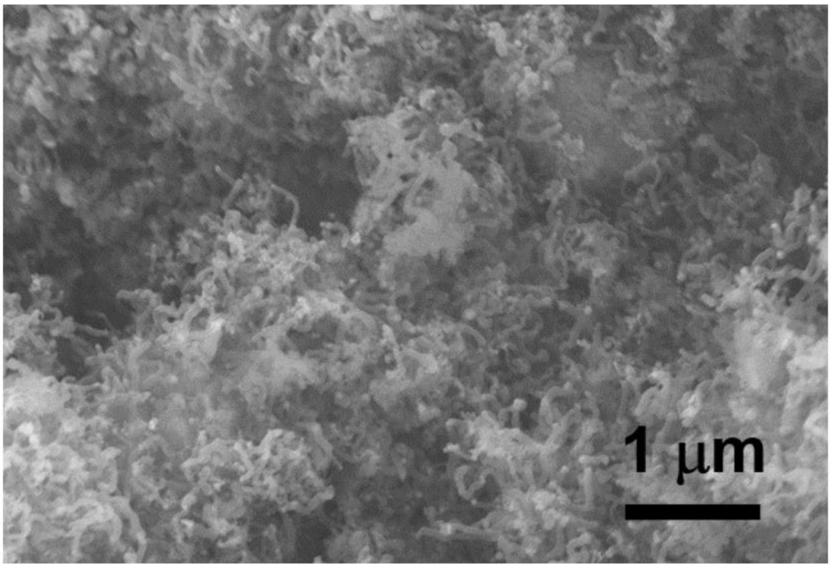

Figure 2.12 SEM image of a used Ni/Al_2O_3 catalyst.

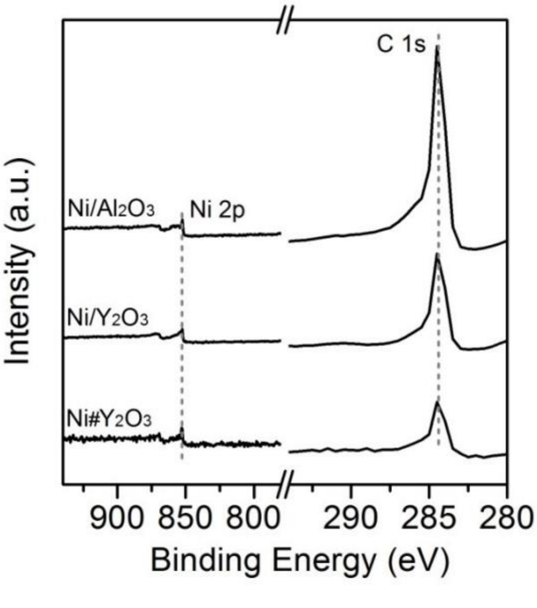

Figure 2.13 Hard X-ray photoemission spectra (HAXPES) in the Ni2p- and C1s regions for the different catalysts after LT-DRM. The C1s photoemission intensities from the used catalysts increased in the following order: Ni#Y_2O_3< Ni/Y_2O_3< Ni/Al_2O_3, while the Ni 2p intensity was the same. The Ni#Y_2O_3 catalyst was less covered with carbon species than any of the other supported catalysts.

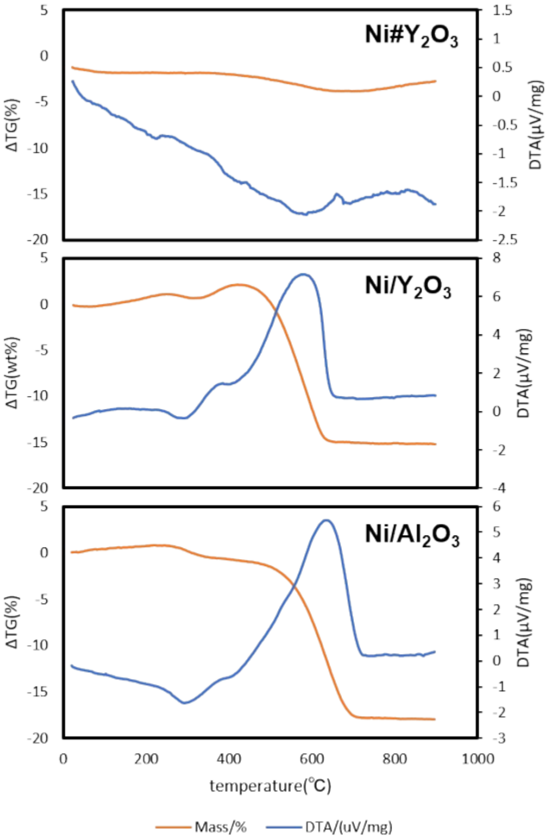

Figure 2.14 Thermo-gravimetry (TG) and differential temperature analysis (TDA) results for 14 Ni#Y_2O_3, Ni/Y_2O_3 and Ni/Al_2O_3, at elevating temperatures in an air stream. In advance to the TG/DTA experiments, each of the materials was first subjected to the diluted LT-DRM atmosphere (CH_4:CO_2:Ar=1:1:98; exposure for 12 hours) to promote carbon depositions.

2.4.2 Direct observation of coking by in-situ TEM

We then conducted in situ TEM to shed light on the growth dynamics of the fibrous carbon in the LT-DRM atmosphere. The Ni/Al_2O_3 catalyst was exposed to a reactant gas consisting of equimolar CH_4 and CO_2 at 723 K with a pressure of 200 Pa, and observed with high-voltage in situ TEM (JEM-1000K RS

TEM (JEOL), Nagoya Univ.). In an aliquot taken 2 h after the exposure to the reactant gas, an onion-shell pattern from graphitic carbon was clearly recognized all the way around the supported Ni nanoparticles (Fig. 2.15 a). A series of in situ TEM snapshots show that this graphitic carbon layer was decomposed near at the Ni/Al_2O_3 interface, most likely by oxygen species donated from the Al_2O_3 support (Fig. 4b, see Movie S1[78]). The Ni nanoparticle in the field of view migrated away from the center to the bottom right through the missing part of the graphitic carbon layer.

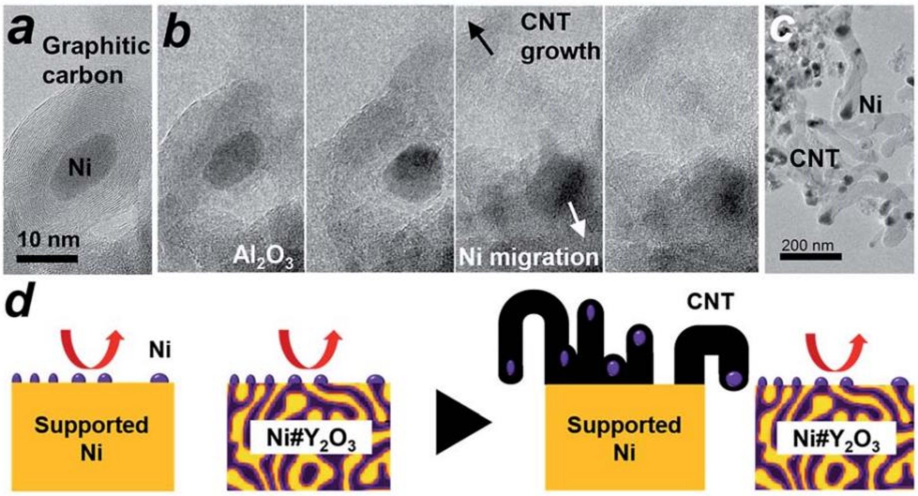

Figure 2.15 Dynamic TEM observations of carbon deposition. (a and b) In situ TEM images visualizing the growth of fibrous carbon deposits (carbon nanotubes: CNT) over the Ni/Al_2O_3 catalyst in the LT-DRM atmosphere. Snapshots of the CNT growth. Shooting interval: 2 seconds. (c) TEM image of the Ni/Al_2O_3 catalyst taken after subjection to LT-DRM for 6 h. (d) A model for the inhibited CNT growth over the Ni#Y_2O_3 catalyst due to the topological immobilization of the Ni catalysis centre.

Fig. 2.15 b also shows that a rapid growth of hollow, multiwalled carbon nanotubes (CNT) was triggered by the migration of Ni nanoparticles. It is acknowledged that Ni nanoparticles, when they are able to freely migrate around without a support, play the role of an efficient catalyst that promotes the growth of long-length CNT fibers from gaseous carbon species such as ethanol vapour via a vapour–solid (VS) mechanism.[79-81] The carbon species provided from the gaseous atmosphere are dissolved in the Ni bulk and recrystallize on the surface in the form of a CNT, which further grows along with the drift of the migrating nanoparticles. As a result of collective migration of the Ni nanoparticles, the Ni/Al_2O_3 and Ni/Y_2O_3 catalysts were densely covered with large numbers of CNTs (50 nm and 500 nm in average thickness and length, respectively; Fig. 2.15 c, 2.12 and 2.16) after exposure to the LT-DRM atmosphere for 6 h. Note that each of the grown CNT contained one Ni nanoparticle at one end as the growth front.

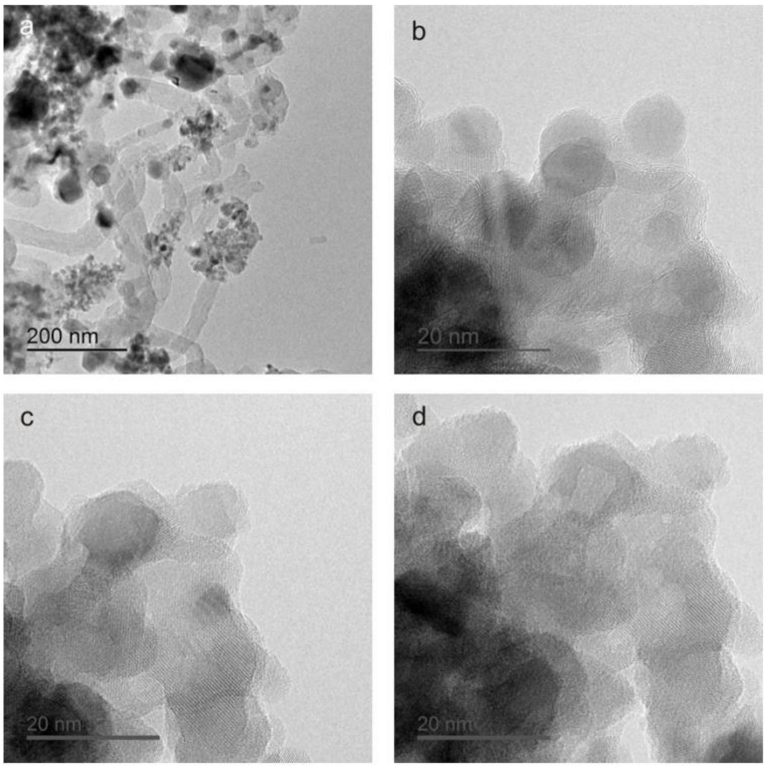

Figure 2.16 Conventional TEM- and in-situ TEM images for the Ni/Y_2O_3 catalyst. (a) The conventional TEM image for the Ni/Y_2O_3 catalyst 6 hrs after the exposure to the LT-DRM reaction. In-situ TEM images for the Ni#Y_2O_3 catalyst, (b)-(d): (b) 0.5 hrs, (c) 1.0 hrs; (d) 2.0 hrs after the exposure to a reactant gas of $CH_4/CO_2 = 1/1$ at 723 K with a pressure of 200 Pa.

2.4.3 Effect of oxygen in Y_2O_3

By contrast to the supported Ni nanoparticles, the Ni catalyst centre of Ni#Y_2O_3 is topologically immobilized due to entanglement with its Y_2O_3 counterpart, which can preclude particle migration and the accompanying CNT growth (Fig. 2.15 d, see Fig. 2.17). Moreover, the HAXPES results on the Ni 2p and O 1s regions showed that the Ni phase of Ni#Y_2O_3 was retained as metal in the LT-DRM atmosphere, whereas the Ni phase of Ni/ Y_2O_3 or Ni/Al_2O_3 was oxidized and/or carburized by CO_2 and/or CH_4 (Fig. 2.18). The HAXPES spectra in the Y 3d region demonstrated that the Y_2O_3 phase of Ni#Y_2O_3, unlike that of Ni/Y_2O_3, contained abundant oxygen vacancies (Fig.2.19).[82-84] The oxygen-deficient Y_2O_3 of Ni#Y_2O_3 not only topologically immobilizes the Ni catalysis centre, but also may contribute to the elimination of carbon deposits via atomic exchange at the Ni–Y_2O_3 interface. In addition, the carbon deposits formed on the catalysis centre of Ni#Y_2O_3 can be more readily oxidized than CNT or graphitic carbon because of their disordered and deficient nature.[7, 85]Therefore, the rooted Ni#Y_2O_3 catalyst, due to its topological advantages and the synergistic function with the oxygen deficient Y_2O_3, successfully inhibited carbon deposition and improved reaction stability.

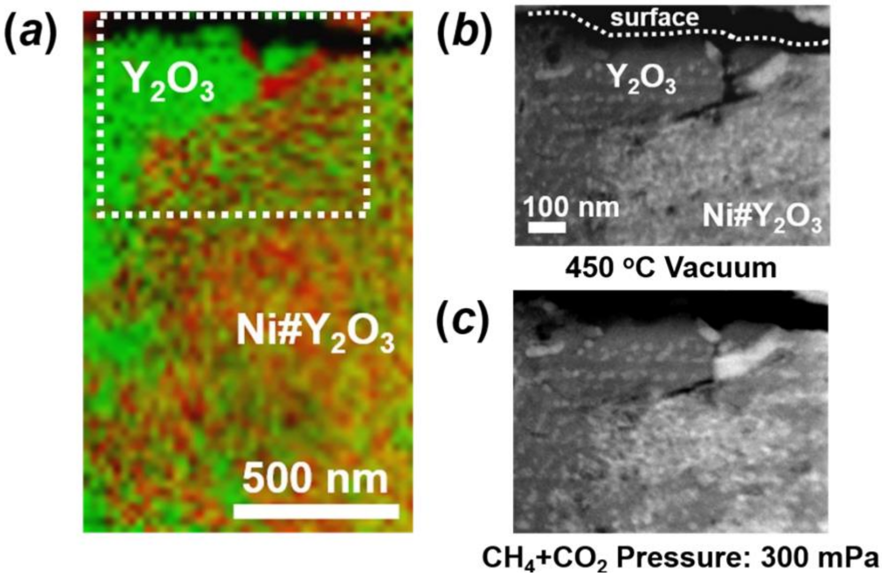

Figure. 2.17 The in-situ TEM observation on Ni#Y_2O_3. (a) Compositional mapping image of a section of Ni#Y_2O_3, (b) in-situ annular-dark field (HAADF) STEM image before the DRM reaction, (c) the same section after the simulated DRM atmosphere of 6 hours.

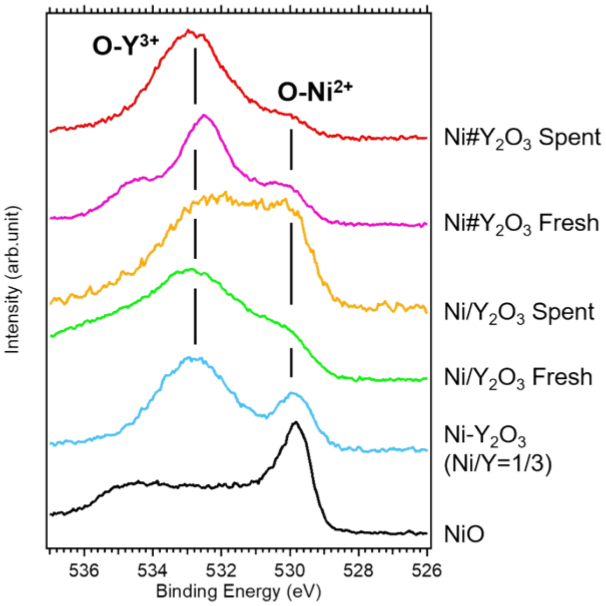

Figure. 2.18 HAXPES in the O 1s region. The HAXPES results show that the as-prepared (Fresh) Ni/Y_2O_3 material mostly contained the Y-O bond, but after exposure to the DRM

atmosphere, the O 1s emission from the Ni-O bond became more prominent (Ni/Y_2O_3 Spent), because of the oxidation of the Ni catalysis center. Unlike Ni/Y_2O_3, the O 1s emission from the Ni-O bond for Ni#Y_2O_3 was suppressed even after exposure to the DRM atmosphere. The HAXPES in the O1s region further showed that the Ni catalysis center of Ni#Y_2O_3 retained the metallic nature after exposure to the DRM atmosphere.

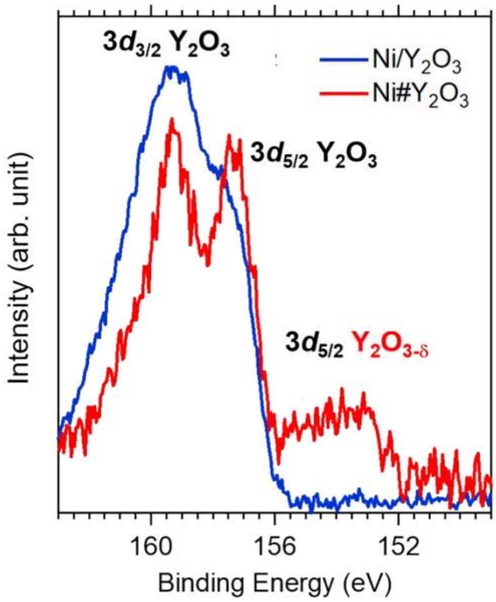

Figure 2.19 HAXPES in the Y 3d region for the spent Ni/Y_2O_3 and Ni#Y_2O_3 catalysts that were used for LT-DRM at 723 K for 6 hrs. The peaks at 157.3 eV and 159.3 eV respectively correspond to the Y 3d5/2- and Y 3d3/2 emissions from filled Y_2O_3. Unlike the HAXPES spectra for Ni/Y_2O_3, there was observed a broad peak in the spectrum for Ni#Y_2O_3, ranging 17 from 156 to 152 eV. This broad peak is attributed to a Y d5/2 emission from an oxygen deficient yttrium oxide, i.e, $Y_2O_{3-\delta}$ ($0< \delta$), in which the Y atoms have lower apparent valence than +3 to establish the electric neutrality.

2.5 Conclusion

In conclusion, we present a catalyst design strategy that involves alloy preparations coupled with atmospheric processing to promote the spontaneous formation of nanocomposites consisting of entangled networks of metal and oxides. By tuning the composition of alloy precursors and the processing atmosphere, we have successfully built a composite catalyst with a rooted nanostructure, namely, Ni#Y_2O_3. The Ni#Y_2O_3 catalyst realized an improved activity and long-term stability to LTDRM. In situ microscopic observations demonstrated that the carbon deposition occurring on traditional supported catalysts is attributable to the collective migration of metal nanoparticles. The catalysis centre of the Ni#Y_2O_3 is topologically immobilized by its oxygen-deficient Y_2O_3 counterpart to preclude particle migration and inhibit carbon deposition. Finally, the material design strategy of rooted catalysts reported here is not limited to the specific conversion of methane, but can be used for a broad range of practical applications, in which stable yet active metal/non-metal interfaces play a central role in performance, such as electrode catalysts for fuel cells and/or secondary batteries[86, 87].

3. Photocatalytic uphill conversion of natural gas beyond the limitation of thermal reaction systems

This chapter shows dry reforming of methane (DRM) is one of the key reactions to exploit natural gas feedstocks by catalytic conversion to synthesis gas ($CH_4 + CO_2 \leftrightarrow 2H_2 + 2CO$) to be used in the production of transportable liquid fuel. However, this reaction suffers from thermodynamic conversion limits and high thermal energy requirements. Herein, we report that a $SrTiO_3$-supported Rh catalyst (Rh/STO) efficiently promotes methane reforming under UV light irradiation without heat supply at low temperatures, which cannot be afforded with conventional thermal catalysis.

3.1 Introduction

Methane is anticipated as a sensible alternative to petroleum because of its abundance in the earth's crust, and yet it is precluded from use in the petrochemical industry due to the lack of cost-effective conversion methods to valued chemical products such as synthesis gas — that is, a mixture of CO and H_2. Although catalytic dry reforming of methane (DRM, $CH_4 + CO_2 \leftrightarrow 2CO + 2H_2$) is of particular interest to exploit the major components of natural gas, namely CH_4 and CO_2, current technologies require high temperatures (800–900 °C) to achieve sufficient conversion (more than 50 %) due to thermodynamic constrains (G_{298K} = +171 kJmol^{-1}). The high reaction temperatures, in turn, cause a significant rise in fuel costs, rapid catalyst degradation, and huge greenhouse gas emissions. Addition of O_2 to the DRM reactants can compensate for the endothermic process through the partial oxidation of methane, which is an exothermic process (POX: $CH_4 + 1/2O_2 = CO + 2H_2$; G_{298K} = -173 kJmol^{-1}). However, it is hard for such a combined DRM-POX process to avoid CH_4 losses due to the thermally favored methane combustion ($CH_4 + 2O_2 = CO_2 + 2H_2O$; G_{298K} = -801 kJmol^{-1}). Photon energy can be harvested from solar light and further converted into a storable form of chemical energy via uphill reactions, such as photocatalytic water splitting ($H_2O = H_2 + 1/2O_2$) and CO_2 reduction, at high efficiencies beyond the maxima allowed at thermodynamic equilibria[88-91]. Photocatalytic DRM can be a promising route that produces syngas with a high conversion beyond the limitation of thermal system. Previous attempts at photon-driven methane conversions were based on a kind of photo-assisted thermal catalysis over β-Ga_2O_3, MgO, $NaTaO_3$, TiO_2, SnO_2, or WO_3-based materials, and reactions were always conducted at elevated temperatures under additional illumination [60, 61, 63, 92, 93]. For all of these cases, the gain in methane conversion by light illumination was lower than 1 % without heating. Moreover, no evidence was provided that the reaction energy was, as expected for photocatalysis, supplied by photoexcitation of electron-hole pairs. Therefore, they are categorized as a photo-assisted DRM rather than truly photocatalytic [61, 63].

In the present study, we have focused on strontium titanate ($SrTiO_3$; STO) as a photocatalyst for DRM, since STO has a suitable band position to reduce CO_2 and to oxidize CH_4. Indeed, STO has demonstrated the ability to drive up-hill reaction such as water splitting and CO_2 reduction in aqueous media [55, 94]. We deposited highly dispersed rhodium (Rh) nanoparticles onto STO by a facile one-pot hydrothermal method using STO nanopowder and an aqueous solution of Rh ions. Rh nanoparticles that are strongly attached to the STO surface act as a catalytic center. Our Rh/STO catalyst exhibited high durability owing to its reduced coking property and suppression of Rh particle aggregation. The Rh/STO catalyst achieved more than 50 % conversion of DRM without additional heat input, which broke the limitation of thermal catalysis at 450 °C.

3.2 Experimental

3.2.1 Preparation of catalysts

To prepare the Rh/STO catalyst, hydrothermal treatment was employed. STO nanoparticles (WAKO Ltd.) and distilled water were put into a polytetrafluoroethylene (PTFE)-lined autoclave. Rh acetate dimer was also introduced into the reactor, where the Rh atom amount was set to 1 to 15 wt% versus STO. The reactor was introduced into a furnace and heated at 180 °C for 12 hours. After hydrothermal treatment, the powders were collected, washed by distilled water and dried at 90 ° C.

3.2.2 Characterization

X-ray diffraction (XRD) patterns were recorded by SmartLab (Rigaku) using Cu Kα X-rays. High-angle annular dark-field scanning transmission electron microscope (HAADF-STEM) observations and energy-dispersive X-ray spectroscopy (EDXS) elemental mapping were performed using an aberration-corrected electron microscope JEM-ARM200F (JEOL) operated at 120 kV.

3.2.3 Photocatalytic dry reforming of methane

After drying, powder samples were illuminated by a mercury-xenon lamp (Hg-Xe lamp, HAYASHI-REPIC Ltd., LA-410UV-5) under *in-situ* DRM conditions ($CH_4/CO_2/Ar$= 1/1/98 in vol%). After this irradiation treatment, Rh ions were reduced through photocatalytic reduction by STO. For the preparation of control samples of Ni/Al_2O_3 (Al_2O_3: KANTO CHEMICAL CO. INC.)and Rh/TiO_2 (P25), Rh/WO_3 (WO_3: KOJUNDO CHEMICAL CO. LTD), Rh/SnO_2, Rh/Bi_2WO_6, and Rh/ZrO_2 the metal chloride and oxides (with the amount of Rh or Ni atoms set to 10% versus oxides) were put into a glass beaker and heated to 90 °C with stirring. [13, 95] Since these semiconductors are acknowledged light absorbers in the visible- and/or UV range[31, 96].

After drying the solution, the powders were collected and introduced into a tube furnace with H_2 flow at 50 mL/min and heated to 500 ° C for 4 h. DRM was performed under ambient pressure in a flow reactor with a quartz window, which enabled us to irradiate the photocatalyst powder (Supplementary Figure. 1). The catalyst (5 mg) was put into the reactor, then the $CH_4/CO_2/Ar$ (1/1/98 in vol%) gas mixture was continuously introduced into the reactor with a flow rate of 10 mL/min. The products were evaluated by microgas chromatography (3000 Micro GC, Inficon). For a photocatalytic DRM test, the light source was a 150 W Hg-Xe lamp (HAYASHI-REPIC Ltd., LA-410UV-5). The absorbed photon number from the light source was calculated as $1.25*10^{17}$ (quanta/cm^2/sec).

3.3 Results and discussions

3.3.1 Characterization

High-angle annular dark field scanning transmission electron microscopy (HAADF-STEM) and energy-dispersive X-ray spectroscopy (EDXS) elemental mapping of the fabricated Rh/STO show that Rh nanoparticles in the range of 1-2 nm were highly dispersed onto STO (Fig. 3.1). XPS analysis on Rh/STO revealed that the valence state of Rh in Rh/STO was that of the metallic state rather than that of the oxide (Fig. 3.2).

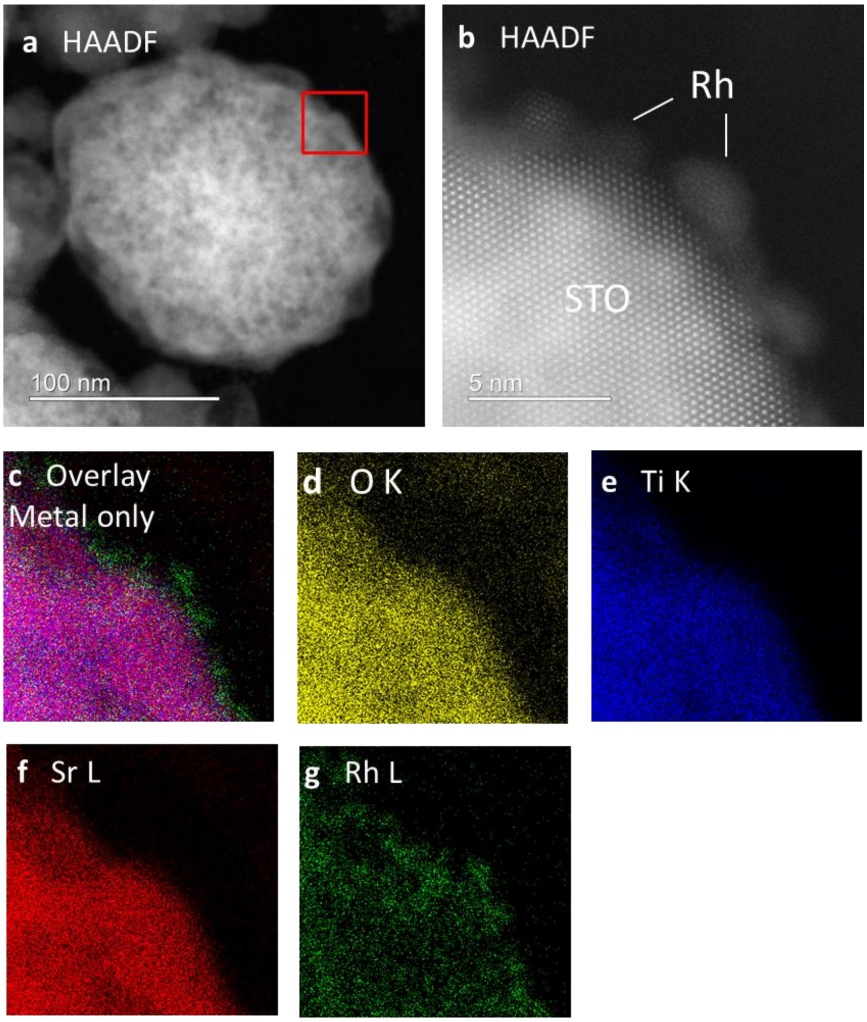

Figure 3.1 STEM and STEM-EDXS images of the Rh/STO. **a,** HAADF-STEM image of the Rh/STO. **b**, The magnified image of the red square in the panel **a**. **c-g,** STEM-EDXS elemental maps of the same region in the panel **b** for oxygen **d**, titanium **e**, strontium **f** and rhodium **g** and the overlay of metal elements **c**.

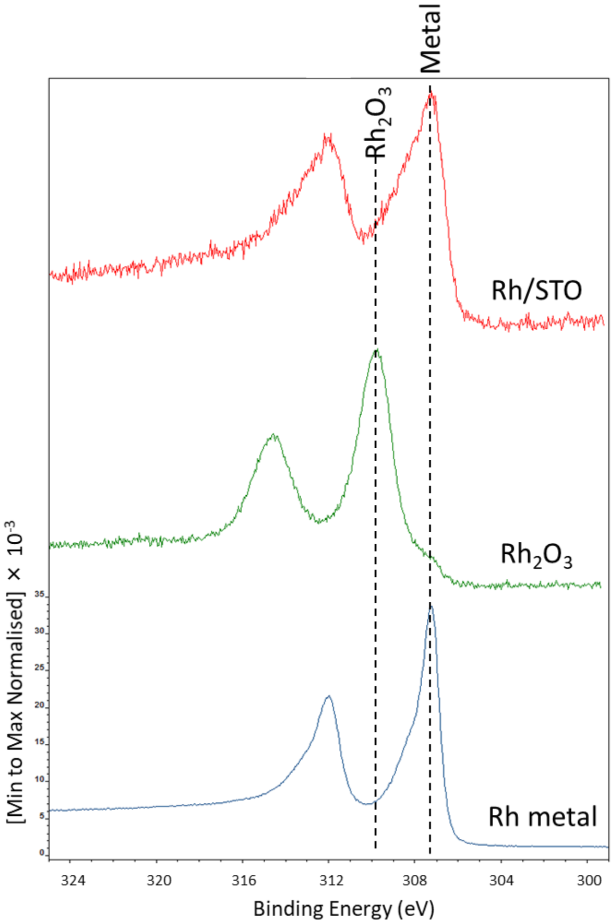

Figure 3.2 XPS of Rh metal (bottom, blue line), Rh_2O_3/STO (middle, green line), and Rh/STO (top, red line), respectively. The dashed lines indicate the representative peaks of Rh_2O_3 and Rh metal.

3.3.2 Performance of the catalysts

Firstly, we evaluated the performance of the Rh/STO catalyst under irradiation from a 150 W mercury-xenon lamp and under controlled temperature conditions using a flow reactor apparatus (Figure 3.3). Before conducting the detailed performance test, we investigated the Rh loading dependence on the catalytic activities and found the optimum amount to be around 10 wt% (Figure 3.4). However, the loaded amount of Rh onto STO should be lower than 10 % because all Rh source, which was added into a hydrothermal reactor, would not entirely be loaded on STO. To determine the accurate Rh amount, inductively coupled plasma (ICP) analysis was conducted and the Rh amount was determined to be 4.23 %. Figure 3.5 shows the performance of the optimized Rh/STO (10 wt%). The dashed line in this figure represents the limitation of thermal catalyst for DRM by thermal catalysts, which means that no catalyst could produce hydrogen over this line. Indeed, DRM performances under thermal conditions — in the present study corresponds to Rh/STO under dark conditions— were lower than the limitation of thermal catalyst (in blue area). In contrast, surprisingly, our Rh/STO produced more hydrogen than the thermal catalyst limit under light irradiation. We introduce 1 % CH_4 and 1 % CO_2 mixture in Ar balance gas (CH_4/CO_2 mixture gas) at a flow rate of 10 mL/ min, *i.e.* 4.5 μmol/min of CH_4 and CO_2 were introduced into a reactor. Under this flow rate of mixture gas, the hydrogen generation at 100 % DRM conversion would be 9 μmol/ min. It is noteworthy that the H_2 conversion by our Rh/STO exceeded 50 % under light irradiation even at a mild temperature below 200 °C. Bare STO did not produce any hydrogen under light irradiation, indicating that the Rh particles on the STO surface act as an active catalytic center. These results strongly imply that our

Rh/STO causes the DRM reaction only under light irradiation, without the input of external heat.

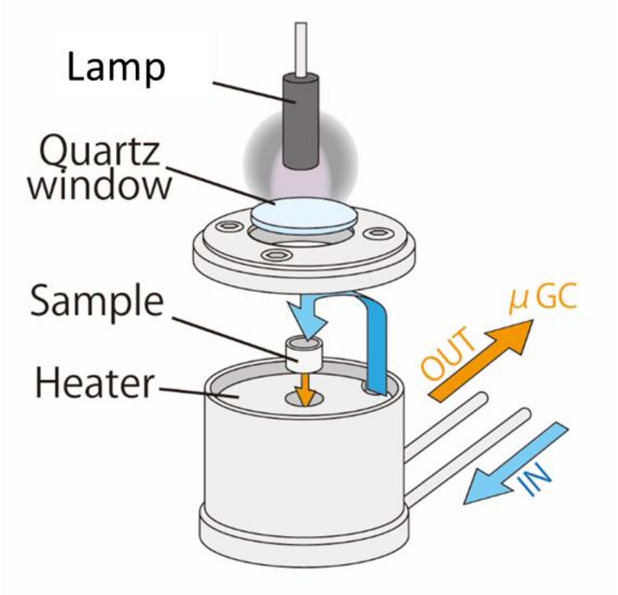

Figure 3.3 Schematic illustration of the DRM reactor.

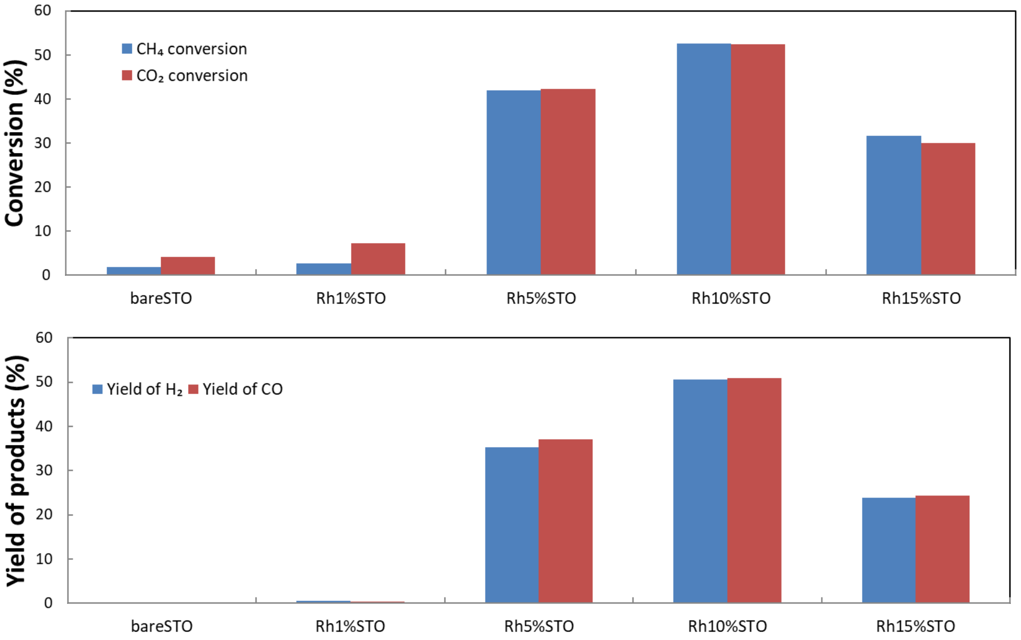

Figure 3.4 DRM performance of Rh/STO samples with different Rh loading amount under UV irradiation.

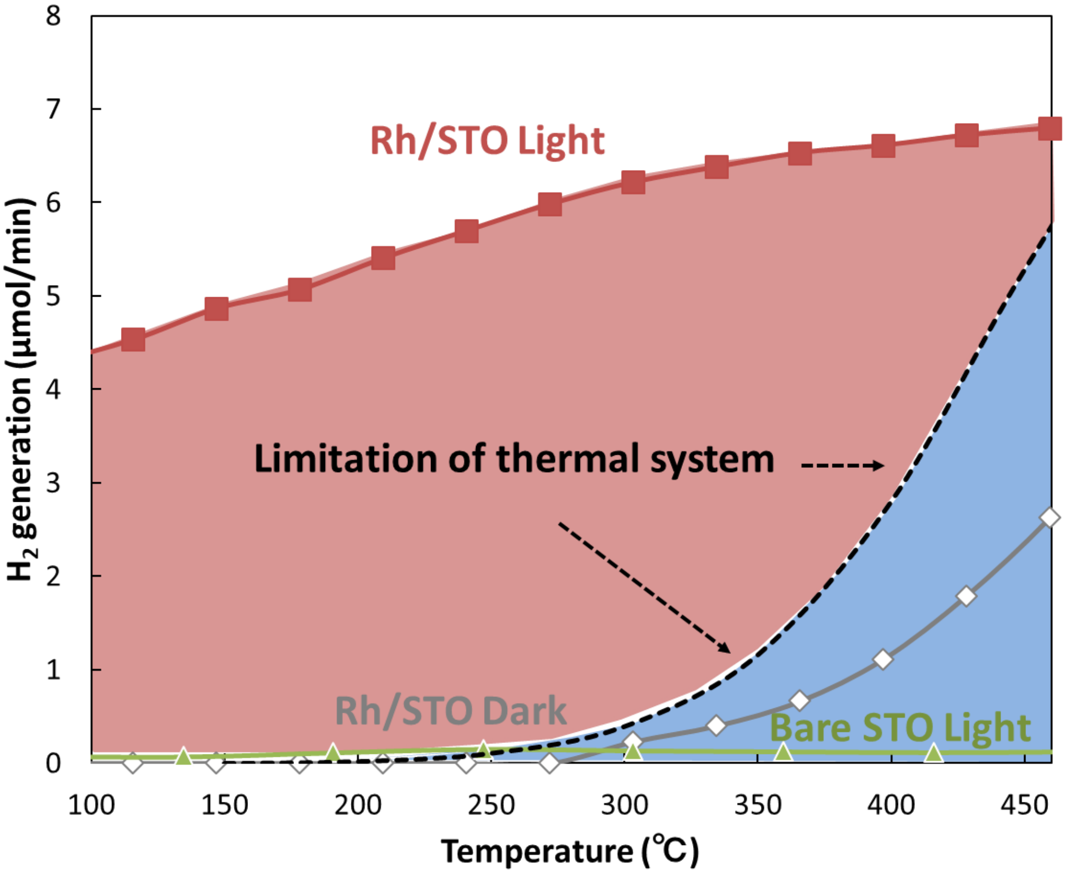

Figure 3.5 Temperature dependence of DRM activity in dark and light irradiation conditions. Rh/STO under light irradiation (red squares), limitation of thermal system by using generic catalystof DRM (dashed line), Rh/STO under dark (gray line with white diamonds), bare STO under light irradiation (green line, with green triangles).

3.3.3 Comparison of different semiconductors

We compared the performance of the Rh/STO catalyst with those of the control samples under light irradiation without external heat. Figure 3.6 shows the CO_2 and CH_4 conversion (panel (a)) and H_2 and CO production (panel (b)). Bare

STO exhibited negligible conversion of CH_4 and CO_2. In contrast to bare STO, Rh/STO exhibited the highest conversion and achieved a stoichiometric yield of over 50 % for both products. We previously investigated the photo-assisted DRM reaction by a pristine STO under light irradiation, as well as with heating at 700 °C, [63] but its conversion was very low and the production yields of H_2 and CO were not balanced[1, 2]. These results indicate that the Rh particles and/or interfaces between Rh and STO play an important role to activate CH_4 and CO_2 effectively. It is also noted that the estimated quantum efficiency (QE) versus absorbed photon number achieved 5.9 % with our Rh/STO catalyst, suggesting that the photon energy would efficiently be used for the production of syngas. In contrast, the conventional Ni/Al_2O_3 catalyst showed no activity (Fig. 3.6), strongly implying that a light-absorbable semiconductor like STO is indispensable to drive DRM at very low temperatures [63]. In this study, we employed $SrTiO_3$ (STO, Bandgap (BG): 3.2 eV), TiO_2 (BG: 3.0 eV), SnO_2 (BG: 3.5 eV), Bi_2WO_6 (BG: 2.8 eV), ZrO_2 (BG: 5.8 eV) and WO_3 (BG: 2.6 eV) as light-absorbable semiconductors. Among these, only $Rh/SrTiO_3$, Rh/ZrO_2 and Rh/TiO_2 exhibited finite DRM activity in light irradiation, while the others were inactive. It is worth of noting that the conduction band position of STO, ZrO_2 and TiO_2 are higher than those of the other semiconductors.[97] It is acknowledged that photocatalytic CO_2 reduction occurs over the catalyst surface in water only in the event the conduction band position of light-absorbable semiconductors is higher than the reduction potential of CO_2 to allow photoexcited electrons smoothly reaching CO_2 admolecules.[50]

Indeed, Rh/SnO_2 poorly promoted DRM under light irradiation because the CO_2 reduction, which is one of the major reaction pathways comprising DRM, hardly occurs due to its low conduction band position. Narrow-band gap semiconductors such as WO_3 also poorly promoted DRM under light illumination due to its low conduction band position, despite having ability to absorb both visible- and UV light to generate heat through photothermal processes. The activity of Rh/ZrO_2 was lower than that of Rh/STO, since the bandgap of ZrO_2 is too large and its absorbed photon number is limited as compared to the STO case. These results suggest that not only the conduction band position of semiconductors but also absorbed photon number and/or oxygen ion diffusion property are important factors for the photocatalytic DRM, as discussed chapter 4.

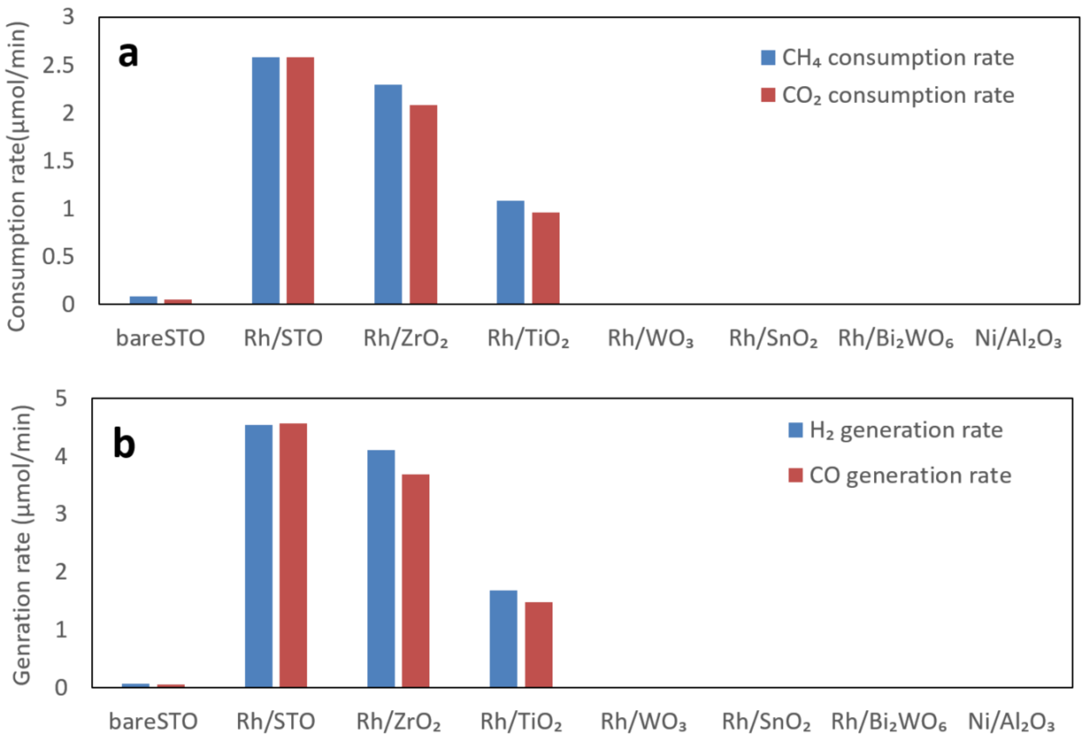

Figure 3.6 Performance of photocatalytic DRM by various catalysts. Conversion of DRM for the Rh/STO (Rh: 10%) and control samples under light irradiation **a** and yield of the products **b**. Sample amount: 5 mg, reactant gas composition: CH_4:CO_2:Ar = 1:1:98 (volume ratio), and gas flow rate: 10 mL min^{-1}, respectively.

3.3.4 Durability of the catalyst

To achieve 50 % yield using the Ni/AlO_3 catalyst, a reaction temperature over 500 °C is needed. However, the catalyst was immediately deactivated by coking at the surface, where fibrous carbon was deposited (Figure 3.7). Supplementary Figure 3.8 shows the durability test of Rh/STO, (panel (a)) and

STEM images for before and after 800 mins of DRM test (panel (b) and (c)). Rh/STO showed a stable reaction over 800 min, and the turnover number (TON), which is defined as the electron number for the production of H_2 or CO molecules divided by the amount of Rh, reached 1827. Furthermore, the turnover frequency (TOF) was calculated to be 1.7 [10^{-2}/s], which is of the same order as those of the previously reported catalysts operating at high temperatures.[78] The particle size of Rh in Rh/STO remained 1- 2 nm in size before and after DRM (Figure. 3.8 (b) and (c)), which means that there was no aggregation of Rh particles. Furthermore, no carbon fiber was detected on Rh/STO after 800 mins DRM operation time, according to the STEM images (Figure 3.8). These results suggest that photocatalytic DRM, without external heat, could suppress the aggregation of catalyst and coking to maintain a stable reaction.

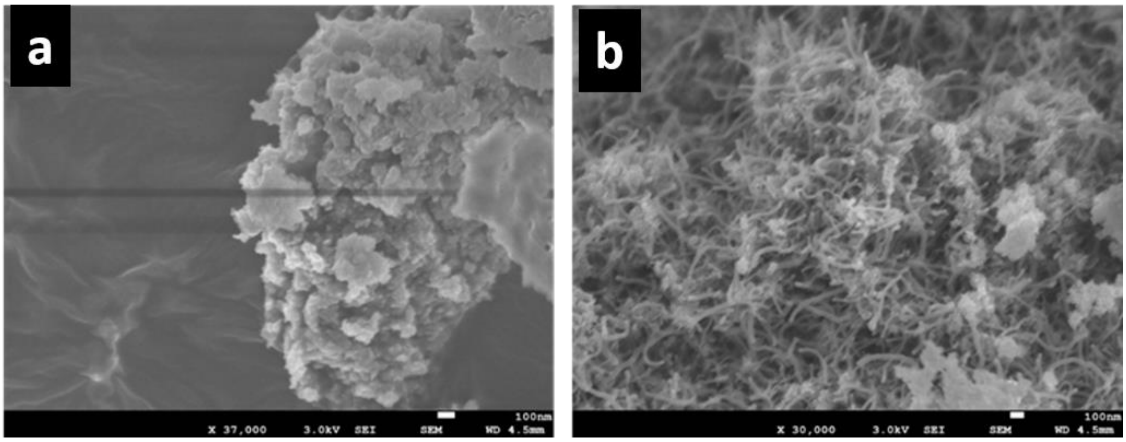

Figure 3.7 SEM images of Ni/Al_2O_3 before (a) and after DRM (b) at 500 ° C for 5 hours.

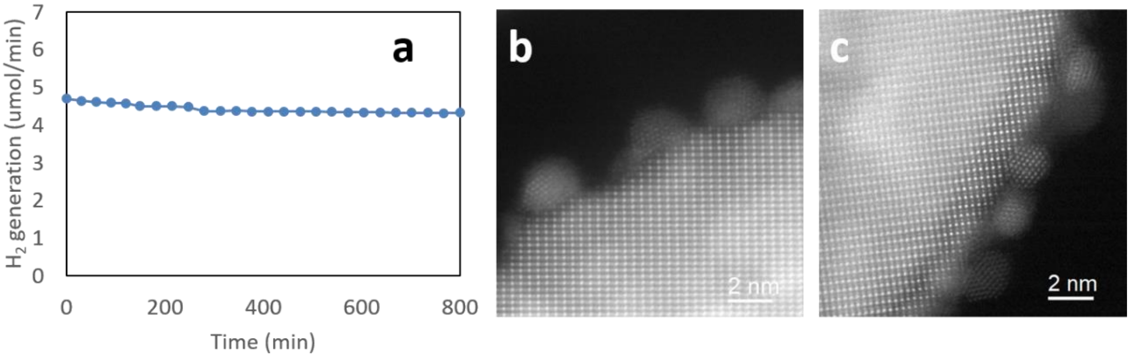

Figure 3.8 Long-term stability for the H_2 production over the Rh/STO (a). HAADF-STEM images of Rh/STO before DRM (b) and 10 hours after DRM (c).

3.4 Conclusion

In the present study, we establish a method to convert CO_2 and CH_4 molecules into syngas through photocatalysis without heat input, outlining a strategy to perform gas-phase photocatalytic uphill reactions using abundant natural gas as an electron donor. Rh/STO drove DRM with a substantially high performance and caused a stoichiometric reaction using photons, while breaking the limitation of thermal catalyst for syngas production. Our facile hydrothermal fabrication method led to high performance and long-term stability without coking and aggregation of metal nanoparticles thus, overcoming one of the problems generally encountered during thermal catalysts.

4. Mechanistic analysis on photocatalytic dry reforming of methane

This chapter explains the mechanism of photocatalytic DRM on Rh/STO. The photo-excited holes and electrons are used for CH_4 oxidation over STO and CO_2 reduction over Rh, respectively. Isotope analysis clarified that the lattice oxygen (O^{2-}) act as mediator to drive DRM. The materials design of Rh/STO can be extended in principle to diverse uphill reactions that utilize solar energy to obtain valued products from different carbon resources.

4.1 Introduction

Electron spin resonance (ESR), Kelvin probe force microscopy (KPFM) analysis, and isotope trace analysis, were used to elucidate charge transport and the mechanism of our photocatalyst. Most of conventional photocatalytic uphill reactions involve protons as mediator, such as water splitting and CO_2 reduction in water. However, in this article, the oxygen ions of O^{2-} act as the intermediate of the photocatalytic DRM.

4.2 Experimental

4.2.1Characterization

The photoexcited species were observed by electron spin resonance (ESR: EMX nano, BRUKER) under N_2, CO_2, CO_2 and CH_4 atmosphere. In the ESR experiment, we introduced catalyst powder into a quartz tube without taking out the powder sample throughout whole ESR measurements including dark and light irradiation conditions. Before various gas flow for in-situ analysis, a quartz tube was vacuumed and treated with nitrogen flow for 30 min to exclude the surface-adsorbed molecules. Under this fixed experimental setting, we could reduce the peak changes caused by the sample tube difference and/or the position to irradiate light.

The surface potential was observed through Kelvin probe force microscope (KPFM), in which the scanning apparatus was based on an atomic force microscope (TT-2, AFM Workshop) equipped with the SPT-20 (Toyo Corporation) surface potential measurement unit. The sample was mounted on an apparatus stage, and scanning was performed using a Pt-coated cantilever (240AC-PP, Mikromasch). The UV light source (ULEDN-102UV-LED, wavelength:365 nm) was focused using a convex lens and illuminated the sample at an incident angle of ~60° . The irradiance was ~56 mW/cm^2 at the sample position.

4.3 Mechanism of the system

4.3.1 Contribution of heat to the system

Next, we discuss the effect of thermal energy on our photocatalysis system, since the surface temperature of our catalyst would be increased by light irradiation. Surface temperature which means working temperature was continuously observed by radiation thermometer (JAPAN SENSOR CORPORATION, TMHX-CQE0500), and we confirmed the increasing of temperature by only irradiating lights was 300 °C which is quite low to drive DRM efficiently as thermal catalysts. However, to exclude the thermal energy effect we carefully discussed as below, charge transfer process at liquid nitrogen temperature and light intensity dependence for DRM activity.

4.3.2 Charge transfer process

To investigate the charge transport in our catalyst during the DRM reaction, we conducted *in-situ* ESR measurement under DRM conditions with light irradiation at -173 °C using liquid nitrogen (Fig. 4.1). Before the test under DRM conditions, we measured the ESR spectra under an inert nitrogen atmosphere for the Rh/STO and bare STO samples to investigate the charge transport between metal Rh nanoparticles and semiconductive STO (panel (a) and (b) in Fig. 4.1). The peaks, which appeared under dark condition in both case of bare STO and Rh/STO, were similar to the previously reported Ti tetravalent oxides cases[98] .These signals are considered as paramagnetic spices related to some defects or impurities. After light irradiation to bare STO and Rh/STO samples, these signals disappeared suggesting that these paramagnetic species would be coupled with photogenerated electrons yielding diamagnetic states. It is noted that the additional peaks were appeared under light irradiation. Previous studies reported on the nature of excited charges in STO or TiO_2 by using ESR, and assigned the ESR signals positioned at around $g = 1.97\text{-}1.99$ and 2.01 to trapped electrons (Ti^{3+} species) and trapped holes (O^-).[98-100] Similar to these reports, trapped hole peaks in the valence band of STO were clearly observed in both Rh/STO and bare STO under UV irradiation, whereas the trapped electron signals in the conduction band of STO were not detected in the case of Rh/STO. These results suggest that the excited electrons in the conduction band of STO are injected into Rh particles.Our Rh nanoparticle would act as an electron acceptor in the DRM reaction, as Maeda *et al.* previously reported [101]. Next, we introduced sole CO_2 gas, or CH_4/CO_2 mixture gas into the ESR chamber (Fig. 4.1(c)). As a result, the intensity of hole signals in an inert N_2 gas atmosphere was similar to that under a CO_2 atmosphere; however, those under sole CH_4 gas and CH_4/CO_2 mixture clearly decreased. These results clearly suggest that the holes reacted with CH_4 but did not react with CO_2.

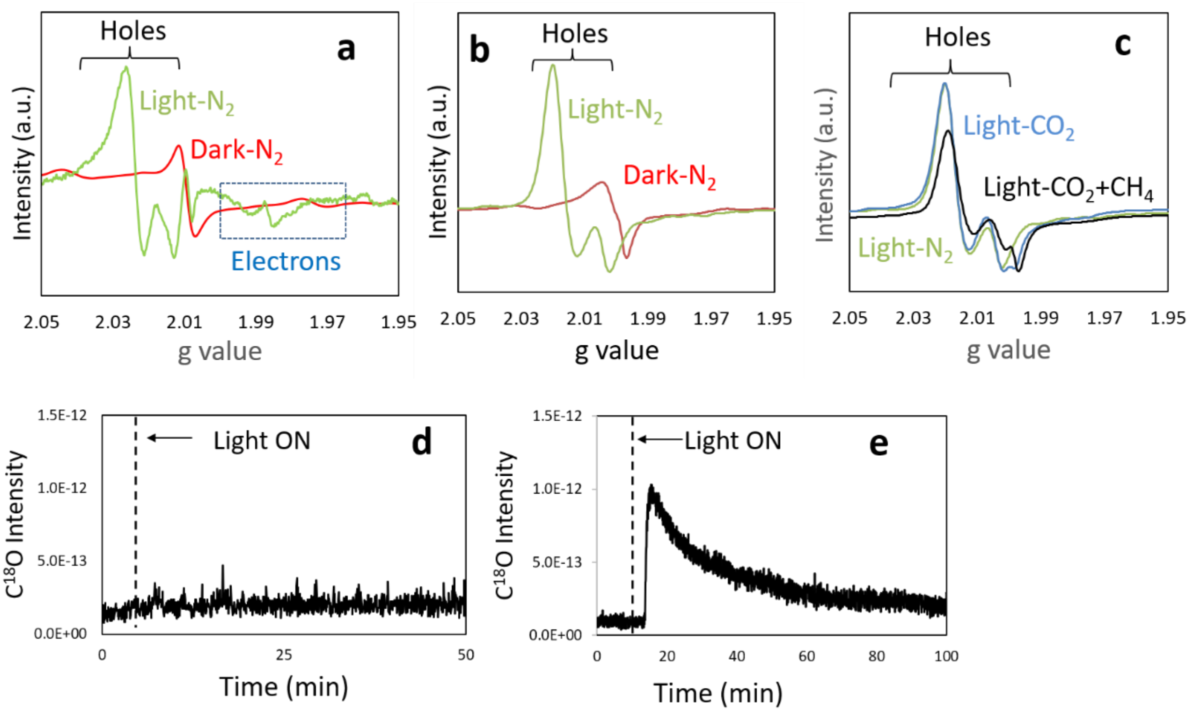

Figure. 4.1 Mechanism analysis by ESR and isotope trace experiment. Electron spin resonance spectroscopy of Rh/STO and bare STO (a-c) and C^{18}O production during DRM analyzed by gas chromatograph mass spectroscopy (GC-MS; d, e). (a) Bare STO under light irradiation and dark conditions in N_2 atmosphere. (b) Rh/STO under light irradiation and dark conditions in N_2 atmosphere. (c) Rh/STO under light irradiation in N_2, CO_2, or CH_4/CO_2 atmosphere conditions. (d) Change of the GC-MS signals for mass number of 30 (C^{18}O) during DRM of Rh/STO without ^{18}O-doping, and (e) that of Rh/STO with ^{18}O-doping.

Next, to directly observe the charge-transfer process, we conducted Kelvin probe force microscopy (KPFM) analysis on the Rh-loaded STO single crystal (110), which was prepared in the same manner as the powder preparation of Rh/STO. We could see the potential gap between STO and Rh even under dark condition, owing to their different work functions (Figure 4.2). According to the subtract potential profile between light-on and light-off conditions (Figure. 4.2 c), the Fermi level upshift of STO by light irradiation was more obvious than that of Rh particle, since the electron transition through band gap excitation occurred in STO. Consequently, the electrons in STO can transfer to Rh following their gap of Fermi levels, and the Fermi level upshift of Rh under light irradiation was also seen (Figure 4.2 a and 4.2 b). These results strongly imply the electron transport between semiconductor and metal interface similar to the previous study.[102]

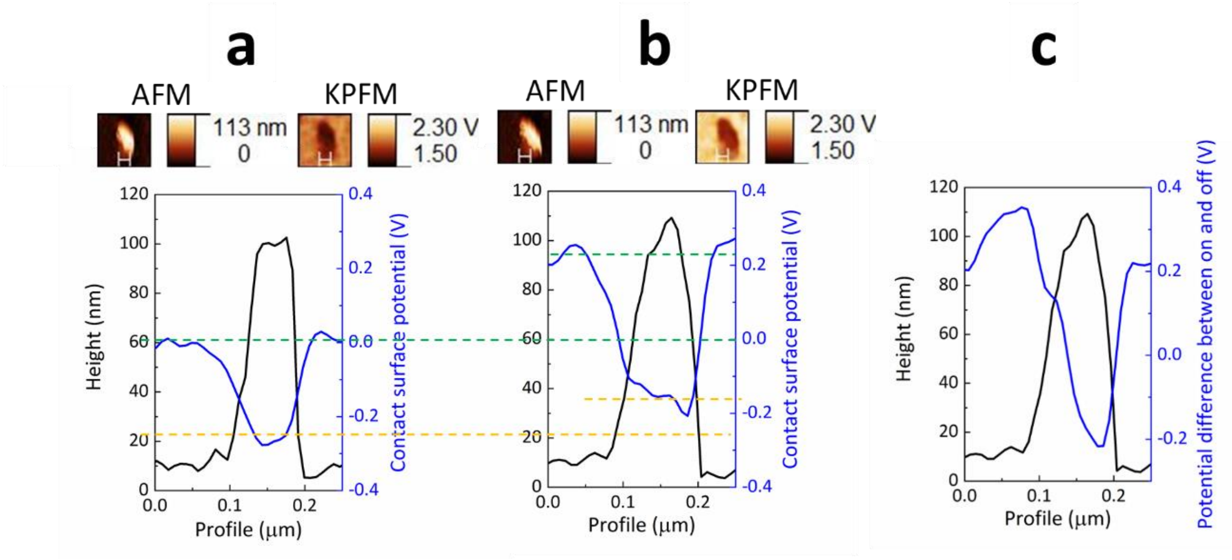

Figure 4.2. Kelvin probe force microscope (KPFM) analysis on the Rh loaded STO single crystal (110), (a) before UV light irradiation, (b) during UV light irradiation, and (c) potential difference between light-on and light-off conditions, respectively. The cross sectional profiles of the atomic force microscope (AFM) and the KPFM analyses were taken in horizontal direction. The sample was prepared by the same manner with powder preparation of Rh/STO.

The scale bars on the AFM images show 60 nm. The contact surface potential of the STO before UV light irradiation is set to 0 V.

According to the subtract potential profile between light-on and light-off condition (panel c), the Fermi level upshift of STO by light irradiation was more obvious than that of Rh particle, since the electron transition through band gap excitation was happened in STO. Consequently, the electrons in STO can transfer to Rh following their gap of Fermi levels. Indeed, the Fermi level upshift of Rh particle was also seen (dashed yellow lines). These results strongly imply the electron transport between semiconductor and metal interface.

4.3.3 Photocatalytic reaction or photothermal reaction

Furthermore, the light intensity dependence on hydrogen production rate over Rh/STO shows a linear relationship, revealing that the reaction is driven by the photoexcited carriers through a photocatalytic light-limited condition, rather than by thermal catalysis behavior (Figure. 4.3). Furthermore, the action spectrum (Figure. 4.4) shows that the reaction was boosted below the wavelength of 380 nm, which corresponds to the band gap energy of STO (3.2 eV). This result also supports the hypothesis that the DRM reaction is mainly driven by the bandgap excitation of STO.

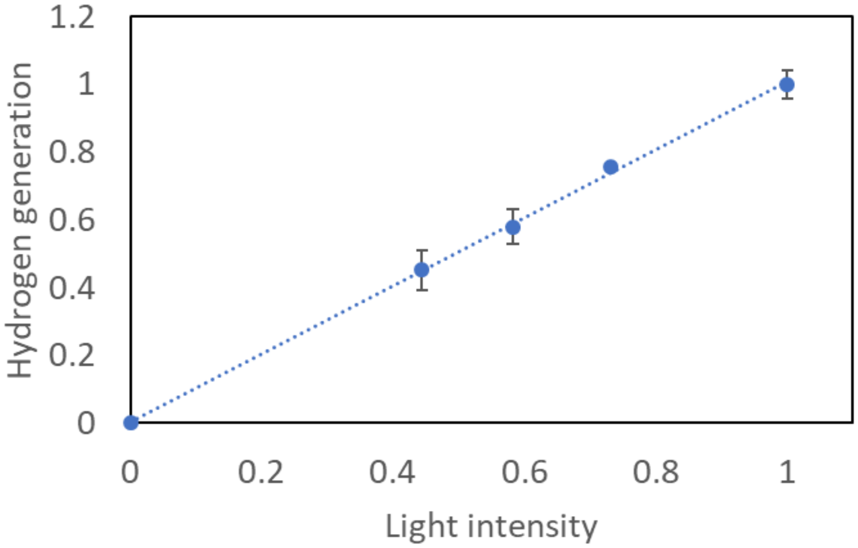

Figure 4.3. Light intensity dependence on hydrogen generation rate of Rh/STO. To simplify the figure, hydrogen generation rate in the vertical axis is normalized. The error bars represent the standard deviation by taking data more than twice.

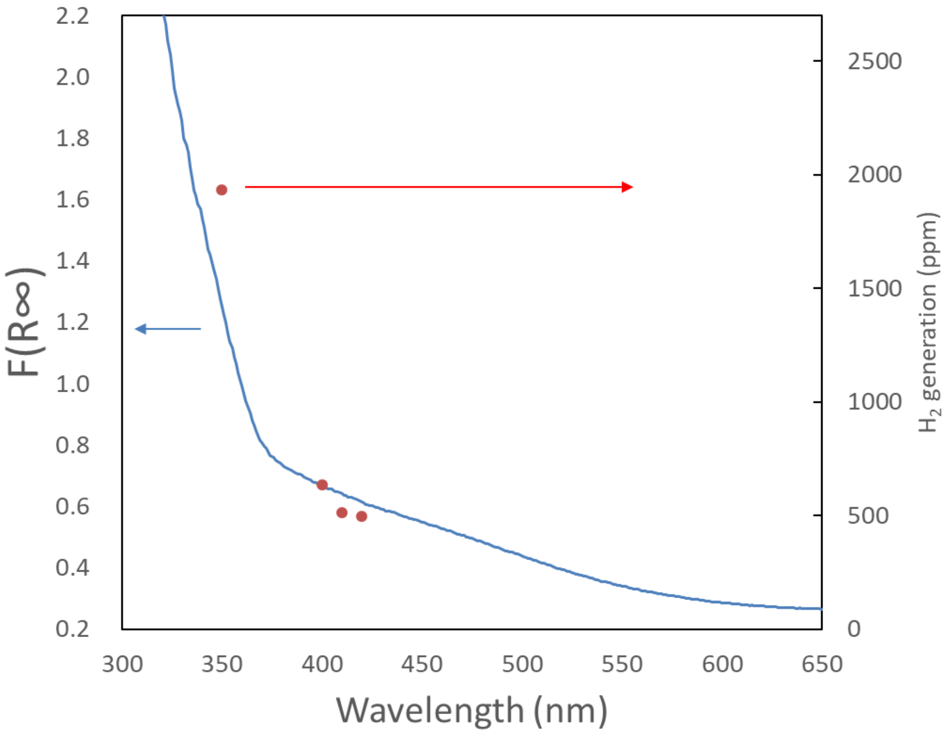

Figure 4.4 UV-vis spectrum of Rh-STO (F: optical absorption drawn by blue line) and action

spectrum of DRM activity (red circles). The action spectrum shows that the reaction was boosted below the wavelength of 380 nm, which corresponds to the band gap energy of STO (3.2 eV).

4.3.4 Investigation of mass transport process

Next, we examined the catalytic activity under sole gas conditions to investigate the mass transport process of oxygen species (Figure. 4.5). When 1 % CH_4 in Ar gas was flowed under light irradiation, both H_2 and CO gasses were generated and the amount of H_2 was larger than CO (Figure. 4.5 (a)), indicating that these products originated from CH_4. Interestingly, CO was produced even under sole CH_4 condition, in which no oxygen species were introduced in the gas phase. However, CO production was gradually decreased under sole CH_4 condition. After the sole CH_4 gas flow, we subsequently introduced CO_2 in addition to CH_4, then both of H_2 and CO were regenerated under light irradiation (Figure. 4.5 (b)). Next, we flowed sole CH_4 gas again (Figure.4.5 (c)), then a similar trend with Figure. 4.5 (a) reappeared. These results strongly imply that the oxygen source of the CO production is feed CO_2 gas in our photocatalytic DRM reaction, in which oxygen species in the catalyst act as the mediator to react with carbon species produced from the partial oxidation of methane.

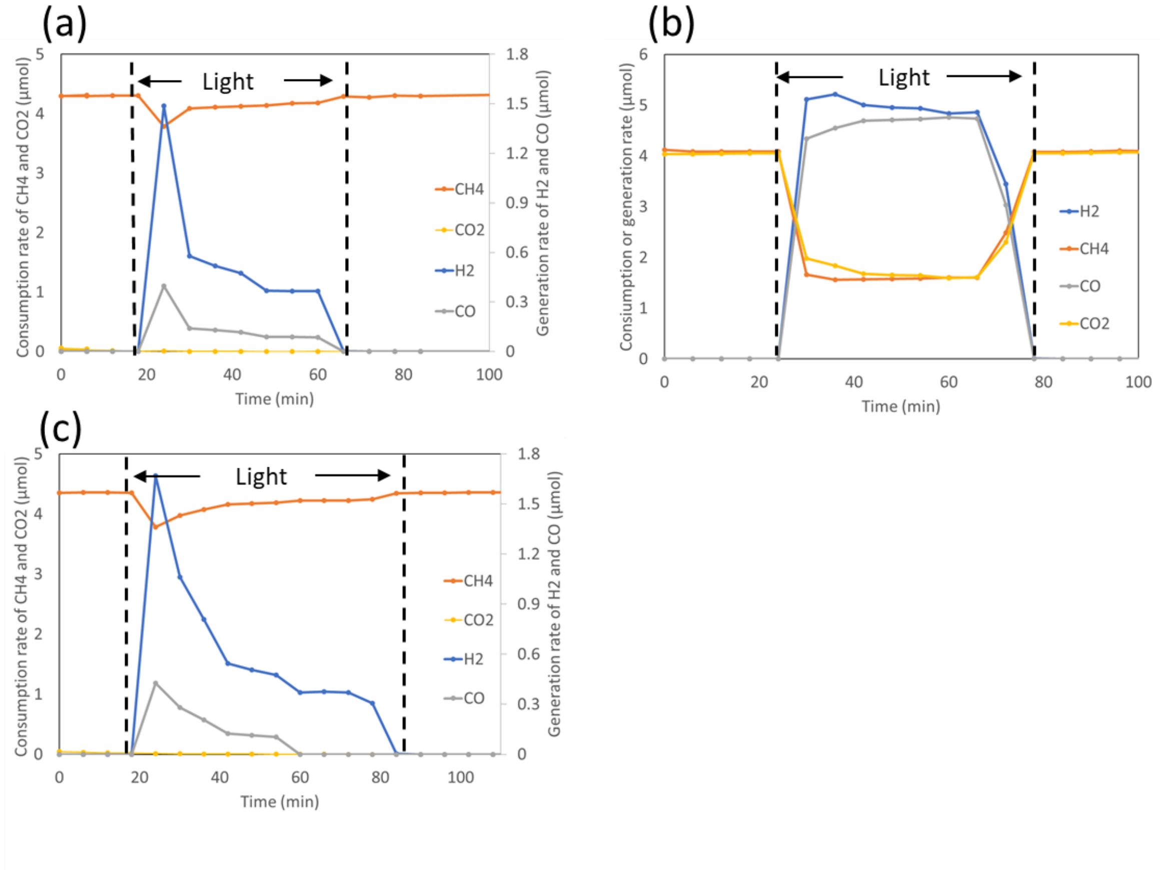

Figure 4.5 Catalytic activity of Rh/STO under sole CH_4 gas condition (a), subsequently introduced by CO_2 and CH_4 mixture (b), and sole CH_4 gas condition again (c). Before the reaction of each condition, the gases were flowed into reactor and the reactor was heated to 150 ° C to remove surface absorbed molecules. The test was subsequently conducted from (a) to (c) in order.

4.3.5 Isotope trace analysis

To discuss the oxygen species more in detail, we conducted isotope trace analysis to detect intermediate species of the reaction. First, we doped ^{18}O into STO lattice near its surface by heat treatment of STO catalyst at 300 °C under the flow of humid Ar gas bubbling through isotope water, in which oxygen mass number was 18 ($H_2{}^{18}O$). According to the previous report [103], this annealing treatment through isotope water bubbling at 300 °C could introduce ^{18}O ions around the surface of the metal oxide catalysis support, other than causing oxidation of metal catalyst. We have evaluated the product during DRM on the ^{18}O-doped STO sample using gas chromatograph mass spectroscopy (GC-MS). Under the light irradiation, carbon monoxide isotope ($C^{18}O$) molecules were produced from the ^{18}O-doped sample as shown in Fig. 4.1(e). We also investigated the control group, *i. e.*, the sample without isotope water bubbling treatment, however, it did not generate any $C^{18}O$ (Fig. 4.1 (d)). These results indicate that the ^{18}O species are successfully introduced into the STO lattice by heat treatment under humid isotope condition, and oxygen species in STO dominantly acts as photocatalytic redox mediator for DRM reaction. Although the quantitative discussion on the amount of doped isotope oxygen species in the STO is difficult, the evidence of $C^{18}O$ generation strongly suggests the oxygen species in STO plays an important role in the present photocatalytic DRM reaction. Our results of stoichiometric syngas generation for long-term light irradiation also indicate that the oxygen mediators would not be released to gas phase as radical species.

4.3.6 Speculated mechanisms

Photo-induced steam reforming and partial oxidation of methane in metal catalysts modified semiconductors have recently been reported.[62, 104] These works explained that the catalysis reaction was driven by hot carriers transition in the metal nanoparticles themselves, in which broad visible light absorption appeared. Indeed, the slight visible light sensitivity observed in our action spectrum is due to this transition. We speculate that the band-gap excitation and hot carrier generation compete in these semiconductor-based systems and depend on the type of methane conversion reactions. In the present case, our ESR analysis, KPFM, and action spectrum strongly suggest that the dominant process for DRM is bandgap excitation of STO. We speculate the mechanism of our photocatalytic DRM as shown in Figure 4.6(a) and (b). Excited electrons in the conduction band of STO were injected into Rh nanoparticles yielding efficient charge separation (Fig.4.6(b)-ii). Electrons in Rh are trapped by CO_2 to produce CO. Further, the remained O^{2-} ions are introduced to STO lattice as proven by isotope trace analysis (Fig.4.6(b)-iii). Photogenerated holes in the valence band of STO migrate near the interface of Rh nanoparticles and react with CH_4. Further, the O^{2-} ions supplied from CO_2 and the holes near the interface between STO and Rh nanoparticles react with methane to produce H_2 (Fig.4.6(b)-iv). Residual carbon after methane cracking would react with oxygen ions generated by CO_2 reduction, yielding stoichiometric products and highly stable anti-coking properties.

Previous research also suggests the oxygen species like O^{2-} in lattice of oxides, play a key role in reactions with carbon species [3, 65]. It is noted that we do not introduce any oxygen source other than CO_2, but we could succeed to produce the same amount of H_2 and CO, strongly suggesting a reaction between residual carbon and oxygen species from CO_2 in our system.

The present study provides a new strategic way to utilize photon energy for methane conversion with a quite high QE of 5.9 %, whereas the electron transition in metal nanoparticles themselves under visible light irradiation slightly contributed to the DRM reaction. However, doping of acceptors, like cationic rhodium ions or anionic nitrogen ions, into the STO crystal to form impurity levels above the valence band [94, 105] will greatly contribute to the visible light absorbability, and now the doped STO is under investigation to extend the active photon in sunlight.

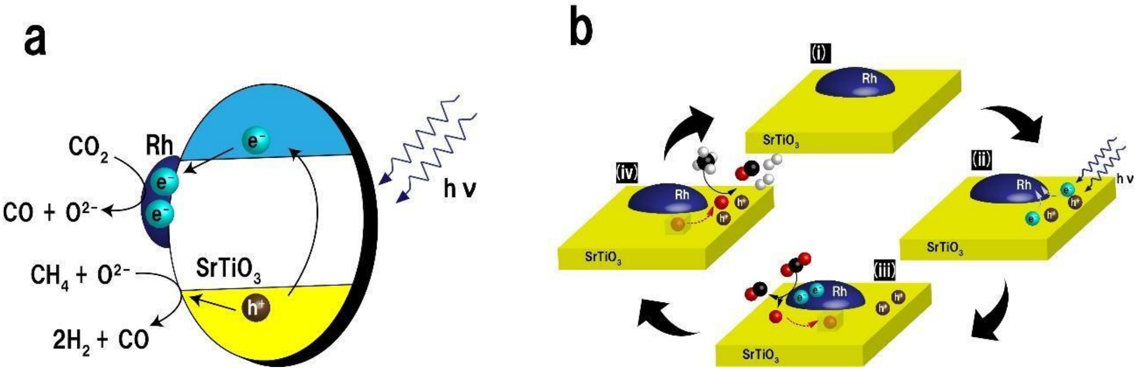

Figure. 4.6 Tentative mechanistic aspects of the photocatalytic DRM by Rh/STO. **a** band diagram and **b** charge transport.

4.4 Conclusion

The present system uses oxygen ions as the mediator, while most of the previously reported photocatalytic uphill reaction used proton mediators in water splitting and CO_2 reduction. In the present study, we chose the DRM as a model reaction among various methane-reforming reactions, since the DRM is the most challenging endothermic reaction, where CO_2 reduction requires the high negative potential of the conduction band to semiconductors. Therefore, the present idea can be extended to other methane-reforming reactions, such as steam reforming and partial oxidation, involving proton reduction and oxygen reduction, important processes for renewable energy applications.

5. Topologically immobilized photocatalysis centre for long-term stable DRM at low temperature

5.1 Strategy for low temperature and long life-time DRM

Before I move on to the main issue, I summarize the points to develop the catalyst for low temperature and long life-time DRM.

1. Topologically immobilized interfaces of catalyst (Chapter 2)
2. Lattice oxygen from oxide supports (Chapter 2, 3 and 4)
3. Appropriate band structure of semiconductors (Chapter 3 and 4)

Since, I chose CeO_2 as a semiconductor which has high lattice oxygen mobility[106] and appropriate band structure for photocatalytic DRM. Further, I chose the synthesis method same as chapter 2 for topologically immobilized interfaces. By combining these knowledge, I realize the low temperature and long-lifetime DRM.

5.2 Introduction

In chapter 3 and 4, I reported the efficient DRM reaction driven by light irradiation on the basis of rhodium and metal oxide hybrid photocatalyst. Its conversion and/or yield of DRM reaction was about 50 %, exceeded beyond the theoretical thermal system’s limit. According to the careful investigation for the mechanism study, photocatalytic DRM involves electron-hole pairs generation in metal oxide, electron injection into rhodium to cause CO_2 reduction, methane clacking by photogenerated holes, and oxygen ions acting as mediators to cause both reduction and oxidation reactions efficiently. Therefore, the morphological control of the oxidation and/or reduction sites interface and that for efficient diffusion of oxygen ions are quite important to achieve the higher photocatalytic DRM activity.

On the other hand, topologically entangled three-dimensional metal/semiconductor nanocomposites, which called rooted catalyst, were reported.[77, 78] In this rooted catalyst, metal phase is separated from metal oxide region and continuously distributed over three dimensional direction. This unique three-dimensional nano-phase separated structure is promising for efficient photocatalyst design, since photocatalytic DRM involves electron-hole pairs separation, these charge transport, as well as oxygen ions diffusion in a metal oxide.

Herein, I have focused on the rooted nanostructure to develop an efficient DRM photocatalyst. Since the photocatalytic DRM reaction involves CO_2 reduction and oxygen ion diffusion in a metal oxide, enough high conduction band as well as oxygen ions conductivity are key characteristics as a metal oxide. Thus, we chose cerium oxide (CeO_2) as a semiconductor photocatalyst because of its oxygen ions diffusion property[106]. and high conduction band to drive CO_2 reduction and deep valence band to drive CH_4 oxidation[107, 108]. We tailored the topologically entangled three-dimensional rhodium/ceria nanocomposites, which represented as Rh#CeO_2. The present chapter reports the photocatalytic DRM property of Rh#CeO_2 and its long-term stability.

5.3 Results and Discussions

5.3.1 Characterization of Rh#CeO_2

The precursor for the synthesis of Rh#CeO_2 was Rh_2Ce bimetal, which was fabricated by melting of metal Rh and Ce ingot using an arc torch. The Rh_2Ce prepared by arc torch treatment was grinded into the size of 30 – 50 μm particles and those were treated under CO and O_2 stream (Ar: CO: O_2 = 97: 2: 1) the flow rate of 50ml/min at 600 ˚C in the tube furnace. As a control sample to our rooted Rh#CeO_2 catalyst, we prepared Rh loaded CeO_2 powder by an impregnation method using commercial CeO_2 powder and rhodiun chloride. The nanostructure of the Rh#CeO_2 was characterized by a scanning transmission electron microscope (STEM) and it showed the rooted structure which composed of entangled network of 5-10 nm sized fibrous Rh and CeO_2 phase (Figure 5.1a – d). The network is spread over three dimensionally and observed whole catalyst powder. The X-ray diffraction (XRD) pattern shows that the single phase of Rh_2Ce bimetal was transformed to multi phases of metallic Rh and CeO_2 by the heat treatment under CO and O_2 stream (Figure 5.2 (a)). Hard X-ray photoemission spectroscopy (HAXPES) revealed that the Rh in Rh#CeO_2 was metallic Rh^0 state. Further, the heat treatment under CO and O_2 stream completely oxidized the metallic cerium into tetravalent Ce^{4+} states, which is consistent with the spectrum of CeO_2 (Figure 5.2 (b) and (c)). Since, it is known that the Ce state during DRM is mixture of 3+ and 4+ because of the atmosphere of H_2 and CO, the real state of Ce during DRM can be speculated as mixture of 3+ and 4+[118,119] .

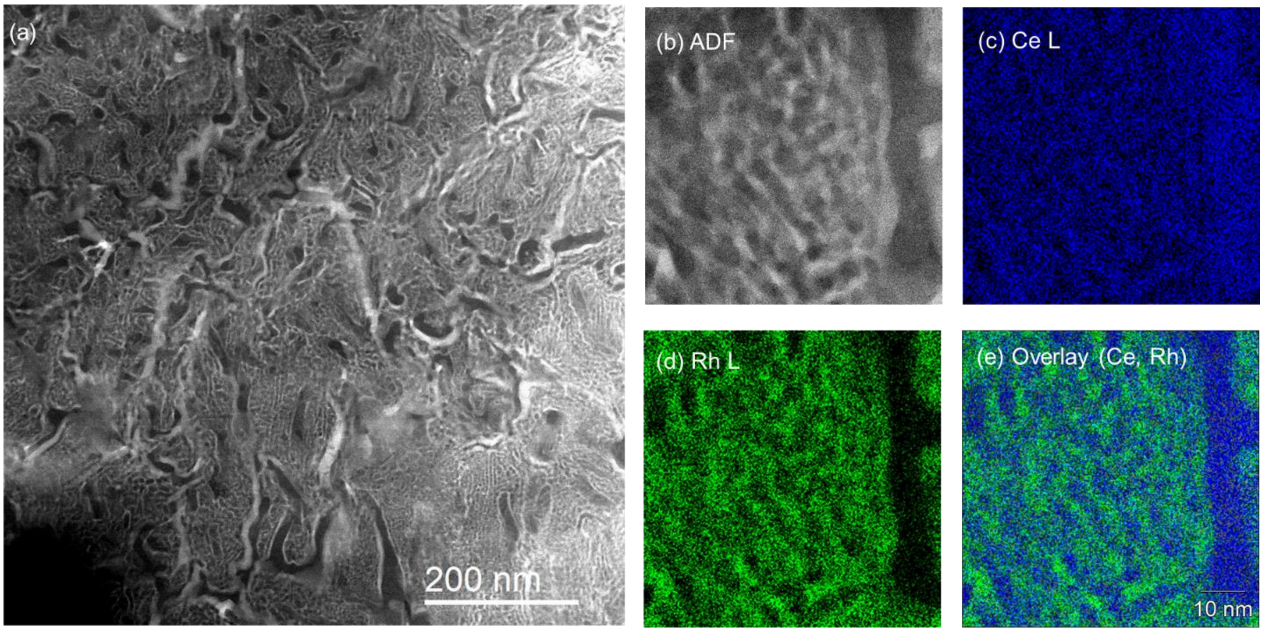

Figure 5.1 Cross sectional STEM image of the Rh#CeO_2 (a), Annular dark-field image of the focused (a) image (c), Energy dispersive X-ray spectroscopy mapping of Ce, Rh and Overlay image (c)-(e) at image (b).

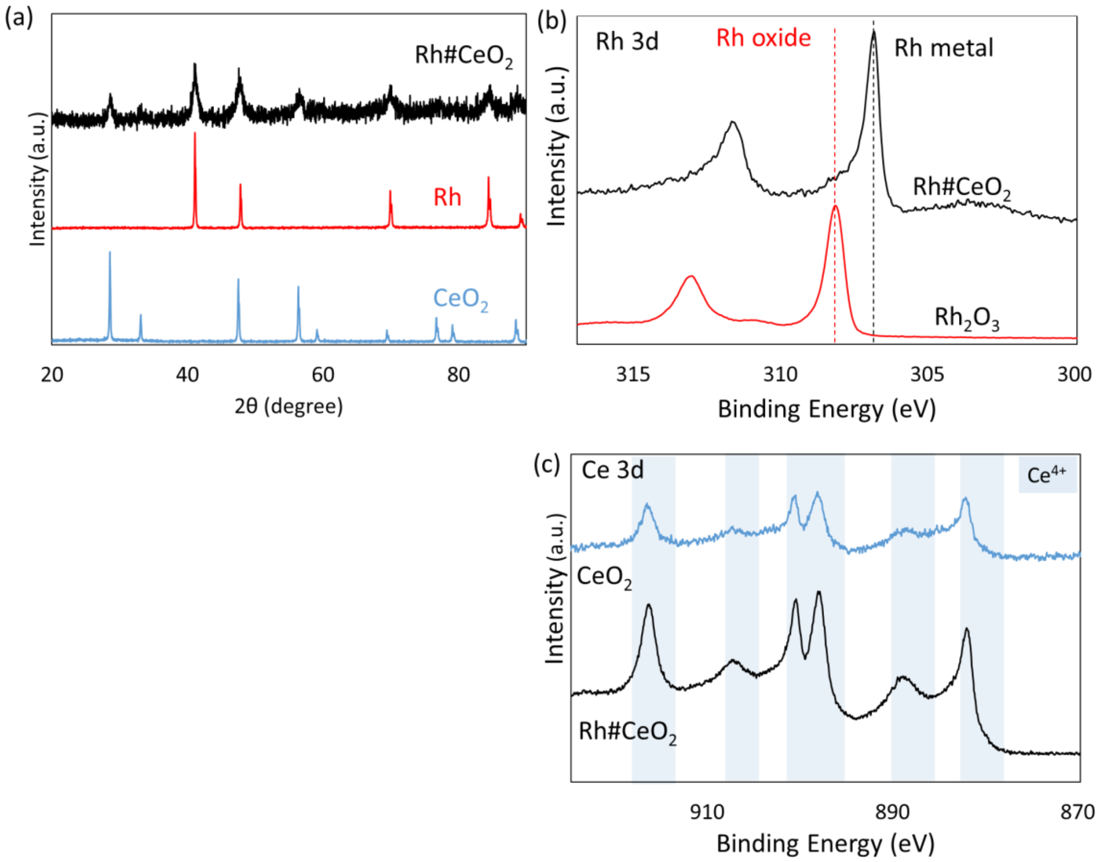

Figure 5.2 XRD pattern for the Rh#CeO$_2$, Rh metal and CeO$_2$ (a). and HAXPES in the Rh 3d region for the Rh$_2$O$_3$ and Rh#CeO$_2$ (b). and Ce 3d region for the CeO$_2$ and Rh#CeO$_2$ (c).

5.3.2 Photocatalytic activity and Stability

The photocatalytic DRM activities of the Rh#CeO$_2$ and control samples were evaluated under light irradiation by a 150 W mercury-xenon lamp under the gas flow (CH$_4$/CO$_2$/Ar = 1/1/98, flow rate: 10 mL/min). Figure 5.3 show conversions under light irradiation. The photocatalytic activity of our rooted Rh#CeO$_2$ was significantly higher than that of Rh/CeO$_2$, which was prepared by a conventional impregnation method. It is noted that the conversion of CH$_4$ and

CO_2 by Rh#CeO_2 reached to around 65 %, which is much higher than the previous report (Chapter 3). It is also noteworthy, that the stoichiometric reaction proceeded, i. e. product amount was twice of the consumption amount of feed gas. Further, the Rh#CeO_2 sustained stable DRM reaction over 100 h, and its turn-over number reached to 13000 (Figure 5.4), indicating that the carbon intermediate precipitation (coking) was suppressed because of the stoichiometric DRM reaction on our photocatalyst. Next, to clarify the mechanisms of DRM reaction under light irradiation, we evaluated the action spectrum (Figure 5.5). The red line shows Bare CeO_2 spectrum and the blue line shows Rh#CeO_2, and the dots shows the activity at the wavelength. The absorption starts from 360 nm which has great match with the band gap absorption of CeO_2. Further, the activity also boosted from the wavelength of the band gap excitation of CeO_2 clearly suggesting that the photogenerated electron-hole pairs contributed to drive the DRM reaction[107, 108].

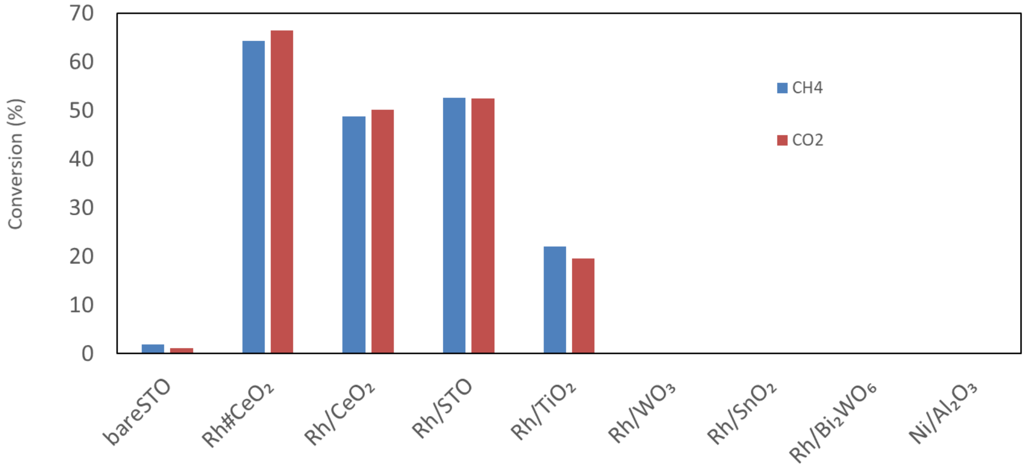

Figure 5.3 DRM performance of Rh#CeO$_2$, 54.5wt%Rh/CeO$_2$ and other conventional photocatalysts under UV irradiation.

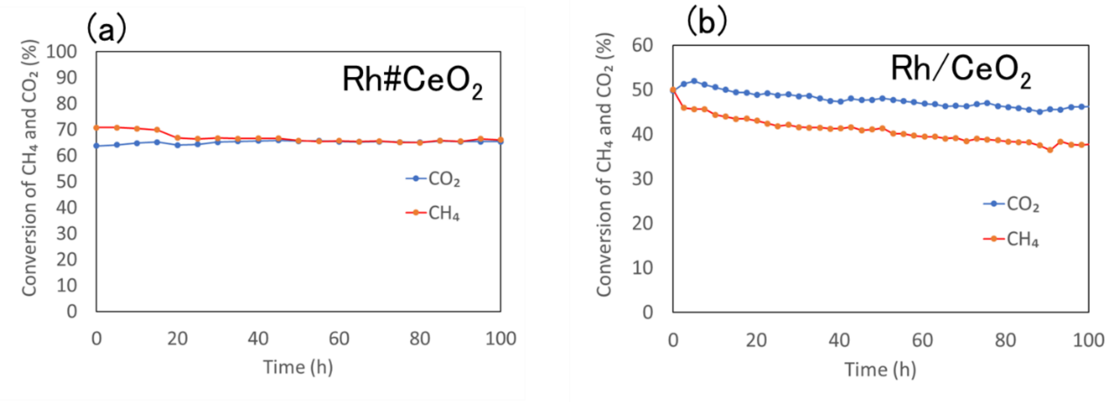

Figure 5.4 Long time stability under UV irradiation. (a)Rh#CeO$_2$ and (b) Rh loaded CeO$_2$

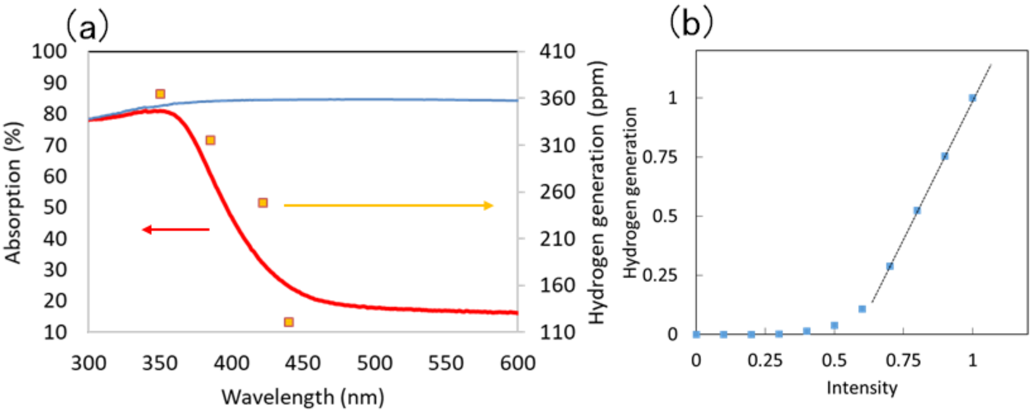

Figure 5.5 (a)UV-vis spectrum of Rh#CeO$_2$ and CeO$_2$ (blue and red line) and action spectrum of photo-DRM activity (orange squares). The action spectrum shows the reaction was boosted at the band gap energy (365nm). Light intensity dependence on hydrogen generation rate of Rh#CeO$_2$ (b). The light intensity and hydrogen generation rate were normalized.

5.3.3 Mechanistic analysis

Here we discuss the comparison between the present light-driven DRM reaction and a thermal catalyst system. To achieve the same conversion (~65 %) of the present light irradiation condition, heat input over 600 ˚C was needed. These results indicate that the high 65 % conversion under light irradiation cannot be simply explained by thermal process. Figure 5 (b) shows the light intensity dependence on catalytic activity and surface temperature for each condition.

It is well known that the electron conductivity which means oxygen species conductivity of Ce oxides has exponential relation between temperature[106]. Recently, our group reported that the photo-DRM was drove using oxygen ion as intermediate. The report supports our results that shows the Rh#CeO_2 shows high activity than other semiconductors and has not linear relationship at low light intensity region which means temperature was not enough to conduct oxygen species for efficient photo-DRM. Further, doping of Zr, Pr, La, Gd or Sm can be good candidates to improve oxygen mobility to drive photo-DRM effectively[120] .

Conventional thermal catalysts for DRM rarely exhibit stoichiometric reaction and immediately deactivated by the coking at the surface because of the sub-reaction[7]. To avoid coking, the previous study applied high temperature to change the balance of prior reaction of coking to target reaction of DRM[109]. However, the high temperature treatment causes the quick deactivation by the aggregation of loaded catalysts on oxides[16]. In the case of Rh#CeO_2, the main driving factors are the photocatalytic generated electrons and holes and the photocatalytic reaction tends to force the products to be balanced which means stoichiometric reaction happens when there is no impurities or unstable catalysts. Further, in the Rh#CeO_2 photo-DRM system, no heat input realized the quite low reaction temperature which causes the suppression of catalyst aggregation. In particular, the Rh and CeO_2 were immobilized at the interfaces because of the entangled nano structure strongly prohibits the aggregation which leads the long life time.

5.4 Conclusion

In conclusion, we demonstrated a catalyst design with -10nm entangled network of metal and oxides, namely, Rh#CeO_2. Rh#CeO_2 converted CH_4 and CO_2 into CO and H_2 gas almost stoichiometry without heat input and achieved quite high activity over 60 % conversion. Further, the reaction stably continued above 100 hours to achieve TON as 13000 with less sub-reaction like coking. The topologically immobilized interface of Rh and CeO_2 inhibited deactivation by the migration of catalyst. Further, the highly entangled interface enabled the lattice oxygen spices diffusion and reaction between oxygen species and carbon species to suppress the coking. In the present study, strongly suggests the catalyst design with usage of oxygen in the oxides realizes the high activity and stability for gas phase photocatalytic reactions.

6. Scientific Contribution of This Thesis

In this chapter, I discuss the philosophical contribution of this thesis to science and practical catalyst applications. Firstly, I will explain how my thesis is novel and gives important insight in light of the history of photocatalysis research. Secondly, I will describe how this thesis has a practical advantage versus previously reported DRM catalyst systems.

6.1 History of photocatalysis and scientific impact of this thesis on photocatalysis field

As I introduced in Chapter 1, the research and development of photocatalysis have been initiated since 1970s. Until now, various photocatalytic functions, such as water splitting, water and/or air purification, self-cleaning, visible light sensitivity for anti-pathogen function, and artificial photosynthesis including CO_2 reduction, have been studied. The report of Honda-Fujishima effect encouraged many researchers to develop the hydrogen energy production by photocatalysis, when people faced “energy crisis”, which was caused by the peaking of oil production in major industrial nations[31]. Unfortunately, the photocatalytic water splitting has not yet been commercialized, because most of the reported photocatalytic efficiencies were insufficient and their poor visible-light sensitivities. After the energy crisis in 1970s, rapid economic growth caused the environmental pollution in 1980s. Prof. Hashimoto et al. focused on the strong oxidation power of TiO_2 photocatalyst and developed environmental purification photocatalyst. In 1990s, Wang et al. found the phenomena of light-induced amphiphilic surfaces,[39] which can control the surface wettability of solid substrates by light irradiation. This hydrophilic conversion opened the new application of photocatalyst for self-cleaning function. Photocatalytic hydrophilic conversion has widely been applied to outdoor building materials, such as roof, wall, and/or glass window. In addition, Prof. Hashimoto' group reported novel interfacial charge transfer process which enables wide gap photocatalyst to absorb visible light in 2000s [43, 98, 110, 111]. This technology enabled the usage of photocatalyst not only for outdoor use but also for indoor environment such as airport and hospital. Indeed, since the report of the Honda-Fujishima effect, photocatalysts could successfully contribute to practical applications especially for environment remediation. Recent years, we must change the energy source from fossil oil to sustainable energy such like wind, water and light according to the Kyoto Protocol and the Paris Agreement. Thus, the research on water splitting and CO_2 reduction returned to the hot topic[46, 51, 54, 55, 57, 88, 89, 94, 101].

Although the development of photocatalytic energy production is desired, we will still depend on fossil fuel and have to efficiently use and manage these fossil fuel for long term ahead. Most recently, the development of mining technology of gas product like natural gas and landfill gas increased the importance of methane conversion as described in chapter 1[7, 12, 65, 112-114]. The world is changing the direction of energy demand from fossil oil to methane[2].

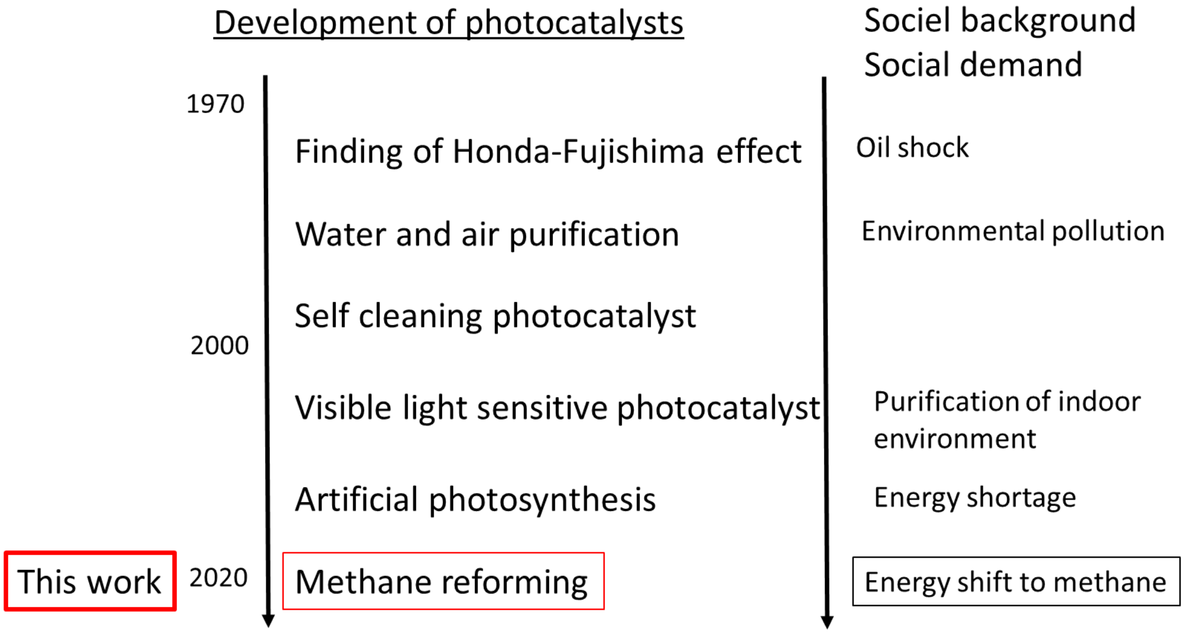

Figure 6.1 Relation between development of photocatalysts and social demand.

As described in chapter 3-5, the photocatalytic DRM system has successfully been developed by my thesis. It is noted that I use oxygen ions mediator to drive the DRM reaction, which is much different from previously reported photocatalysis. In the case of water splitting and CO_2 reduction, protons in water act as mediator to drive up-hill reaction. In the case of environmental purification application under gaseous atmosphere, photocatalysts also produce O^{2-}, hydrogen peroxide, and/or OH^- radical species[115-117]. However, such oxygen radical spices are dissipated to atmosphere and they do not act as mediator for any redox reactions. In contrast to these previously reported systems, my photocatalytic system uses oxygen ions mediator to drive efficient redox reaction (Fig. 6.2). In other words, the produced O^{2-} ions through CO_2 reduction react with CH4 through lattice oxygen ions mediator. My finding of using oxygen ions mediator is quite new in the field of photocatalytic science, and this idea is not limited to the DRM reaction but is applicable for various gas phase reactions such as SRM and ammonia synthesis. Though I used Rh/STO and Rh#CeO_2, my idea can be extended to other photocatalyst materials like oxynitride semiconductors with visible light sensitivity. I expect that my thesis encourages many scientists to start various photocatalytic gas-phase uphill reactions in addition to the DRM reaction. The reaction scheme of my thesis is quite different from conventional water-splitting, CO_2 reduction, or air purification, thus new patents will be created based on my thesis concept.

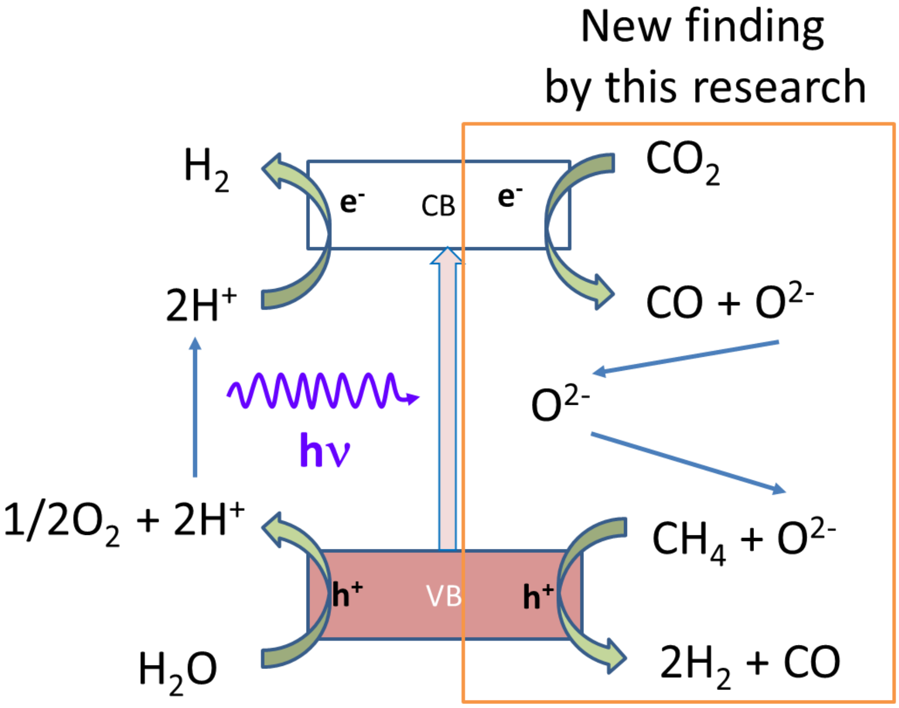

Figure 6.2 New finding by this thesis research to photocatalytic and science fields.

6.2 Industrial and practical impact of this thesis on the methane reforming applications

Here, I discuss the advantage of my photocatalyst system as compared to conventional thermal catalysts and photo-assisted systems. In Figure 6.3, the relation between reforming temperature and coking rate were described for various catalysts. Most of supported catalysts shows the high coking rate with decreasing the temperature. On the other hand, Ni#Y_2O_3 catalyst positioned the left-bottom corner which shows the lowest coking rate and reaction temperature.

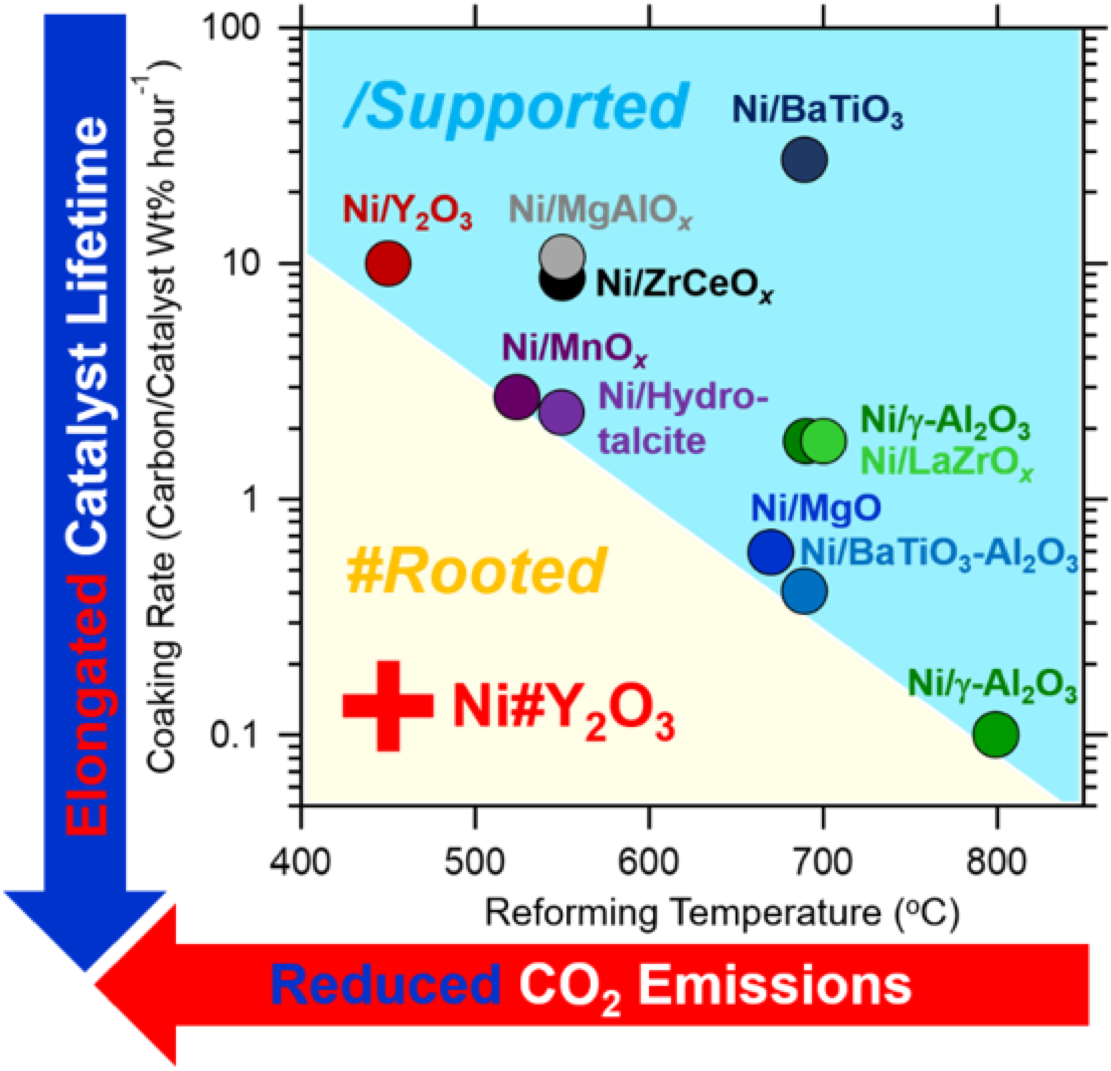

Figure 6.3 Relation between reforming temperature and coking rate.

Next, Table 6.1 shows the comparison of my photocatalysts (Rh/STO and Rh#CeO$_2$) with previously reported photo-assisted systems to drive DRM reaction. As shown in Table 6.1, previous studies of photo-induced DRM are quite limited. Methane conversion and/or production yield of these previous studies were less than 5 %. Some of these studies indicate that the DRM reaction was driven by hot-carrier generation or bandgap excitation, however, they did not show any clear evidence on the role of electron-hole pairs. The present study has elucidated the reaction mechanism using careful in-situ ESR and isotope trace analyses, and the DRM activity of our catalyst is much higher than those of previous reports. Our catalysis achieves state-of-art DRM performance with a yield of over 50 % under extra-mild conditions (without heating/only light irradiation). Surprisingly. the yield of my nano-phase separated photocatalyst (Rh#CeO_2) reached 65 % yield for the DRM reaction, which is the world record at a present among the previously reported photo-assisted DRM catalysts.

Table 6.1 Comparison with previous reported catalysts and this work.

	Catalyst	Reaction	yield or conversion	mechanism
Yoshida et al. [60]	β-Ga_2O_3	Non-oxidative methane coupling DRM	less than 1 % (@200 ℃)	no evidence
Ye et al. [62]	Rh/TiO_2	Steam-reforming of methane	2.6 % (@260 ℃)	Hot carrier from metal
Han et al.[61]	$Pt/Black TiO_2$	DRM	1.47 % (@550 ℃)	Not included
Singgih et al.[63]	$SrTiO_3$	DRM	3.88 % (@700 ℃)	Not included
This work Chapter 3.4	$Rh/SrTiO_3$	DRM	52 % (without heat)	Lattice oxygen intermediate Photocatalytic reaction
This work Chapter 5	Rh#CeO_2	DRM	65 % (without heat)	Lattice oxygen intermediate Photocatalytic reaction

7. Summary of This Thesis

Chapter 1 is the general introduction of this thesis. Low temperature and stable DRM is significant challenge but one of the best ways to utilize abundant natural gas or greenhouse gases. In chapter 1, I showed the strategy to realize loe temperature and stable DRM from the viewpoint of nano-structure, usage of lattice oxygen and introduce of photon energy. Thus, I decided the objectives as to drive stable DRM at low temperature.

In Chapter 2, I developed the catalyst in this thesis by controlling the catalyst composition and nanostructure. I carefully investigated the mechanism of carbon growth by the in-situ TEM observation. Based on these discussions, I developed the efficient thermal catalyst by a topological control which actively drive DRM under low temperature (450℃).

In Chapter 3 and 4, Even though previous studies reported photo-assisted DRM, no research, which realized the photocatalytic DRM by using light without heat, has yet been established. Further, previous works could not elucidate the photocataltic DRM process. Therefore, I developed a photocatalytic system from the viewpoint of band structure of semiconductors and co-catalyst modification to drive DRM by using light as an energy source. The photocatalyst Rh/STO showed 52 % of conversion and long-time stability under UV light irradiation. Finally, I clarified the mechanism of photocatalytic DRM by ESR and Isotope trace analysis and the importance of lattice oxygen to drive stable DRM.

In Chapter 5, I combined the knowledge of Chapter 2-4 to establish efficient photocatalytic DRM system. CeO_2 was chosen as semiconductor because of the high mobility of lattice oxygen and appropriate band structure. Further, the structure was controlled to be nano-phase separated structure with metal Rh. The catalyst showed highest activity of 65 % conversion and stably proceeded photocatalytic DRM over 100 hours.

In Chapter 6, I explained the philosophical contribution of my thesis by introducing history of photocatalysis again. The findings of lattice oxygen mediated photocatalytic system was firstly revealed. My finding of using oxygen ions mediator is quite new in the field of photocatalytic science, and this idea is not limited to the DRM reaction but is applicable for various gas phase reactions such as SRM and ammonia synthesis. Though I used Rh/STO and Rh#CeO_2, my idea can be extended to other photocatalyst materials like oxynitride semiconductors with visible light sensitivity. I expect that my thesis encourages many scientists to start various photocatalytic gas-phase uphill reactions in addition to the DRM reaction. The reaction scheme of my thesis is quite different from conventional water-splitting, CO_2 reduction, or air purification, thus new patents will be created based on my thesis concept.

Chapter 7 summarized this thesis.

References

1. BP p.l.c, L., 2019, BP Energy Outlook 2019. 2019.
2. Administration, E. I. ANNUAL ENERGY OUTLOOK 2016. https://www.eia.gov/outlooks/aeo/pdf/0383(2016).pdf.
3. Enger, B. C.; Lødeng, R.; Holmen, A., A review of catalytic partial oxidation of methane to synthesis gas with emphasis on reaction mechanisms over transition metal catalysts. *Applied Catalysis A: General* **2008,** *346* (1-2), 1-27.
4. Che, F.; Gray, J. T.; Ha, S.; McEwen, J.-S., Improving Ni Catalysts Using Electric Fields: A DFT and Experimental Study of the Methane Steam Reforming Reaction. *ACS Catalysis* **2017,** *7* (1), 551-562.
5. Che, F.; Ha, S.; McEwen, J.-S., Elucidating the field influence on the energetics of the methane steam reforming reaction: A density functional theory study. *Applied Catalysis B: Environmental* **2016,** *195*, 77-89.
6. Kechagiopoulos, P. N.; Angeli, S. D.; Lemonidou, A. A., Low temperature steam reforming of methane: A combined isotopic and microkinetic study. *Applied Catalysis B: Environmental* **2017,** *205*, 238-253.

7. Pakhare, D.; Spivey, J., A review of dry (CO2) reforming of methane over noble metal catalysts. *Chemical Society Reviews* **2014,** *43* (22), 7813-7837.

8. Gronchi, P.; Centola, P.; Del Rosso, R., Dry reforming of CH4 with Ni and Rh metal catalysts supported on SiO2 and La2O3. *Applied Catalysis A: General* **1997,** *152* (1), 83-92.

9. Fan, M. S.; Abdullah, A. Z.; Bhatia, S., Catalytic technology for carbon dioxide reforming of methane to synthesis gas. *ChemCatChem* **2009,** *1* (2), 192-208.

10. Galuszka, J.; Pandey, R.; Ahmed, S., Methane conversion to syngas in a palladium membrane reactor. *Catalysis Today* **1998,** *46* (2-3), 83-89.

11. Lewis, W. K.; Gilliland, E. R.; Reed, W. A., Reaction of Methane with Copper Oxide in a Fluidized Bed. *Industrial & Engineering Chemistry* **1949,** *41* (6), 1227-1237.

12. Sodesawa, T.; Dobashi, A.; Nozaki, F., Catalytic reaction of methane with carbon dioxide. *Reaction Kinetics and Catalysis Letters* **1979,** *12* (1), 107-111.

13. Alipour, Z.; Rezaei, M.; Meshkani, F., Effect of alkaline earth promoters (MgO, CaO, and BaO) on the activity and coke formation of Ni catalysts supported on nanocrystalline Al2O3 in dry reforming of methane. *Journal of Industrial and Engineering Chemistry* **2014,** *20* (5), 2858-2863.

14. Kathiraser, Y.; Thitsartarn, W.; Sutthiumporn, K.; Kawi, S., Inverse NiAl2O4 on LaAlO3–Al2O3: unique catalytic structure for stable CO2 reforming of methane. *The Journal of Physical Chemistry C* **2013,** *117* (16), 8120-8130.

15. Bradford, M. C.; Vannice, M. A., CO2reforming of CH4over supported Ru catalysts. *Journal of Catalysis* **1999,** *183* (1), 69-75.

16. Hou, Z.; Chen, P.; Fang, H.; Zheng, X.; Yashima, T., Production of synthesis gas via methane reforming with CO2 on noble metals and small amount of noble-(Rh-) promoted Ni catalysts. *International Journal of Hydrogen Energy* **2006,** *31* (5), 555-561.

17. Mark, M. F.; Maier, W. F., CO2-reforming of methane on supported Rh and Ir catalysts. *Journal of Catalysis* **1996,** *164* (1), 122-130.

18. Múnera, J. F.; Irusta, S.; Cornaglia, L. M.; Lombardo, E. A.; Cesar, D. V.; Schmal, M., Kinetics and reaction pathway of the CO2 reforming of methane on Rh supported on lanthanum-based solid. *Journal of Catalysis* **2007,** *245* (1), 25-34.

19. Djinović, P.; Batista, J.; Pintar, A., Efficient catalytic abatement of greenhouse gases: methane reforming with CO2 using a novel and thermally stable Rh–CeO2 catalyst. *international journal of hydrogen energy* **2012,** *37* (3), 2699-2707.

20. Bitter, J.; Seshan, K.; Lercher, J., Mono and bifunctional pathways of CO2/CH4reforming over Pt and Rh based catalysts. *Journal of catalysis* **1998,** *176* (1), 93-101.

21. Gallego, G. S.; Mondragón, F.; Barrault, J.; Tatibouët, J.-M.; Batiot-Dupeyrat, C., CO2 reforming of CH4 over La–Ni based perovskite precursors. *Applied Catalysis A: General* **2006,** *311*, 164-171.

22. Tsipouriari, V.; Efstathiou, A.; Zhang, Z.; Verykios, X., Reforming of methane with carbon dioxide to synthesis gas over supported Rh catalysts.

Catalysis today **1994,** *21* (2-3), 579-587.

23. Wang, S.; Lu, G.; Millar, G. J., Carbon dioxide reforming of methane to produce synthesis gas over metal-supported catalysts: state of the art. *Energy & fuels* **1996,** *10* (4), 896-904.

24. Gadalla, A. M.; Bower, B., The role of catalyst support on the activity of nickel for reforming methane with CO2. *Chemical Engineering Science* **1988,** *43* (11), 3049-3062.

25. Pakhare, D.; Spivey, J., A review of dry (CO 2) reforming of methane over noble metal catalysts. *Chemical Society Reviews* **2014,** *43* (22), 7813-7837.

26. Beebe Jr, T. P.; Goodman, D. W.; Kay, B. D.; Yates Jr, J. T., Kinetics of the activated dissociative adsorption of methane on the low index planes of nickel single crystal surfaces. *The Journal of chemical physics* **1987,** *87* (4), 2305-2315.

27. Zheng, C.; Apeloig, Y.; Hoffmann, R., Bonding and coupling of C1 fragments on metal surfaces. *Journal of the American Chemical Society* **1988,** *110* (3), 749-774.

28. Bradford, M. C. J.; Vannice, M. A., Catalytic reforming of methane with carbon dioxide over nickel catalysts I. Catalyst characterization and activity. *Applied Catalysis A: General* **1996,** *142* (1), 73-96.

29. Li, K.; Wang, H.; Wei, Y.; Yan, D., Syngas production from methane and air via a redox process using Ce–Fe mixed oxides as oxygen carriers. *Applied Catalysis B: Environmental* **2010,** *97* (3-4), 361-372.

30. Frusteri, F.; Spadaro, L.; Arena, F.; Chuvilin, A., TEM evidence for factors affecting the genesis of carbon species on bare and K-promoted Ni/MgO catalysts during the dry reforming of methane. *Carbon* **2002,** *40* (7), 1063-1070.

31. Fujishima, A.; Honda, K., Electrochemical photolysis of water at a semiconductor electrode. *nature* **1972,** *238* (5358), 37.

32. Frank, S. N.; Bard, A. J., Heterogeneous photocatalytic oxidation of cyanide ion in aqueous solutions at titanium dioxide powder. *Journal of the American Chemical Society* **1977,** *99* (1), 303-304.

33. Kawai, T.; Sakata, T., Conversion of carbohydrate into hydrogen fuel by a

photocatalytic process. *Nature* **1980,** *286* (5772), 474.

34. Halmann, M., Photoelectrochemical reduction of aqueous carbon dioxide on p-type gallium phosphide in liquid junction solar cells. *Nature* **1978,** *275* (5676), 115.

35. Inoue, T.; Fujishima, A.; Konishi, S.; Honda, K., Photoelectrocatalytic reduction of carbon dioxide in aqueous suspensions of semiconductor powders. *Nature* **1979,** *277* (5698), 637.

36. Fujishima, A.; Zhang, X.; Tryk, D. A., TiO2 photocatalysis and related surface phenomena. *Surface science reports* **2008,** *63* (12), 515-582.

37. Hashimoto, K.; Irie, H.; Fujishima, A., TiO2 photocatalysis: a historical overview and future prospects. *Japanese journal of applied physics* **2005,** *44* (12R), 8269.

38. Fujishima, A.; Rao, T. N.; Tryk, D. A., Titanium dioxide photocatalysis. *Journal of photochemistry and photobiology C: Photochemistry reviews* **2000,** *1* (1), 1-21.

39. Wang, R.; Hashimoto, K.; Fujishima, A.; Chikuni, M.; Kojima, E.;

Kitamura, A.; Shimohigoshi, M.; Watanabe, T., Light-induced amphiphilic surfaces. *Nature* **1997,** *388* (6641), 431.

40. Bai, J.; Zhou, B., Titanium dioxide nanomaterials for sensor applications. *Chemical reviews* **2014,** *114* (19), 10131-10176.

41. Colmenares, J. C.; Luque, R., Heterogeneous photocatalytic nanomaterials: prospects and challenges in selective transformations of biomass-derived compounds. *Chemical Society Reviews* **2014,** *43* (3), 765-778.

42. Banerjee, S.; Dionysiou, D. D.; Pillai, S. C., Self-cleaning applications of TiO2 by photo-induced hydrophilicity and photocatalysis. *Applied Catalysis B: Environmental* **2015,** *176*, 396-428.

43. Qiu, X.; Miyauchi, M.; Sunada, K.; Minoshima, M.; Liu, M.; Lu, Y.; Li, D.; Shimodaira, Y.; Hosogi, Y.; Kuroda, Y.; Hashimoto, K., Hybrid CuxO/TiO2 Nanocomposites As Risk-Reduction Materials in Indoor Environments. *ACS Nano* **2012,** *6* (2), 1609-1618.

44. Scaife, D., Oxide semiconductors in photoelectrochemical conversion of solar energy. *Solar Energy* **1980,** *25* (1), 41-54.

45. Li, X.; Wen, J.; Low, J.; Fang, Y.; Yu, J., Design and fabrication of semiconductor photocatalyst for photocatalytic reduction of CO 2 to solar fuel. *Science China Materials* **2014,** *57* (1), 70-100.

46. Windle, C. D.; Perutz, R. N., Advances in molecular photocatalytic and electrocatalytic CO2 reduction. *Coordination Chemistry Reviews* **2012,** *256* (21-22), 2562-2570.

47. Liu, L.; Li, Y., Understanding the reaction mechanism of photocatalytic reduction of CO2 with H2O on TiO2-based photocatalysts: a review. *Aerosol Air Qual. Res* **2014,** *14* (2), 453-469.

48. Baturina, O. A.; Lu, Q.; Padilla, M. A.; Xin, L.; Li, W.; Serov, A.; Artyushkova, K.; Atanassov, P.; Xu, F.; Epshteyn, A., CO2 electroreduction to hydrocarbons on carbon-supported Cu nanoparticles. *ACS Catalysis* **2014,** *4* (10), 3682-3695.

49. Chang, X.; Wang, T.; Zhang, P.; Wei, Y.; Zhao, J.; Gong, J., Stable aqueous photoelectrochemical CO2 reduction by a Cu2O dark cathode with improved selectivity for carbonaceous products. *Angewandte Chemie*

International Edition **2016,** *55* (31), 8840-8845.

50. Gattrell, M.; Gupta, N.; Co, A., A review of the aqueous electrochemical reduction of CO2 to hydrocarbons at copper. *Journal of Electroanalytical Chemistry* **2006,** *594* (1), 1-19.

51. Iizuka, K.; Wato, T.; Miseki, Y.; Saito, K.; Kudo, A., Photocatalytic reduction of carbon dioxide over Ag cocatalyst-loaded ALa4Ti4O15 (A= Ca, Sr, and Ba) using water as a reducing reagent. *Journal of the American Chemical Society* **2011,** *133* (51), 20863-20868.

52. Yamamoto, M.; Yoshida, T.; Yamamoto, N.; Nomoto, T.; Yamamoto, Y.; Yagi, S.; Yoshida, H., Photocatalytic reduction of CO 2 with water promoted by Ag clusters in Ag/Ga 2 O 3 photocatalysts. *Journal of Materials Chemistry A* **2015,** *3* (32), 16810-16816.

53. Chen, Y.; Li, C. W.; Kanan, M. W., Aqueous CO2 reduction at very low overpotential on oxide-derived Au nanoparticles. *Journal of the American Chemical Society* **2012,** *134* (49), 19969-19972.

54. Shoji, S.; Yin, G.; Nishikawa, M.; Atarashi, D.; Sakai, E.; Miyauchi, M.,

Photocatalytic reduction of CO2 by CuxO nanocluster loaded SrTiO3 nanorod thin film. *Chemical Physics Letters* **2016,** *658*, 309-314.

55. Shoji, S.; Yamaguchi, A.; Sakai, E.; Miyauchi, M., Strontium Titanate Based Artificial Leaf Loaded with Reduction and Oxidation Cocatalysts for Selective CO2 Reduction Using Water as an Electron Donor. *ACS Applied Materials & Interfaces* **2017,** *9* (24), 20613-20619.

56. Arai, T.; Sato, S.; Uemura, K.; Morikawa, T.; Kajino, T.; Motohiro, T., Photoelectrochemical reduction of CO 2 in water under visible-light irradiation by a p-type InP photocathode modified with an electropolymerized ruthenium complex. *Chemical communications* **2010,** *46* (37), 6944-6946.

57. Jiang, H.; Katsumata, K.-i.; Hong, J.; Yamaguchi, A.; Nakata, K.; Terashima, C.; Matsushita, N.; Miyauchi, M.; Fujishima, A., Photocatalytic reduction of CO2 on Cu2O-loaded Zn-Cr layered double hydroxides. *Applied Catalysis B: Environmental* **2018,** *224,* 783-790.

58. Teramura, K.; Tanaka, T.; Ishikawa, H.; Kohno, Y.; Funabiki, T.,

Photocatalytic Reduction of CO2 to CO in the Presence of H2 or CH4 as a Reductant over MgO. *The Journal of Physical Chemistry B* **2004,** *108* (1), 346-354.

59. Shi, D.; Feng, Y.; Zhong, S., Photocatalytic conversion of CH4 and CO2 to oxygenated compounds over Cu/CdS–TiO2/SiO2 catalyst. *Catalysis Today* **2004,** *98* (4), 505-509.

60. Yuliati, L.; Itoh, H.; Yoshida, H., Photocatalytic conversion of methane and carbon dioxide over gallium oxide. *Chemical Physics Letters* **2008,** *452* (1), 178-182.

61. Han, B.; Wei, W.; Chang, L.; Cheng, P.; Hu, Y. H., Efficient visible light photocatalytic CO2 reforming of CH4. *ACS Catalysis* **2015,** *6* (2), 494-497.

62. Song, H.; Meng, X.; Wang, Z.-j.; Wang, Z.; Chen, H.; Weng, Y.; Ichihara, F.; Oshikiri, M.; Kako, T.; Ye, J., Visible-Light-Mediated Methane Activation for Steam Methane Reforming under Mild Conditions: A Case Study of Rh/TiO2 Catalysts. *ACS Catalysis* **2018,** *8* (8), 7556-7565.

63. Wibowo, S.; Yamaguchi, A.; Shoji, S.; Fujita, T.; Abe, H.; Miyauchi, M.,

Photo-assisted Dry Reforming of Methane over Strontium Titanate. *Chemistry Letters* **2018,** *47* (7), 935-937.

64. Li, S.; Gong, J., Strategies for improving the performance and stability of Ni-based catalysts for reforming reactions. *Chemical Society Reviews* **2014,** *43* (21), 7245-7256.

65. Zhu, J.; van Ommen, J. G.; Bouwmeester, H. J. M.; Lefferts, L., Activation of O2 and CH4 on yttrium-stabilized zirconia for the partial oxidation of methane to synthesis gas. *Journal of Catalysis* **2005,** *233* (2), 434-441.

66. Han, J. W.; Kim, C.; Park, J. S.; Lee, H., Highly coke - resistant Ni nanoparticle catalysts with minimal sintering in dry reforming of methane. *ChemSusChem* **2014,** *7* (2), 451-456.

67. Tsang, S. C.; Claridge, J. B.; Green, M. L. H., Recent advances in the conversion of methane to synthesis gas. *Catalysis Today* **1995,** *23* (1), 3-15.

68. Budiman, A. W.; Song, S.-H.; Chang, T.-S.; Shin, C.-H.; Choi, M.-J., Dry reforming of methane over cobalt catalysts: a literature review of catalyst

development. *Catalysis Surveys from Asia* **2012,** *16* (4), 183-197.

69. Kim, S. M.; Abdala, P. M.; Margossian, T.; Hosseini, D.; Foppa, L.; Armutlulu, A.; van Beek, W.; Comas-Vives, A.; Copéret, C.; Müller, C., Cooperativity and Dynamics Increase the Performance of NiFe Dry Reforming Catalysts. *Journal of the American Chemical Society* **2017,** *139* (5), 1937-1949.

70. Margossian, T.; Larmier, K.; Kim, S. M.; Krumeich, F.; Fedorov, A.; Chen, P.; Müller, C. R.; Copéret, C., Molecularly tailored nickel precursor and support yield a stable methane dry reforming catalyst with superior metal utilization. *Journal of the American Chemical Society* **2017,** *139* (20), 6919-6927.

71. Hu, Y. H.; Ruckenstein, E., BINARY MgO-BASED SOLID SOLUTION CATALYSTS FOR METHANE CONVERSION TO SYNGAS. *Catalysis Reviews* **2002,** *44* (3), 423-453.

72. Pakhare, D.; Schwartz, V.; Abdelsayed, V.; Haynes, D.; Shekhawat, D.; Poston, J.; Spivey, J., Kinetic and mechanistic study of dry (CO2)

reforming of methane over Rh-substituted La2Zr2O7 pyrochlores. *Journal of catalysis* **2014,** *316*, 78-92.

73. Kathiraser, Y.; Oemar, U.; Saw, E. T.; Li, Z.; Kawi, S., Kinetic and mechanistic aspects for CO2 reforming of methane over Ni based catalysts. *Chemical Engineering Journal* **2015,** *278*, 62-78.

74. Das, S.; Ashok, J.; Bian, Z.; Dewangan, N.; Wai, M.; Du, Y.; Borgna, A.; Hidajat, K.; Kawi, S., Silica–Ceria sandwiched Ni core–shell catalyst for low temperature dry reforming of biogas: Coke resistance and mechanistic insights. *Applied Catalysis B: Environmental* **2018,** *230*, 220-236.

75. Li, Z.; Li, M.; Bian, Z.; Kathiraser, Y.; Kawi, S., Design of highly stable and selective core/yolk–shell nanocatalysts—A review. *Applied Catalysis B: Environmental* **2016,** *188*, 324-341.

76. Li, Z.; Das, S.; Hongmanorom, P.; Dewangan, N.; Wai, M. H.; Kawi, S., Silica-based micro-and mesoporous catalysts for dry reforming of methane. *Catalysis Science & Technology* **2018,** *8* (11), 2763-2778.

77. Tanabe, T.; Imai, T.; Tokunaga, T.; Arai, S.; Yamamoto, Y.; Ueda, S.;

Ramesh, G. V.; Nagao, S.; Hirata, H.; Matsumoto, S.-i.; Fujita, T.; Abe, H., Nanophase-separated Ni3Nb as an automobile exhaust catalyst. *Chemical Science* **2017,** *8* (5), 3374-3378.

78. Shoji, S.; Peng, X.; Imai, T.; Murphin Kumar, P. S.; Higuchi, K.; Yamamoto, Y.; Tokunaga, T.; Arai, S.; Ueda, S.; Hashimoto, A.; Tsubaki, N.; Miyauchi, M.; Fujita, T.; Abe, H., Topologically immobilized catalysis centre for long-term stable carbon dioxide reforming of methane. *Chemical Science* **2019,** *10* (13), 3701-3705.

79. Baker, R. T. K.; Barber, M. A.; Harris, P. S.; Feates, F. S.; Waite, R. J., Nucleation and growth of carbon deposits from the nickel catalyzed decomposition of acetylene. *Journal of Catalysis* **1972,** *26* (1), 51-62.

80. Yang, R.; Chen, J., Mechanism of carbon filament growth on metal catalysts. *Journal of Catalysis* **1989,** *115* (1), 52-64.

81. Tessonnier, J. P.; Su, D. S., Recent progress on the growth mechanism of carbon nanotubes: a review. *ChemSusChem* **2011,** *4* (7), 824-847.

82. Sun, G.; Hidajat, K.; Wu, X.; Kawi, S., A crucial role of surface oxygen

mobility on nanocrystalline Y2O3 support for oxidative steam reforming of ethanol to hydrogen over Ni/Y2O3 catalysts. *Applied Catalysis B: Environmental* **2008,** *81* (3-4), 303-312.

83. Malacrida, P.; Sanchez Casalongue, H. G.; Masini, F.; Kaya, S.; Hernández-Fernández, P.; Deiana, D.; Ogasawara, H.; Stephens, I. E. L.; Nilsson, A.; Chorkendorff, I., Direct observation of the dealloying process of a platinum–yttrium nanoparticle fuel cell cathode and its oxygenated species during the oxygen reduction reaction. *Physical Chemistry Chemical Physics* **2015,** *17* (42), 28121-28128.

84. Huang, X.; Xue, G.; Wang, C.; Zhao, N.; Sun, N.; Wei, W.; Sun, Y., Highly stable mesoporous NiO–Y2O3–Al2O3 catalysts for CO2 reforming of methane: effect of Ni embedding and Y2O3 promotion. *Catalysis Science & Technology* **2016,** *6* (2), 449-459.

85. Ferreira-Aparicio, P.; Fernandez-Garcia, M.; Guerrero-Ruiz, A.; Rodrı; guez-Ramos, I., Evaluation of the role of the metal–support interfacial centers in the dry reforming of methane on alumina-supported rhodium

catalysts. *Journal of Catalysis* **2000,** *190* (2), 296-308.

86. Wang, W.; Su, C.; Wu, Y.; Ran, R.; Shao, Z., Progress in solid oxide fuel cells with nickel-based anodes operating on methane and related fuels. *Chemical Reviews* **2013,** *113* (10), 8104-8151.

87. Palacin, M. R., Recent advances in rechargeable battery materials: a chemist's perspective. *Chemical Society Reviews* **2009,** *38* (9), 2565-2575.

88. Kato, H.; Kudo, A., Water splitting into H2 and O2 on alkali tantalate photocatalysts ATaO3 (A= Li, Na, and K). *The Journal of Physical Chemistry B* **2001,** *105* (19), 4285-4292.

89. Sekizawa, K.; Maeda, K.; Domen, K.; Koike, K.; Ishitani, O., Artificial Z-Scheme Constructed with a Supramolecular Metal Complex and Semiconductor for the Photocatalytic Reduction of CO2. *Journal of the American Chemical Society* **2013,** *135* (12), 4596-4599.

90. Bahnemann, D., Photocatalytic water treatment: solar energy applications. *Solar Energy* **2004,** *77* (5), 445-459.

91. Hsu, H.-C.; Shown, I.; Wei, H.-Y.; Chang, Y.-C.; Du, H.-Y.; Lin, Y.-G.;

Tseng, C.-A.; Wang, C.-H.; Chen, L.-C.; Lin, Y.-C.; Chen, K.-H., Graphene oxide as a promising photocatalyst for CO2 to methanol conversion. *Nanoscale* **2013,** *5* (1), 262-268.

92. Yuliati, L.; Yoshida, H., Photocatalytic conversion of methane. *Chemical Society Reviews* **2008,** *37* (8), 1592-1602.
93. Shimura, K.; Kato, S.; Yoshida, T.; Itoh, H.; Hattori, T.; Yoshida, H., Photocatalytic steam reforming of methane over sodium tantalate. *The Journal of Physical Chemistry C* **2010,** *114* (8), 3493-3503.
94. Konta, R.; Ishii, T.; Kato, H.; Kudo, A., Photocatalytic activities of noble metal ion doped SrTiO3 under visible light irradiation. *The Journal of Physical Chemistry B* **2004,** *108* (26), 8992-8995.
95. Osaki, T.; Mori, T., Role of Potassium in Carbon-Free CO2 Reforming of Methane on K-Promoted Ni/Al2O3 Catalysts. *Journal of Catalysis* **2001,** *204* (1), 89-97.
96. Sayama, K.; Mukasa, K.; Abe, R.; Abe, Y.; Arakawa, H., Stoichiometric water splitting into H2 and O2 using a mixture of two different photocatalysts and an IO3－/I－ shuttle redox mediator under visible light irradiation. *Chemical Communications* **2001,** (23), 2416-2417.
97. Miyauchi, M.; Nakajima, A.; Watanabe, T.; Hashimoto, K., Photocatalysis and Photoinduced Hydrophilicity of Various Metal Oxide Thin Films. *Chemistry of Materials* **2002,** *14* (6), 2812-2816.

98. Nosaka, Y.; Takahashi, S.; Mitani, Y.; Qiu, X.; Miyauchi, M., Reaction mechanism of visible-light responsive Cu (II)-grafted Mo-doped SrTiO3 photocatalyst studied by means of ESR spectroscopy and chemiluminescence photometry. *Applied Catalysis B: Environmental* **2012,** *111,* 636-640.

99. Hirakawa, T.; Nakaoka, Y.; Nishino, J.; Nosaka, Y., Primary Passages for Various TiO2 Photocatalysts Studied by Means of Luminol Chemiluminescent Probe. *The Journal of Physical Chemistry B* **1999,** *103* (21), 4399-4403.

100. Chiesa, M.; Paganini, M. C.; Livraghi, S.; Giamello, E., Charge trapping in TiO2 polymorphs as seen by Electron Paramagnetic Resonance spectroscopy. *Physical Chemistry Chemical Physics* **2013,** *15* (24), 9435-9447.

101. Maeda, K.; Teramura, K.; Lu, D.; Saito, N.; Inoue, Y.; Domen, K., Noble-Metal/Cr2O3 Core/Shell Nanoparticles as a Cocatalyst for Photocatalytic Overall Water Splitting. *Angewandte Chemie* **2006,** *118* (46), 7970-7973.

102. Kazuma, E.; Tatsuma, T., In Situ Nanoimaging of Photoinduced Charge Separation at the Plasmonic Au Nanoparticle - TiO2 Interface. *Advanced Materials Interfaces* **2014,** *1* (3), 1400066.

103. Watanabe, R.; Sakamoto, Y.; Yamamuro, K.; Tamura, S.; Kikuchi, E.; Sekine, Y., Role of alkali metal in a highly active Pd/alkali/Fe2O3 catalyst for water gas shift reaction. *Applied Catalysis A: General* **2013,** *457,* 1-11.

104. Jiang, H.; Peng, X.; Yamaguchi, A.; Ueda, S.; Fujita, T.; Abe, H.; Miyauchi, M., Photocatalytic Partial Oxidation of Methane on Palladium-Loaded Strontium Tantalate. *Solar RRL* **2019,** *3* (7), 1900076.

105. Miyauchi, M.; Takashio, M.; Tobimatsu, H., Photocatalytic activity of SrTiO3 codoped with nitrogen and lanthanum under visible light illumination. *Langmuir* **2004,** *20* (1), 232-236.

106. Gotte, A.; Spångberg, D.; Hermansson, K.; Baudin, M., Molecular dynamics study of oxygen self-diffusion in reduced CeO2. *Solid State Ionics* **2007,** *178* (25), 1421-1427.

107. Wetchakun, N.; Chaiwichain, S.; Inceesungvorn, B.; Pingmuang, K.; Phanichphant, S.; Minett, A. I.; Chen, J., BiVO4/CeO2 Nanocomposites with High Visible-Light-Induced Photocatalytic Activity. *ACS Applied Materials & Interfaces* **2012,** *4* (7), 3718-3723.

108. Tian, J.; Sang, Y.; Zhao, Z.; Zhou, W.; Wang, D.; Kang, X.; Liu, H.; Wang, J.; Chen, S.; Cai, H., Enhanced photocatalytic performances of CeO2/TiO2 nanobelt heterostructures. *Small* **2013,** *9* (22), 3864-3872.

109. Wang, S.; Lu, G. Q.; Millar, G. J., Carbon Dioxide Reforming of Methane To Produce Synthesis Gas over Metal-Supported Catalysts: State of the Art. *Energy & Fuels* **1996,** *10* (4), 896-904.

110. Irie, H.; Shibanuma, T.; Kamiya, K.; Miura, S.; Yokoyama, T.; Hashimoto, K., Characterization of Cr (III)-grafted TiO2 for photocatalytic reaction under visible light. *Applied Catalysis B: Environmental* **2010,** *96* (1-2),

142-147.

111. Irie, H.; Miura, S.; Kamiya, K.; Hashimoto, K., Efficient visible light-sensitive photocatalysts: grafting Cu (II) ions onto TiO2 and WO3 photocatalysts. *Chemical Physics Letters* **2008,** *457* (1-3), 202-205.

112. Gronchi, P.; Mazzocchia, C.; Del Rosso, R., Carbon dioxide reaction with methane on La2O3 supported Rh catalysts. *Energy conversion and management* **1995,** *36* (6-9), 605-608.

113. Topalidis, A.; Petrakis, D. E.; Ladavos, A.; Loukatzikou, L.; Pomonis, P. J., A kinetic study of methane and carbon dioxide interconversion over 0.5%Pt/SrTiO3 catalysts. *Catalysis Today* **2007,** *127* (1), 238-245.

114. Ashcroft, A.; Cheetham, A.; Green, M., Partial oxidation of methane to synthesis gas using carbon dioxide. *Nature* **1991,** *352* (6332), 225-226.

115. Nosaka, Y.; Nosaka, A. Y., Generation and detection of reactive oxygen species in photocatalysis. *Chemical reviews* **2017,** *117* (17), 11302-11336.

116. Bard, A., *Standard potentials in aqueous solution*. Routledge: 2017.

117. Wardman, P., Reduction potentials of one‐electron couples involving free radicals in aqueous solution. *Journal of Physical and Chemical Reference Data* **1989,** *18* (4), 1637-1755.

118. Wibowo, S.; Shoji, S.; Takeda, K.; Haoyang, J.; Yamaguchi, A.; Fujita, T.; Abe, H.; Miyauchia, M., Photo-assisted dry reforming of methane over ruthenium loaded strontium titanate.

119 Edwards, J. H.; Maitra, A. M., The chemistry of methane reforming with

carbon dioxide and its current and potential applications. *Fuel Processing Technology* **1995,** *42* (2), 269-289.

120 Djinović, P.; Batista, J.; Pintar, A., Efficient catalytic abatement of greenhouse gases: Methane reforming with CO2 using a novel and thermally stable Rh–CeO2 catalyst. *International Journal of Hydrogen Energy* **2012,** *37* (3), 2699-2707.

121 Laosiripojana, N.; Sutthisripok, W.; Assabumrungrat, S., Synthesis gas production from dry reforming of methane over CeO2 doped Ni/Al2O3: Influence of the doping ceria on the resistance toward carbon formation. *Chemical Engineering Journal* **2005,** *112* (1), 13-22.

Acknowledgement

Firstly, I want to show my gratitude to *Prof. A. Nakajima, Prof. T. Ikoma, Prof. N. Matsushita, and Prof. S. Matsushita* for reviewing my thesis and undertaking the investigation of my work.

I would like to give my greatest appreciate and respects to my advisors, *Prof. M. Miyauchi, Prof. E. Sakai, and Dr. A. Yamaguchi* for their benevolent conduction for my research and life. They are always full of kindness and always trying to educate me to be greater researcher. They always sincerely listen what I said and provided me best suggestions. Without their encourage, I'm not here, I think. Especially thanks *Prof. M. Miyauchi* for his kindest guide and concern for me and always showing me wonderful and new area.

I also thanks to *Prof. H. Abe and Prof. Fujita* from NIMS and Kochi institute of technology. Their generous ideas helped my research and amazing personality provided me so much things. I am confident that our relationship is unending something. I also thanks to Prof. Xiaobo Peng and Dr. Sani to be my best friend in NIMS and so much collaboration.

It’s my honor to get the supporting from *CREST* from Japanese Science and Technology Agency. I also appreciate the financial supporting from *the Japan Society for the Promotion of Science (JSPS)* and *Japanese Government and Tokyo Institute of Technology from the Japanese Government (Monbukagakusho) Scholarship program.*

My deep gratitude goes to Ms. Y. Nakai, Dr. G. Yin, Dr. S. Koyasu, Dr. H. Jiang, Mr. R. Kawamura, Mr. Y. Cho, Mr. M. Kushida, Miss Y. Yang, my brother Dr. K. Shoji, Mr. Kotaro. Shoji, Mr. Waojiro. Shoji, parents and all the active members and alumni of Miyauchi Laboratory. I also thanks to Mr. Y. Suzuki, Mr. U. Kojima and Mr. P. Kataya for deep discussion of the thesis design.

At last, I would like to offer my best regards to all of those who supported me in any respect during the completion of the research.

Shusaku Shoji 2019/01/27

List of publications

As First author

1. **Shusaku Shoji**, Ge Yin, Masami Nishikawa, Daiki Atarashi, Etsuo Sakai, Masahiro Miyauchi. ”Photocatalytic reduction of CO_2 by Cu_xO nanocluster loaded $SrTiO_3$ nanorod thin film”, ***Chemical Physics Letters***., 658, 309–314, 2016.

2. **Shusaku Shoji**, AkiraYamaguchi, Etsuo Sakai, Masahiro Miyauchi. “Strontium titanate based artificial leaf loaded with reduction and oxidation cocatalysts for selective CO_2 reducreduction using water as an electron donor” ***ACS applied materials & interfaces***, 9 (24), 20613–20619, 2017.

3. **Shusaku Shoji**, Peng Xiaobo, Tsubasa Imai, Paskalis Sahaya Murphin Kumar, Kimitaka Higuchi, Yuta Yamamoto, Tomoharu Tokunaga, Shigeo Arai, Shigenori Ueda, Ayako Hashimoto, Noritatsu Tsubaki,Masahiro Miyauchi, Takeshi Fujita, Hideki Abe “Topologically Immobilized Catalysis Centre for Long-term Stable Carbon Dioxide Reforming of Methane” ***Chemical Science***. 10 (13), 3701-3705, 2019.

4. **Shusaku Shoji**, Xiaobo Peng, Akira Yamaguchi, Ryo Watanabe, Choji Fukuhara, Yohei Cho, Tomokazu Yamamoto, Syo Matsumura, Min-Wen Yu, Satoshi Ishii, Takeshi Fujita, Hideki Abe and Masahiro Miyauchi “Photocatalytic uphill conversion of natural gas beyond the limitation of thermal reaction systems” ***Nature Catalysis***. accepted in press (DOI：10.1038/s41929-019-0419-z).

5. **Shusaku Shoji**, Abdillah Sani Bin Mohd Najib, Peng Xiaobo, Tomokazu Yamamoto, Syo Matsumura, Akira Yamaguchi, Satoshi Ishii, Yohei Cho, Takeshi Fujita, Hideki Abe and Masahiro Miyauchi “Rooted Rh#CeO_2 photocatalyst for stable and high active Dry reforming of methane conversion under extra mild condition.” ready to submit

As contributed author

6. Y Nukui, N Srinivasan, S Shoji, D Atarashi, E Sakai, M Miyauchi “Vertically aligned hexagonal WO_3 nanotree electrode for photoelectrochemical water oxidation” ***Chemical Physics Letters*** 635, 306-311, 2015.

7. S Wibowo, A Yamaguchi, S Shoji, T Fujita, H Abe, M Miyauchi. “Photo-assisted Dry Reforming of Methane over Strontium Titanate.” ***Chemistry Letters*** 47 (7), 935-937, 2018.

8. ASBM Najib, X Peng, A Hashimoto, S Shoji, T Iida, Y Bai, H Abe. “Mesoporous Rh Emerging from Nanophase-separated Rh-Y Alloy.” ***Chemistry, an Asian journal*** 14 (16), 2802-2805, 2019.